

NASA Contractor Report 3988

Compression Failure Mechanisms of Composite Structures

H. Thomas Hahn, Mohsen Sohi,
and Suresh Moon

*Washington University
St. Louis, Missouri*

Prepared for
Langley Research Center
under Grant NAG1-295

Accesion For	
NTIS	CRA&I
DTIC	TAB
Unannounced	
Justification _____	
By _____	
Distribution / _____	
Availability Codes _____	
Dist	Avail and / or Special
A-1	



National Aeronautics
and Space Administration

Scientific and Technical
Information Branch

1986

FOREWORD

This document is the final report on research into the compression failure mechanisms of composite structures conducted under NASA Grant NAG-1-295. The work was conducted from August 1982 to July 1985. Dr. Jerry G. Williams of Langley Research Center, Hampton, Virginia was the NASA technical monitor of the grant. Other papers and reports published under the grant are listed in the Appendix.

Appreciation is extended to Union Carbide and Owens-Corning for supplying graphite and glass fibers, respectively, used in this program.

ABSTRACT

An experimental and analytical study was conducted to delineate the compression failure mechanisms of composite structures. Results on unidirectional and quasi-isotropic graphite/epoxy laminates were published previously. The present report summarizes further results on kink band formation in unidirectional composites.

In order to assess the compressive strengths and failure modes of fibers themselves, a fiber bundle was embedded in epoxy casting and tested in compression. A total of six different fibers were used together with two resins of different stiffnesses. The failure of highly anisotropic fibers such as Kevlar 49 and P-75 graphite was due to kinking of fibrils. However, the remaining fibers--T300 and T700 graphite, E-glass, and alumina--failed by localized microbuckling. Compressive strengths of the latter group of fibers were not fully utilized in their respective composites. In addition, acoustic emission monitoring revealed that fiber-matrix debonding did not occur gradually but suddenly at final failure.

The kink band formation in unidirectional composites under compression was studied analytically and through microscopy. The material combinations selected include seven graphite/epoxy composites, two graphite/thermoplastic resin composites, one Kevlar 49/epoxy composite and one S-glass/epoxy composite. The dominant mode of failure in all composites was the kink band initiation and propagation. Thus, not only microbuckling but also compressive failure of fibers could trigger kink band formation. An analytical model was developed under the assumption of plastic yielding in the matrix, and it was used successfully to calculate parameters defining

the kink band geometry. The sudden nature of fiber-matrix debonding was confirmed by testing precompressed specimens in short-beam shear.

TABLE OF CONTENTS

1.0	INTRODUCTION	1
2.0	COMPRESSIVE FAILURE OF FIBER BUNDLES EMBEDDED IN EPOXY CASTING	4
2.1	Background	4
2.2	Specimen Preparation and Testing	5
2.3	Failure Modes	8
2.4	Failure Strains	21
2.5	Detection of Subcritical Failure by Acoustic Emission ...	27
2.6	Summary	46
3.0	KINK BAND FORMATION	48
3.1	Incipient Failure	48
3.2	Kink Band Formation	51
3.3	Experimental Observations	59
3.4	Short-Beam-Shear Testing of Preloaded Graphite/Epoxy Composites	92
3.5	Summary	98
4.0	CONCLUSIONS	100
5.0	REFERENCES	102

LIST OF TABLES

Table	Page
1. Fiber-Resin Combinations	6
2. Resin Properties	7
3. Fiber Properties	7
4. Acoustic Emission Preset Parameters	30
5. Mechanical Properties of Different Unidirectional Composites	60
6. Prediction of Maximum Strains on the Fiber at the Time of Failure	89
7. Predicted Values of Kink Orientation Angle, Kink Length, and Shear Strain at Failure	91
8. Short-Beam-Shear Test Results	95

LIST OF FIGURES

Figure		Page
1	A plate specimen in the compression fixture	9
2	Uniform buckling of E-glass bundle in a weak Epon 815/V140 ...	11
3	Localized buckling of E-glass bundle in Epon 815/V140	11
4	Localized buckling of E-glass bundle in Epon 828/Z	13
5	Localized failure of T300 graphite bundle in Epon 828/Z	13
6	Failure of FP fiber bundle in Epon 815/V140	14
7	Failure of Kevlar fiber bundle in Epon 815/V140	14
8a	SEM micrographs of E-glass bundles: Epon 815/V140	15
8b	SEM micrographs of E-glass bundles: Epon 828/Z	15
9a	SEM micrographs of T300 graphite bundles: Epon 815/V140	17
9b	SEM micrographs of T300 graphite bundles: Epon 828/Z	17
10a	SEM micrographs of T700 graphite bundles: Epon 815/V140	18
10b	SEM micrographs of T700 graphite bundles: Epon 828Z	18
11a	SEM micrographs of FP alumina bundle: bundle	19
11b	SEM micrographs of FP alumina bundle: broken end	19
12a	SEM micrographs of P75 graphite bundles: Epon 815/V140	20
12b	SEM micrographs of P75 graphite bundles: Epon 828/Z	20
13	Numbers of fiber breaks and average segment lengths	22
14	Stress-strain curves for Epon 828/Z specimens with embedded fiber bundle	23
15	Compressive failure strains of bundles	25
16	Compressive failure strain as a function of fiber tensile failure strain.....	26
17	Compressive failure strain increasing with square root of matrix-to-fiber modulus ratio	28

18	Average segment length increasing with quadratic root of fiber-to-matrix modulus ratio and with fiber diameter	29
19	Stress and cumulative events vs. strain for Epon 815/V140	31
20	Stress and cumulative events vs. strain for E-G1/815.....	33
21a	SEM micrographs of specimen cross-sections: poor bonding	34
21b	SEM micrographs of specimen cross-sections: good bonding	34
22	Cumulative events vs. time for E-G1/815 with good and poor bonding	36
23	Cumulative events vs. time for potted E-G1/815 specimens with good and poor bonding	37
24a	A virgin specimen	38
24b	Extensive debonding in failed specimen	38
25	Stress and cumulative events vs. strain for FP/815	39
26	Stress and cumulative events vs. strain for T300/815	40
27	Stress and cumulative events vs. strain for KV/815	42
28	Comparison of acoustic emission activities for various embedded bundles	43
29	Mean peak amplitude vs. time for Epon 815 and for different fiber bundles embedded in Epon 815	44
30a	Kink band formation: kink band geometry	52
30b	Kink band formation: a kinked fiber before collapse	52
30c	Kink band formation: free body diagram for an infinitesimal fiber element	52
31a	Failure initiation in a T300/BP907 specimen: 200 X	61
31b	Failure initiation in a T300/BP907 specimen: 500 X	61
32	Primary and conjugate kink bands in a T300/BP specimen	62
33a	Fiber fracture surfaces in a T300/5208 specimen	64
33b	Bending failure of a brittle fiber	64
34	Fiber fracture surfaces in a T300/mPDA specimen	65

35	Fiber fracture surfaces in a T300/PPS specimen	65
36	Failure through the width of a T300/5208 specimen	67
37	Failure through the width of a T300/BP907 specimen	67
38	Failure through the width of a T300/4901/MDA specimen	68
39	Failure through the width of a T300/4901/mPDA specimen	68
40	Failure through the width of a T700/BP907 specimen	69
41	Failure through the width of a T700/4901/MDA specimen	69
42	Failure through the width of a T300/PPS specimen	70
43	Failure through the thickness of a T300/PPS specimen	71
44	Failure through the width of a T300/PEEK specimen	71
45	SEM micrograph of the fracture surface of a T300/5208 specimen	72
46	SEM micrograph of the fracture surface of a T300/BP907 specimen	73
47	SEM micrograph of the fracture surface of a T300/4901/MDA specimen	74
48	SEM micrograph of the fracture surface of a T300/4901/mPDA specimen	75
49	SEM micrograph of the fracture surface of a T700/BP907 specimen	76
50	SEM micrograph of the fracture surface of a T700/4901/MDA specimen	77
51	SEM micrograph of the fracture surface of a T700/4901/mPDA specimen	78
52	SEM micrograph of the fracture surface of a T300/PPS specimen	79
53	SEM micrograph of the fracture surface of a T300/PEEK specimen	80
54	SEM micrograph of a T300/BP907 specimen showing a fiber-matrix separation	81
55a	Kinking failure in Kevlar/epoxy specimens: tested room temperature	83
55b	Kinking failure in Kevlar/epoxy specimens: preconditioned and tested at room temperature	83

55c	Kinking failure in Kevlar/epoxy specimens: preconditioned and tested at 75°C	83
56a	Typical kinking failure in Kevlar specimens: overall view	84
56b	Typical kinking failure in Kevlar specimens: failure of fibers at the kink-band boundary	84
57	SEM micrograph of a Kevlar fiber within the kink band	85
58	SEM micrograph of a Kevlar fiber located immediately outside the kink band	85
59a	Compression failure in S2-glass/epoxy specimens: tested at room temperature	87
59b	Compression failure in S2-glass/epoxy specimens: tested at 100°C	87
60	Fiber fractures at the kink band boundary of a S2-glass/epoxy specimen tested at 100°C	88
61	Failure by a mixed mode of shear and microbuckling in a T300/5208 short-beam-shear specimen	96
62a	Shear dominated failure: in a virgin T300/mPDA specimen	97
62b	Shear dominated failure: in a virgin T700/mPDA specimen	97

1. INTRODUCTION

The tensile behavior of unidirectional composites is mostly dominated by fibers. In compression, however, the matrix and interface play a key role of providing lateral support to the fibers. Therefore, the compressive behavior depends very much on the properties of the matrix and the interface.

Recent studies [1,2] have shown that the undesirable weakness of composite structures to impact and delamination can be reduced by using tougher resins. However, higher toughness in a resin is frequently coupled with lower modulus, and lower modulus may lead to a lower compressive strength for the composite.

The above argument underscores the importance of a good understanding of compressive behavior of composites. Many modes of compressive failure have been proposed over the years. They include elastic buckling of fibers [3-10], fiber kinking [10-16], shear through both fibers and matrix [17], compressive failure or yielding of fibers [18,19], interfacial failure followed by longitudinal splitting [7,11,19,20], and local yielding or transverse compressive failure of the matrix [19]. Sometimes, the compressive failure is initiated by one mode and ends in another. For example, interfacial failure can be followed by fiber microbuckling; or fiber microbuckling may be followed by plastic deformation in the matrix that allows fibers to rotate and a kink band to form. This makes the identification of the critical mode of failure by post-failure examinations difficult. It is therefore important to slow down the failure process in order to identify the sequence of failure events.

Since the compressive load is primarily carried by the fibers as in tension, the final failure of composites occurs when the fibers fail. Other

events such as fiber-matrix debonding and matrix yielding do not by themselves cause the final failure; but they may facilitate fiber buckling by reducing the side support for the fibers. Failure of the fibers can only be one of the following two types: intrinsic and microbuckling-induced. The intrinsic compressive failure is the result of the fiber stress exceeding the fiber strength, and the microbuckling-induced failure is in fact a bending failure as a consequence of buckling.

The intrinsic compressive failure of fibers usually occurs in composites made with highly anisotropic or ductile fibers. Anisotropic fibers like Kevlar and high-modulus graphite fail by kinking of microfibrils, and ductile fibers by yielding. In most composites, however, the composite failure is the result of the microbuckling-induced failure of fibers. Fiber microbuckling is enhanced by failure or yielding of the matrix, fiber-matrix debonding, or the presence of voids. The term "microbuckling" refers not only to local buckling of initially straight fibers, but also, to increases in local curvature of initially misaligned fibers.

The main purpose of our research was to delineate the compressive failure mechanisms in composite structures. Results on compressive strengths and failure modes of unidirectional and quasi-isotropic graphite/epoxy laminates have been published in [10,21]. In the present report we discuss results of a more microscopic study on the failure mechanisms in unidirectional composites, which are the primary load-bearing members in multidirectional laminates.

To assess the intrinsic compressive strengths of fibers, a fiber bundle was embedded in epoxy casting and examined under compression. Bundle

specimens offer an additional advantage of containing failure and allow the failure to be monitored through the use of transparent resins.

A bundle of fibers rather than a single fiber was used to simulate the fiber-to-fiber interaction present in real composites. The fibers used are E-glass, T300 graphite, T700 graphite, P75 graphite, Kevlar 49, and FP alumina. These fibers were combined with two resins: Epon 815/V140 and Epon 828/Z. The former resin is softer than the latter. The use of resins with different stiffnesses is necessary to detect the failure induced by microbuckling.

In the second part, compressive failure modes of unidirectional composites were studied using optical and scanning electron microscopy. The eleven material systems chosen include seven graphite/epoxy composites (T300/5208, T300/BP907, T300/4901/MDA, T300/4901/mPDA, T700/BP907, T700/4901/MDA, T700/4901/mPDA), two graphite/thermoplastic resin composites (T300/PPS, T300/PEEK), one glass/epoxy composite (S2-glass/DER 332-Menthane Diamine), and one Kevlar/epoxy composite (Kevlar 49/DER 332-Menthane Diamine). The different material combinations allow one to investigate the effect of constituent materials on compressive failure.

The possibility of fiber-matrix debonding before final failure was also explored by monitoring acoustic emissions in embedded bundle specimens. As for unidirectional composites, a short-beam shear test following compression close to failure was used to find out whether or not compressive failure could be triggered by interfacial debonding.

2. COMPRESSIVE FAILURE OF FIBER BUNDLES EMBEDDED IN EPOXY CASTING

2.1 Background

Monitoring of the compressive failure process in composites is difficult because failure is quite sudden without much warning. The dynamic nature of the final failure makes it difficult to identify the microscopic failure sequence. Furthermore, failure tends to be initiated at stress concentration areas such as tab ends. Therefore, it is necessary to develop a means of containing failure without inadvertent introduction of stress concentrations if the true compressive failure sequence is to be delineated. A fiber bundle embedded in epoxy casting provides the needed opportunity to monitor the failure sequence and assess the compressive strength of the fiber.

Failure of fibers by themselves under compression was studied by embedding a single filament in a resin block [22,23]. In carbon fibers with varying moduli, the failure mode tended toward kinking of fibrils and the failure strain decreased, as the fiber anisotropy increased [21]. Yet, AS and Type II carbon fibers did not fail under loading up to 3% strain. Kevlar 49 fibers also failed by kinking of fibrils around 0.5 % strain [23].

The embedded single-filament test can determine the compressive load-carrying capability of fibers themselves. However, it includes no fiber-fiber interaction which is prevalent in real composites. Also, no effect of matrix and interface can be studied by means of this test.

Compressive tests on embedded fiber bundle specimens were conducted with three objectives in mind. The first was to assess the compressive strengths of fibers. The second was to identify the failure mechanisms under compression. The final objective was to study the effect of matrix

and interface on the compressive strength. Specimens were monitored during testing through an optical microscope to detect signs of imminent failure. Failed specimens were examined on a scanning electron microscope (SEM) to identify microscopic modes of failure. Acoustic emissions were monitored to help detect subcritical failures such as interfacial failure.

2.2 Specimen Preparation and Testing

Six different fibers were combined with two different epoxy resins, see Table 1. Two types of E-glass fiber bundles were used: one containing 200 filaments and the other containing 2040 filaments. The former had a polyester-compatible coupling agent applied while the latter was treated with an epoxy-compatible coupling agent. The Kevlar 49 bundle was in the form of a strand which had been impregnated and cured with DER 332/T403. The cured strand was then embedded in the epoxy casting. Epon 815/V140 was chosen to represent a soft resin, and Epon 828/Z, a stiff resin. The nominal properties of fibers and resins used are listed in Tables 2 and 3.

The use of two resins with different stiffnesses was necessary to ascertain whether the failure was intrinsic to the fibers or due to microbuckling. The resin properties were measured but the fiber properties were taken from manufacturers' data sheets. Further details of resin formulations and fabrication procedures can be found in Reference [24].

The IITRI compression fixture was used with a gage length of 13 mm. Specimen thickness varied from 4 to 6.5 mm while the width was kept at 6.5 mm. An Instron testing machine was used at a crosshead speed of 1.3 mm/min. During testing the fiber bundle was monitored for failure through a Zeiss stereo microscope at magnifications up to 50X. Since the fiber bundle

Table 1. Fiber-Resin Combinations

Fiber	No. of filaments per bundle	Resin	Specimen type	Remark
E-glass	200	Epon 815 Epon 828	IITRI IITRI	Polyester-compatible
	2040	Epon 815	Plate	Epoxy-compatible
T300 Graphite	3000	Epon 815	IITRI & Plate	
		Epon 828	IITRI	
T700 Graphite	4500	Epon 815	IITRI	
		Epon 828	IITRI	
P75 Graphite	2000	Epon 815	IITRI	
		Epon 828	IITRI	
FP Alumina	210	Epon 815	Plate	
Kevlar 49	267	Epon 815	Plate	Strand cured in DER332/T403

Table 2. Resin Properties

Epoxy	Modulus (GPa)	Ultimate tensile (MPa)	Tensile failure strain, %
Epon 828/Z (80/20)	3.45	85.4	9
Epon 815/V140 (60/40)	2.13	45.5	14

Table 3. Fiber Properties

Fiber	Diameter (μm)	Cross-sectional area of bundle (mm^2)	Modulus (GPa)	Tensile failure strain, %
E-G1	13.5	2.92×10^{-2}	72.35	4.80
T700	5.1	9.16×10^{-2}	234.00	1.83
T300	7.0	11.61×10^{-2}	230.00	1.34
P75	9.7	14.84×10^{-2}	517.00	0.40
FP	20.0	6.60×10^{-2}	379.00	0.36

occupied a small fraction of the specimen volume, its failure did not lead to specimen failure. Thus the bundle failure could be contained and monitored.

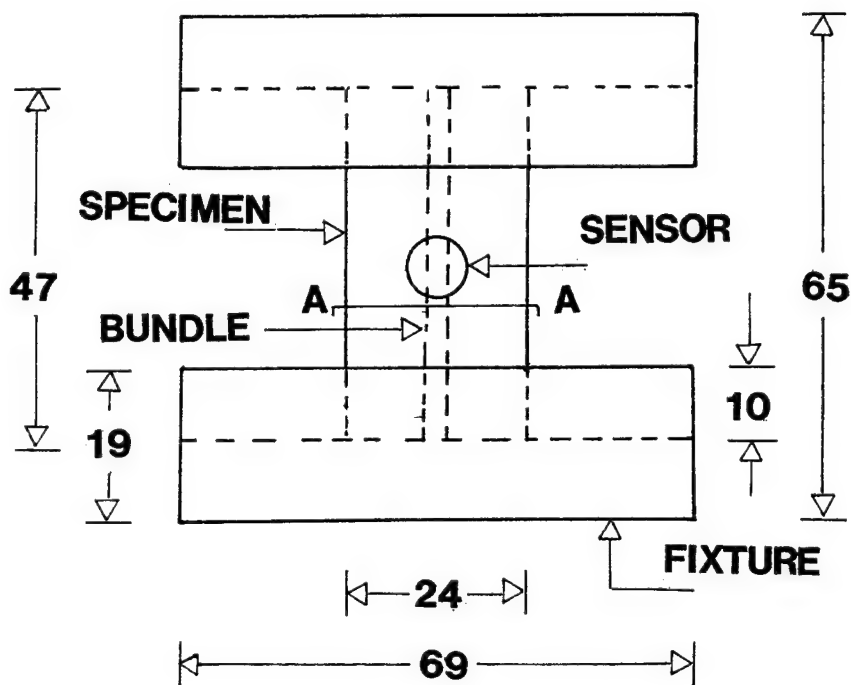
The bundle failure was monitored also on load-strain curves. Two specimens of each material combination had a strain gage attached. Microbuckling of the bundle always resulted in a sudden load drop. However, failure of the P75 and Kevlar 49 fibers did not result in a sudden load drop, and hence could be detected only visually.

After bundle failure, the specimen was cracked open through the bundle and examined on a scanning electron microscope (SEM). Modes of fiber fracture were noted, and the lengths of broken segments were measured.

Additionally, rectangular plate specimens were used to investigate acoustic emission (AE) behavior. All the E-glass bundles in plate specimens had 2040 filaments. The specimen dimensions were chosen so as to accommodate a 8-mm diameter AE transducer and to avoid global buckling. A strain gage was bonded on one side of the specimen and the AE transducer was attached on the other with a high-viscosity silicone grease as coupling agent. The transducer had a resonant frequency of 425 KHz and an AET 5000 system was used to monitor acoustic emissions. The loading was at the top and bottom edges of the specimen in a specially made fixture, as shown in Figure 1. A Teflon strip was inserted between each side of the specimen and the fixture to eliminate the noise that might be generated by friction. A crosshead speed of 1 mm/min was used for the plate specimens.

2.3 Failure Modes

The two compressive failure modes most frequently encountered in the literature are fiber microbuckling and fiber kinking. In the microbuckling



SECTION AA

ALL DIMENSIONS IN mm

Figure 1. A plate specimen in the compression fixture.

mode of failure the fibers usually fracture at several points and there is no relative lateral displacement across the failure zone. In kinking the fibers (initially) fracture at two points and there is relative displacement of the fibers across the failure zone.

Figure 2 shows buckling of the E-glass bundle (200 filaments) in a weak epoxy occurring over its entire length. The epoxy, Epon 815/V140, had too much solvent inadvertently added during formulation, and as a result, was much softer than it should have been. Buckling of the fiber bundle in this epoxy was quite gradual, starting at a very low load, and occurred uniformly over the entire gage length. Note that all fibers buckled in phase with one another.

The elliptical spots seen over the bundle in Figure 2 are cracks growing into the matrix almost normal to the plane of the photograph. These cracks were generated by the tensile stress between the fibers as a result of buckling. Note also that fibers have not broken yet, even though they are bent.

Failure of the E-glass bundle in a well formulated Epon 815 is catastrophic and quite localized, and is in the form of microbuckling, Figure 3. Microbuckling occurs without warning and immediately leads to fracture of fibers. Fiber fracture is seen to progress from one edge of the bundle to the other.

Microbuckling of the E-glass bundle in the stiffer Epon 828 is also quite localized, Figure 4. Although the bundle has an elliptical cross section, it can buckle in the plane of the larger dimension as well. The buckled region is out of focus because of the out-of-plane movement of the bundle. Macroscopically, no distinction could be detected between bundle

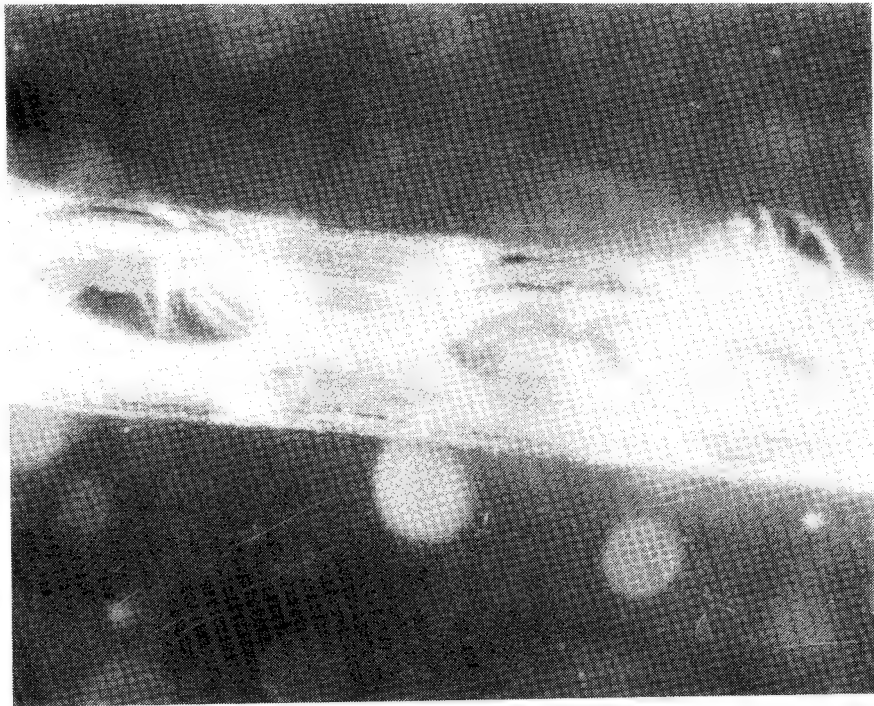


Figure 2. Uniform buckling of E-glass bundle in a weak Epon 815/V140 (74 X).

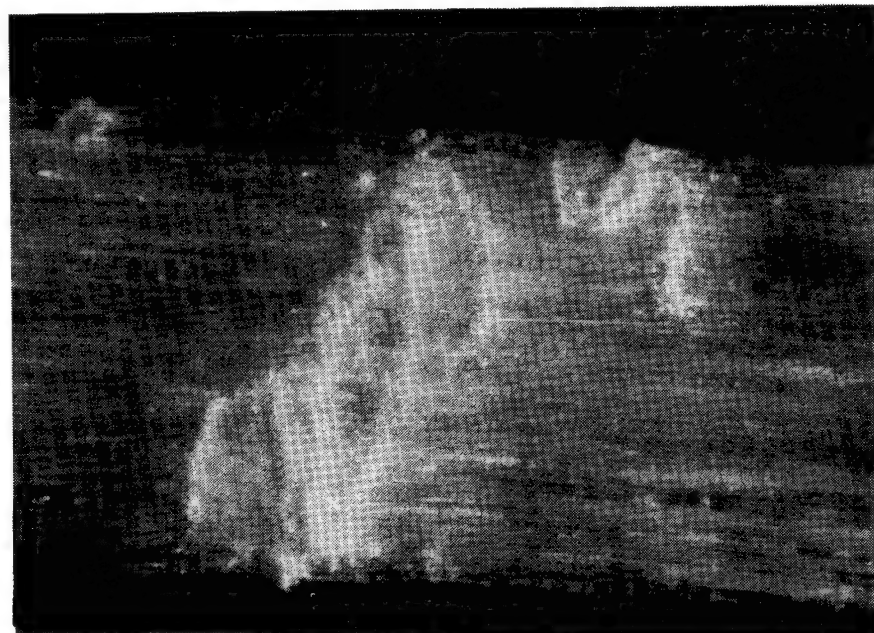


Figure 3. Localized buckling of E-glass bundle in Epon 815/V140 (180 X).

failures in Epon 815 and Epon 828.

The failure of the T300 graphite fiber bundle in Epon 815 is similar to that of the E-glass bundle in Epon 828. However, the failure zone of the T300 bundle in Epon 828 is much narrower. Also, there is very little indication of failure for the bundle in Epon 828. Rather, only a thin dark line indicates failure of the bundle, Figure 5.

The high-strain T700 graphite behaves similarly to the T300 graphite: the failure is localized and Epon 828 results in a smaller failure zone than Epon 815.

FP alumina fibers in Epon 815 also failed catastrophically and without any warning. The failure zone was quite localized yet clearly visible, Figure 6.

Failure of P75 graphite and Kevlar 49 fibers, however, was difficult to detect because it occurred gradually. These fibers failed early in the form of kinking of fibrils at many locations over their length. Since each failure zone was minute, failure was visible only when the lighting was incident at an acute angle with the fibers. Figure 7 shows failed Kevlar 49 fibers in Epon 815. The white bands inclined about 30° to the bundle axis are the kink bands. These kink bands in the bundle are the result of compressive failure of the fibers themselves. The compressive failure of fibers takes the form of kinking of fibrils in high-modulus graphite fibers [22] and Kevlar fibers [22,25].

After compression tests, one specimen from each group was cracked open along the bundle. The SEM micrographs of E-glass bundles clearly show a buckling-induced failure, Figure 8; the broken fiber segments are seen to have rotated and the broken ends are mostly square. Buckling is over a

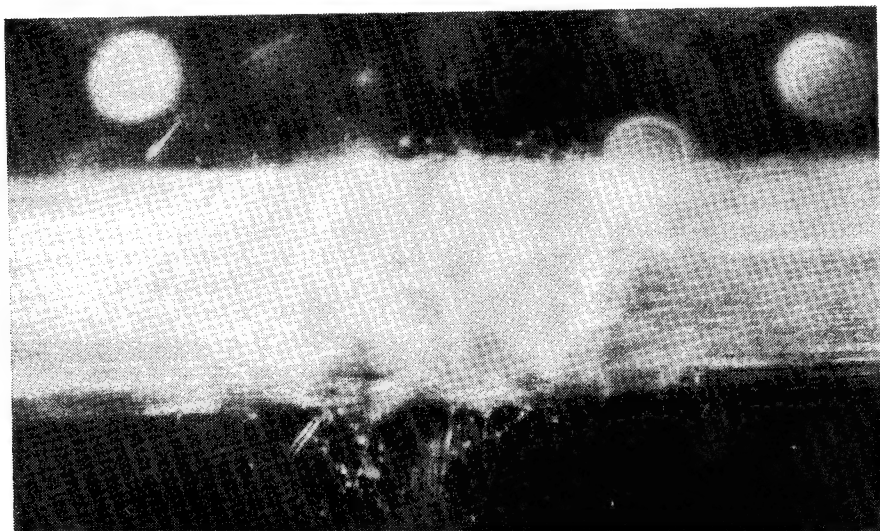


Figure 4. Localized buckling of E-glass bundle in Epon 828/Z (180 X).

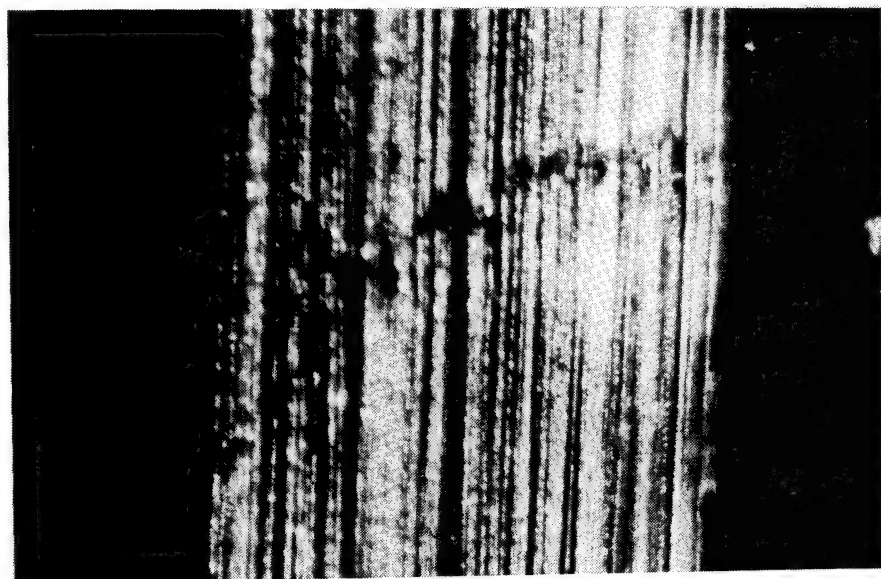


Figure 5. Localized failure of T300 graphite bundle in Epon 828/Z (180 X).

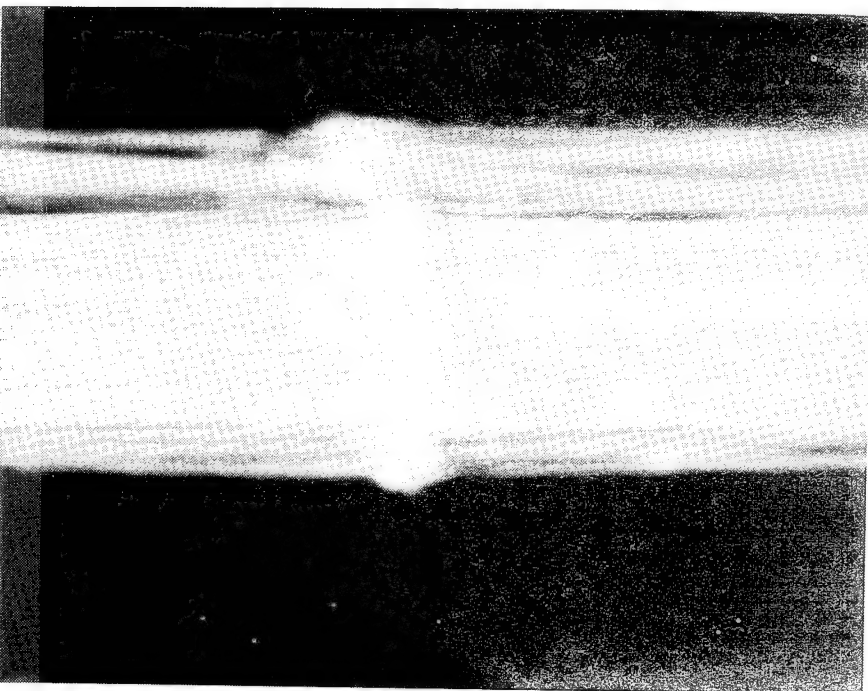


Figure 6. Failure of FP fiber bundle in Epon 815/V140 (180 X).

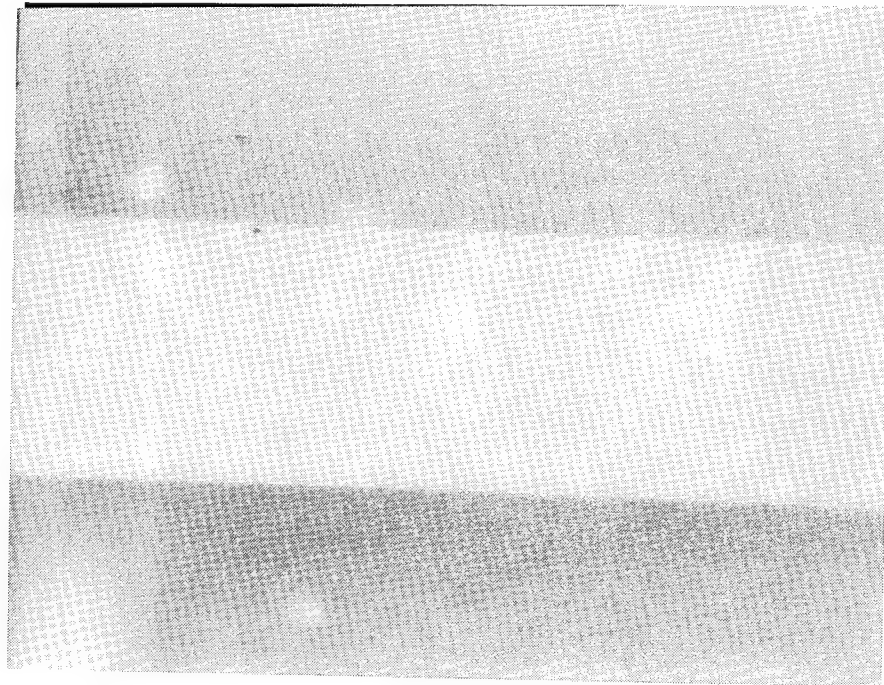
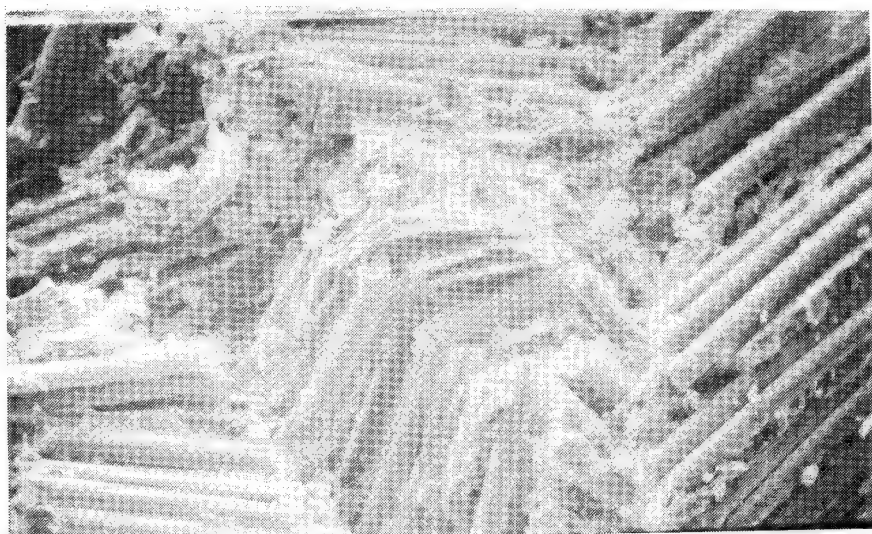
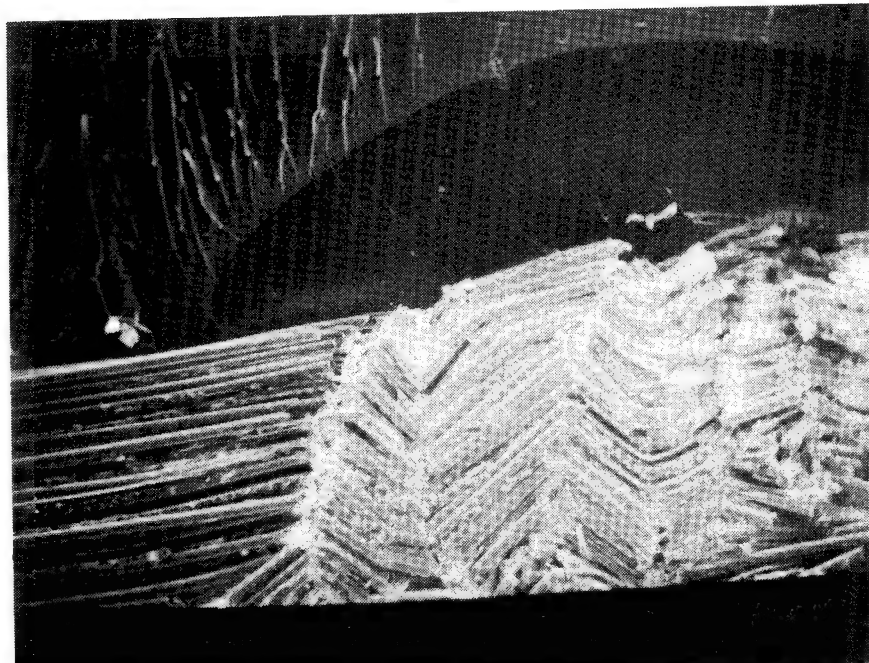


Figure 7. Failure of Kevlar fiber bundle in Epon 815/V140 (180 X).



(a)



(b)

Figure 8. SEM micrographs of E-glass bundles:
(a) Epon 815/V140; (b) Epon 828/Z.

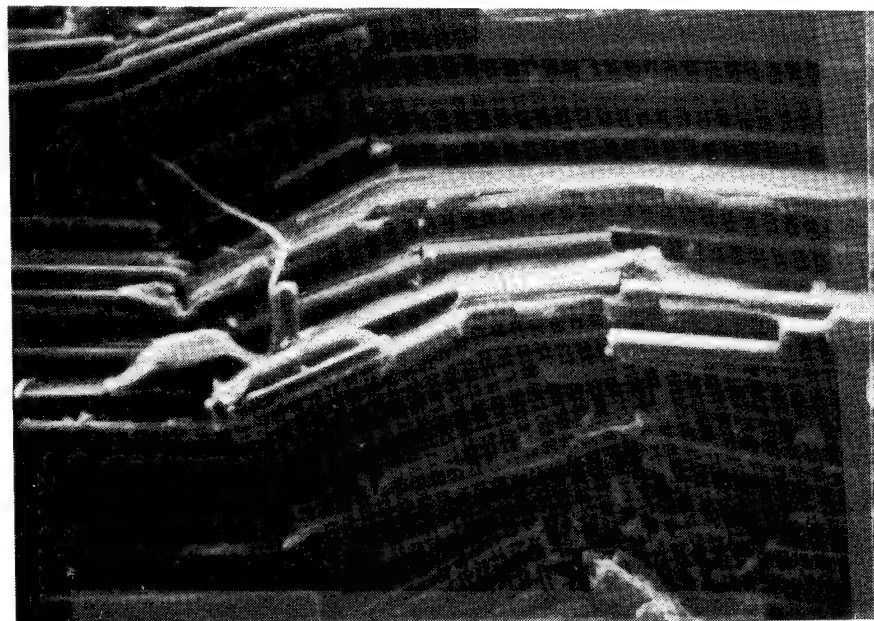
distance of several wave lengths. Not much difference is seen between the two resins.

As mentioned earlier, the T300 graphite bundle shows more localized failure than does the E-glass bundle, Figure 9. Furthermore, failure is more of a kinking type; that is, there is a transverse movement across the failure band. Such behavior is not surprising for the following reasons. Just like the failure initiation under tension, microbuckling will occur first at the weakest point. If fiber fracture does not follow immediately, buckling will spread along the fiber axis. Since graphite fibers have lower tensile failure strain than glass fibers, the former are more likely to fail immediately after buckling, thereby reducing the fiber stress. This may explain why the kinking type of failure is observed in the graphite bundle.

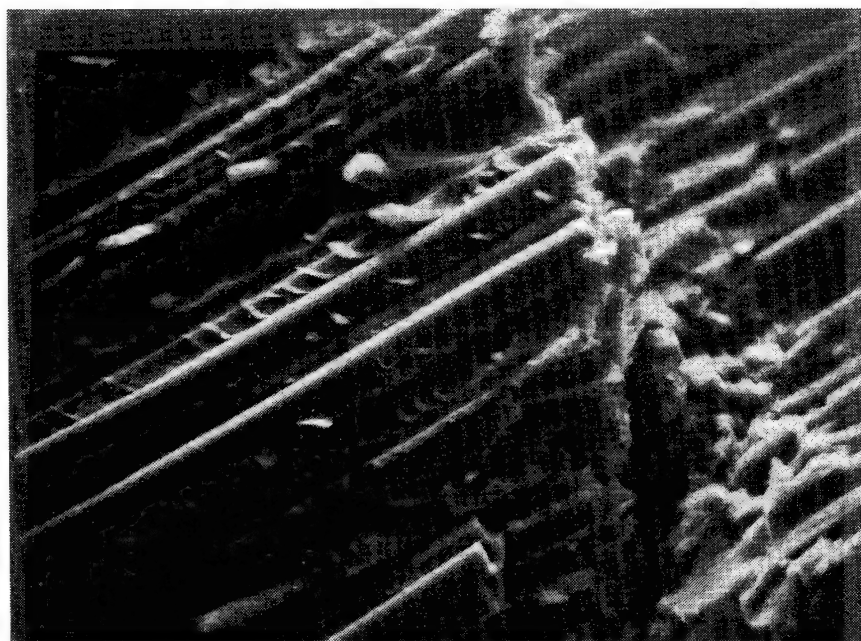
The failure modes of T700 fibers observed in SEM micrographs are similar to those of T300 fibers, Figure 10. FP fibers also failed in microbuckling, Figure 11 (a). Some fibers show splitting through the center, resulting in a step-wise fracture surface, Figure 11 (b).

The high-modulus P75 fibers failed in shear without buckling; slanted fracture surfaces are seen in Figure 12. Even after failure, the fibers remain straight without rotation or curvature. A closer examination of the fracture surfaces reveals that the failure of P75 fibers is really due to kinking of fibrils, Figure 12(b). It should be noted that the P75 fiber has a highly oriented structure and thus behaves like a unidirectional composite on a microscopic scale.

The failure of Kevlar 49 fibers is similar to that of P75 fibers; however, the failure in the former does not involve fracture, but sharp bending of fibrils. The kinking of fibrils on a 45° plane in Kevlar 49

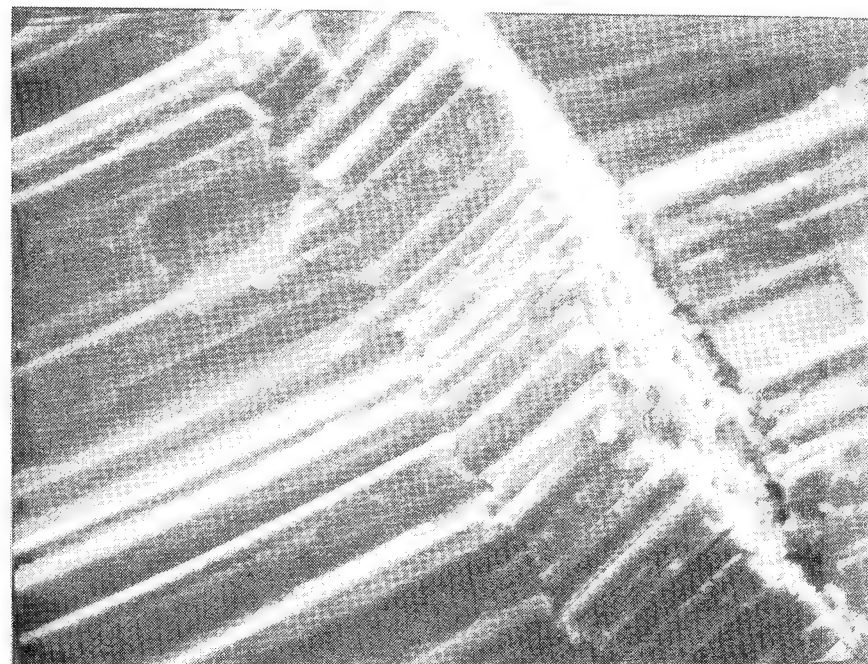


(a)

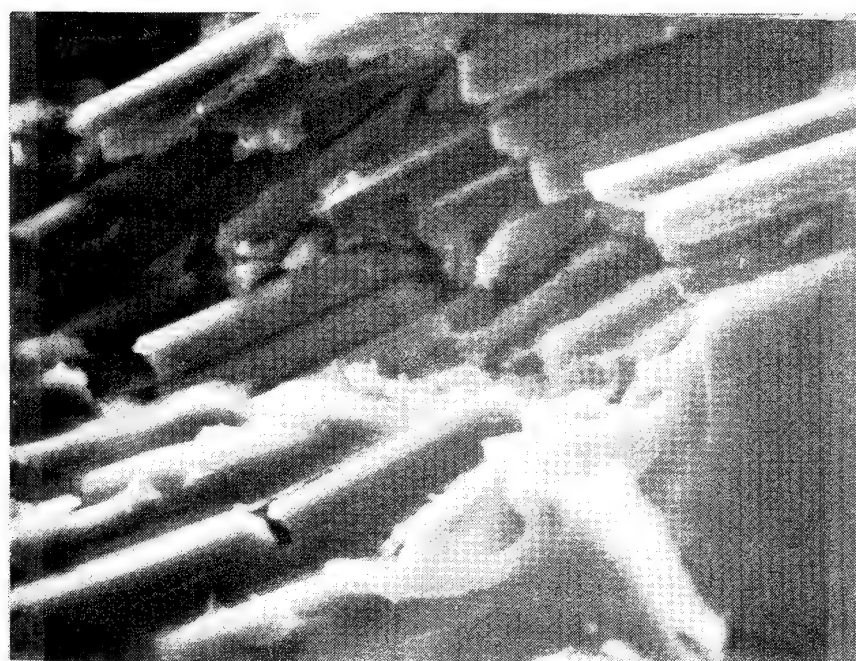


(b)

Figure 9. SEM micrographs of T300 graphite bundles:
(a) Epon 815/V140; (b) Epon 828/Z

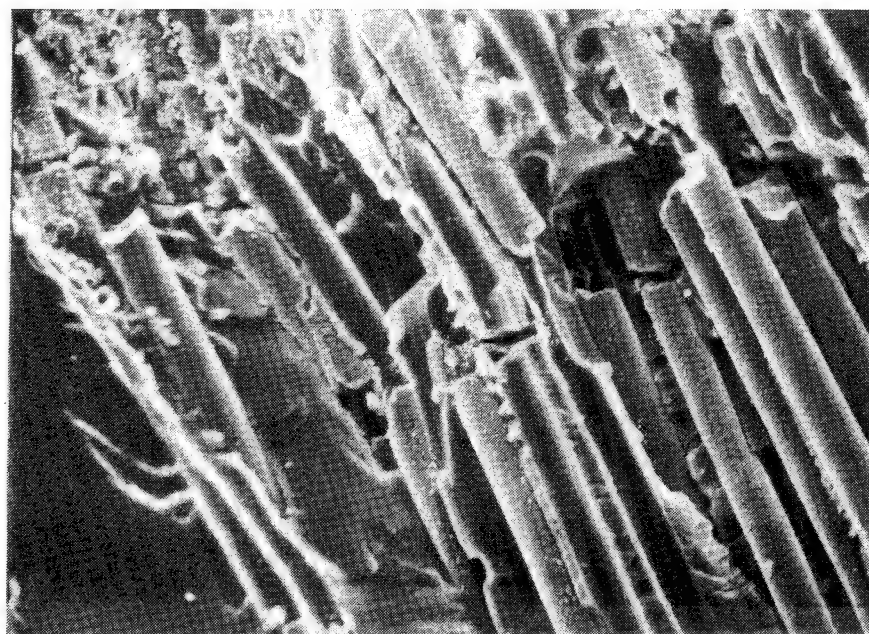


(a)

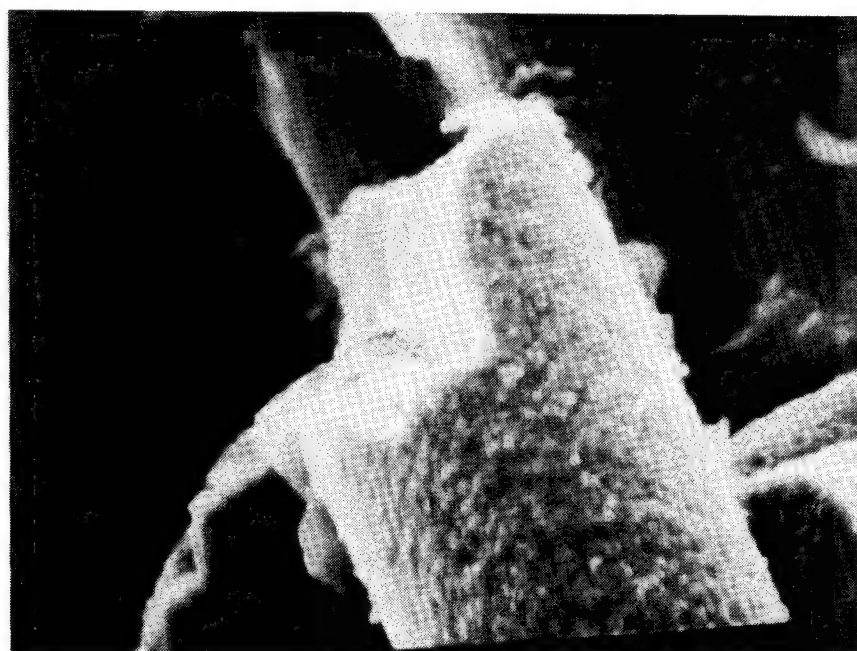


(b)

Figure 10. SEM micrographs of T700 graphite bundles:
(a) Epon 815/V140; (b) Epon 828/Z.

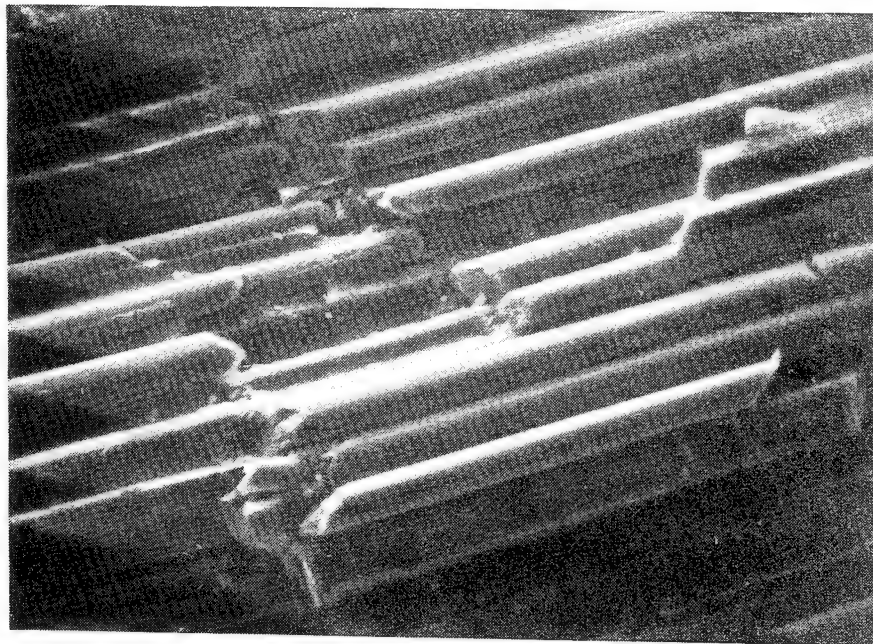


(a)

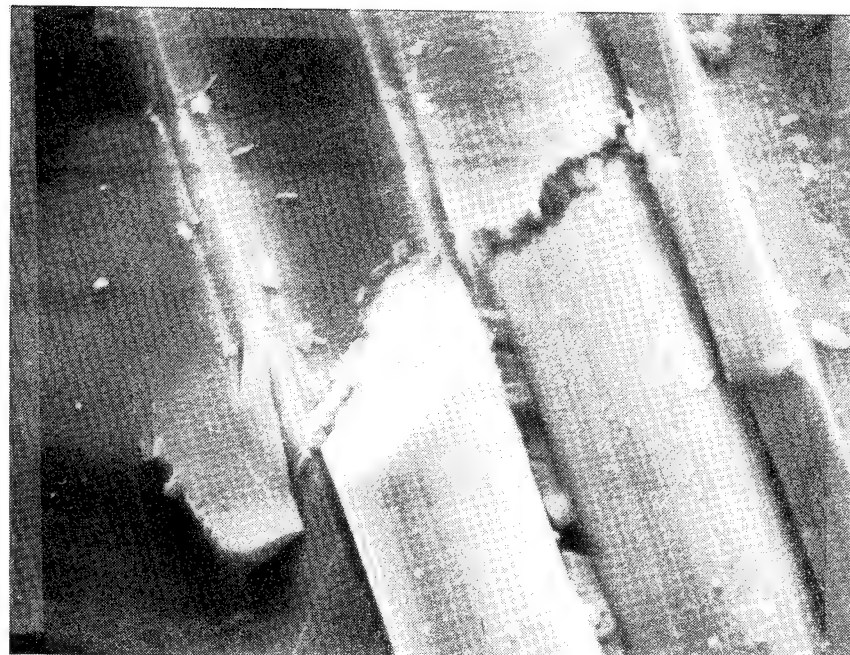


(b)

Figure 11. SEM micrographs of FP alumina bundle :
(a) bundle; (b) broken end.



(a)



(b)

Figure 12. SEM micrographs of P75 graphite bundles:
(a) Epon 815/V140; (b) Epon 828/Z.

fibers only slightly degrades the subsequent tensile strength of the fiber [23].

The apparent shear failure in P75 and Kevlar 49 fibers was quite uniformly distributed over the entire length, whereas the buckling failure of the other fibers was only at a few isolated sites along the bundle. In other words, the compressive failure of P75 and Kevlar 49 fibers is more like the multiple fracture that is frequently observed in the tensile testing of fibers embedded in resin.

The number of fiber breaks and the average length of each segment in a failure zone are shown in Figure 13. No data are shown for the FP fiber since the specimen that was cracked open and examined in SEM did not show enough broken segments. The geometrical details of the failure zone varies much more than could be described by average numbers alone. Yet, the data in the figure indicate an increase in the number of fiber breaks and segment length with increasing bundle failure strain.

As was seen earlier, the failure mode of P75 fibers is a single, slanted fracture surface. The failure of T700 fibers in both epoxies and T300 fibers in Epon 828 is characterized by double breaks in each filament, i.e., fiber kinking. The number of breaks increases to three for the T300 fibers in Epon 815. The E-glass bundle exhibits more than three breaks in each filament regardless of the epoxy type. The length of each segment also increases with the number of breaks.

2.4 Failure Strains

Typical stress-strain curves for Epon 828 specimens of IITRI type are shown in Figure 14 , where buckling of the bundle is seen to occur when the

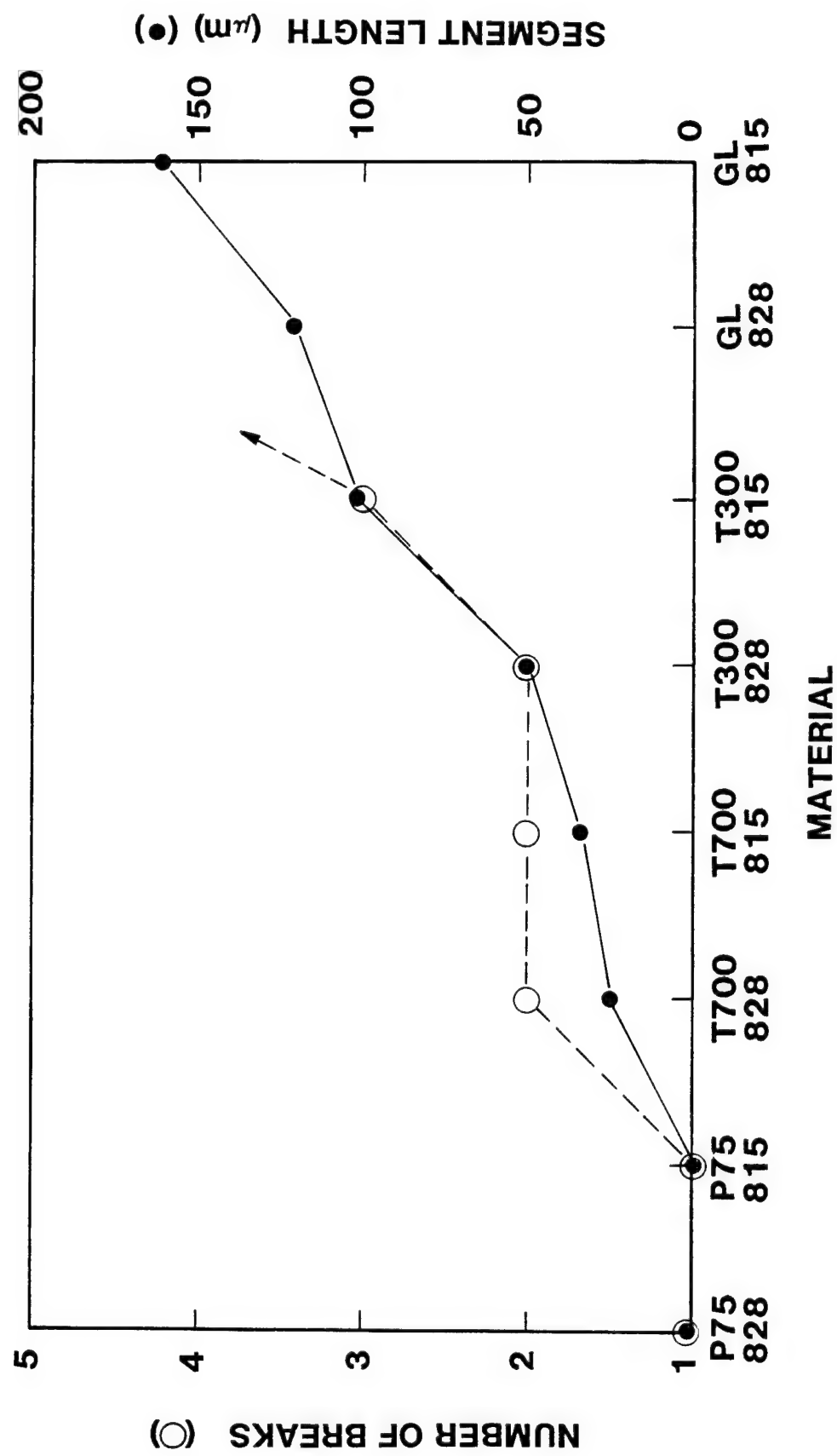


Figure 13. Number of fiber breaks and average segment lengths.

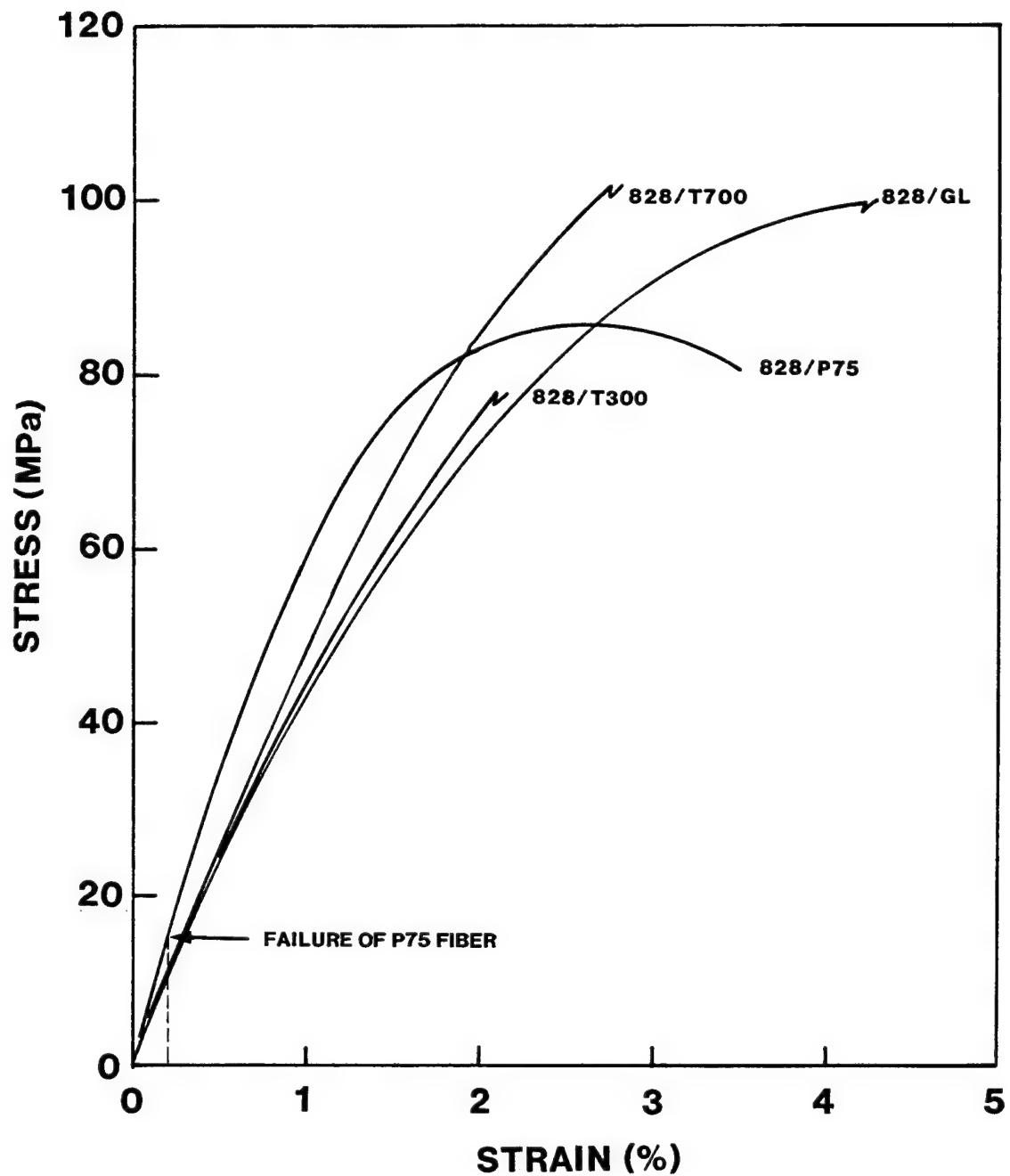


Figure 14. Stress-strain curves for Epon 828/Z specimens with embedded fiber bundle.

resin is in the nonlinear range. Since the average fiber volume content is on the order of 0.4%, fibers do not appreciably affect the initial modulus: using the rule-of-mixtures and the properties defined in Tables 2 and 3 yield an initial modulus of 3.6 GPa for E-glass, 4.2 GPa for T300 and T700 graphite, and 5.5 GPa for P75 graphite. Similar stress-strain relations but with lower moduli were obtained for Epon 815.

As mentioned earlier, the failure of P75 fibers did not result in a sudden drop in stress, Figure 14. Rather, the tangent modulus changed only slightly. The change was more distinctive in Epon 815 than in Epon 828 because the former resin was softer.

The measured compressive strains at bundle failure are shown in Figure 15. The E-glass fiber bundle is seen to have the highest failure strain while the P75 bundle has the lowest. The high-strain T700 graphite bundle is slightly stronger than the T300. As expected from the buckling theory, the stiffer epoxy yields higher failure strains. However, the difference in failure strain due to resin stiffness for the T300 and T700 graphite fibers is much less than for the E-glass fiber, and disappears for the P75 fiber. Since the failure of P75 fibers is in shear without buckling, resin stiffness has no effect.

Fiber bundles having higher tensile failure strains are seen to buckle at higher compressive strains, Figure 16. The P75 fiber is weaker in compression than in tension. However, both T300 and T700 fibers are stronger in compression. The E-glass fiber is slightly weaker in compression.

Buckling of a single fiber embedded in matrix has been analyzed in the literature [26-28]. The approximate analysis in [28] indicates that the

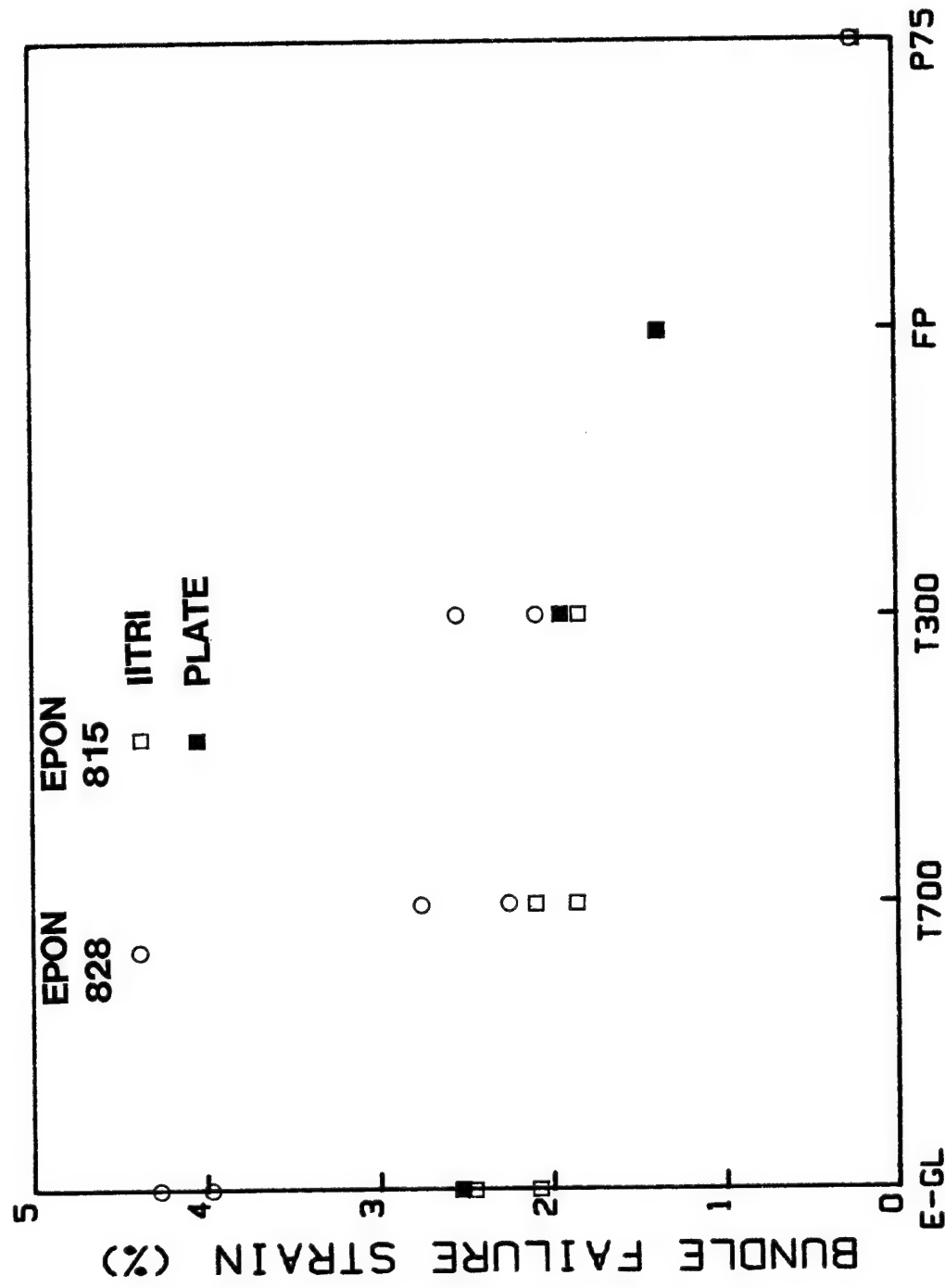


Figure 15. Compressive failure strains of bundles.

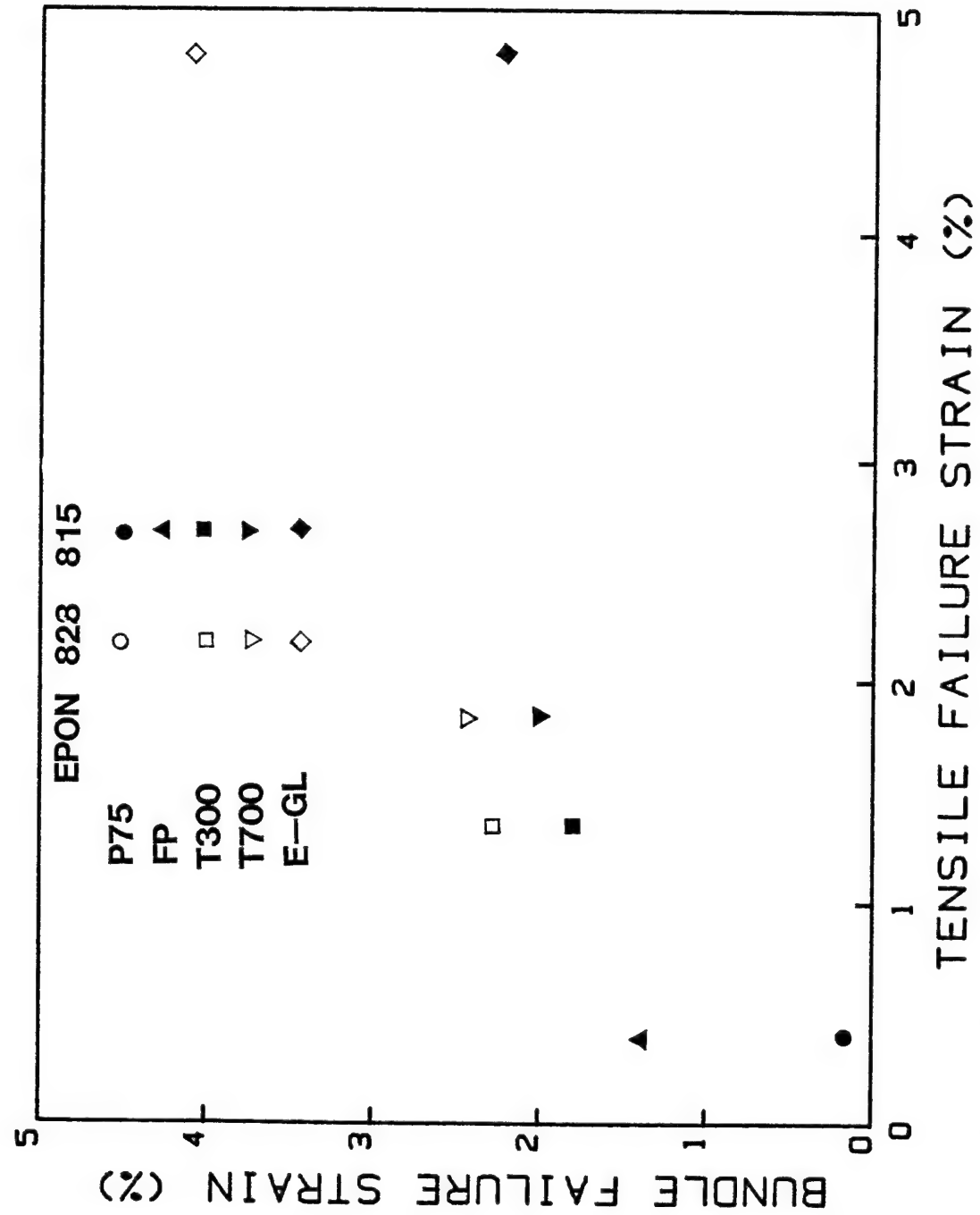


Figure 16. Compressive failure strain as a function of fiber tensile failure strain.

buckling strain and the buckle wavelength of the fiber are related to the moduli E_m , E_f , and the fiber diameter d_f by

$$\varepsilon_b \propto (E_m/E_f)^{1/2} \quad (1)$$

$$\lambda \propto (E_f/E_m)^{1/4} d_f \quad (2)$$

where the subscripts m and f denote matrix and fiber, respectively.

Figures 17 and 18 show that the present data follow the trends predicted by Eqs. (1) and (2), although a bundle of fibers rather than a single fiber was used. The buckling strain is seen to be proportional to the square root of the matrix-to-fiber modulus ratio. The segment length increases linearly with fiber diameter and with the quadratic root of the fiber-to-matrix modulus ratio although the relationship does not go through the origin.

2.5 Detection of Subcritical Failure by Acoustic Emission

Since optical microscopy did not reveal any subcritical failures, the acoustic emission (AE) technique was used to monitor failure sequence in the plate specimens. The preset AE parameters listed in Table 4 were sufficient to avoid noise and record almost all legitimate emissions. The threshold voltage was set at 0.3 volts, and the total amplifier gain at 90 dB including 60 dB at the preamplifier. Acoustic emission parameters such as events, mean ringdown counts, mean peak amplitude, and mean event duration were recorded against time and strain. Distrubutions of peak amplitudes were also obtained.

Figure 19 shows stress and cumulative events versus strain for a net resin specimen under compression. The stress-strain curve is linear up to

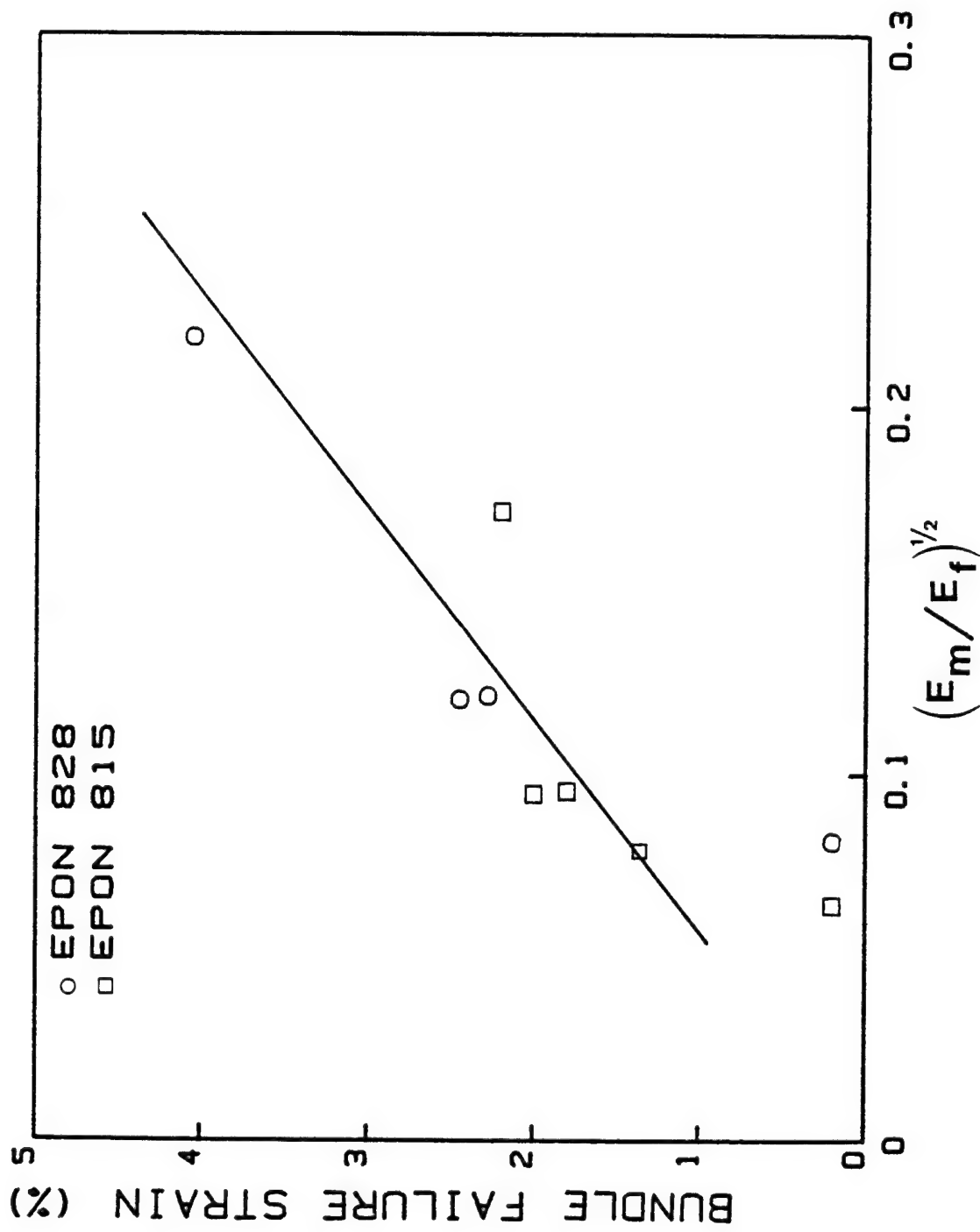


Figure 17. Compressive failure strain increasing with square root of matrix-to-fiber modulus ratio.

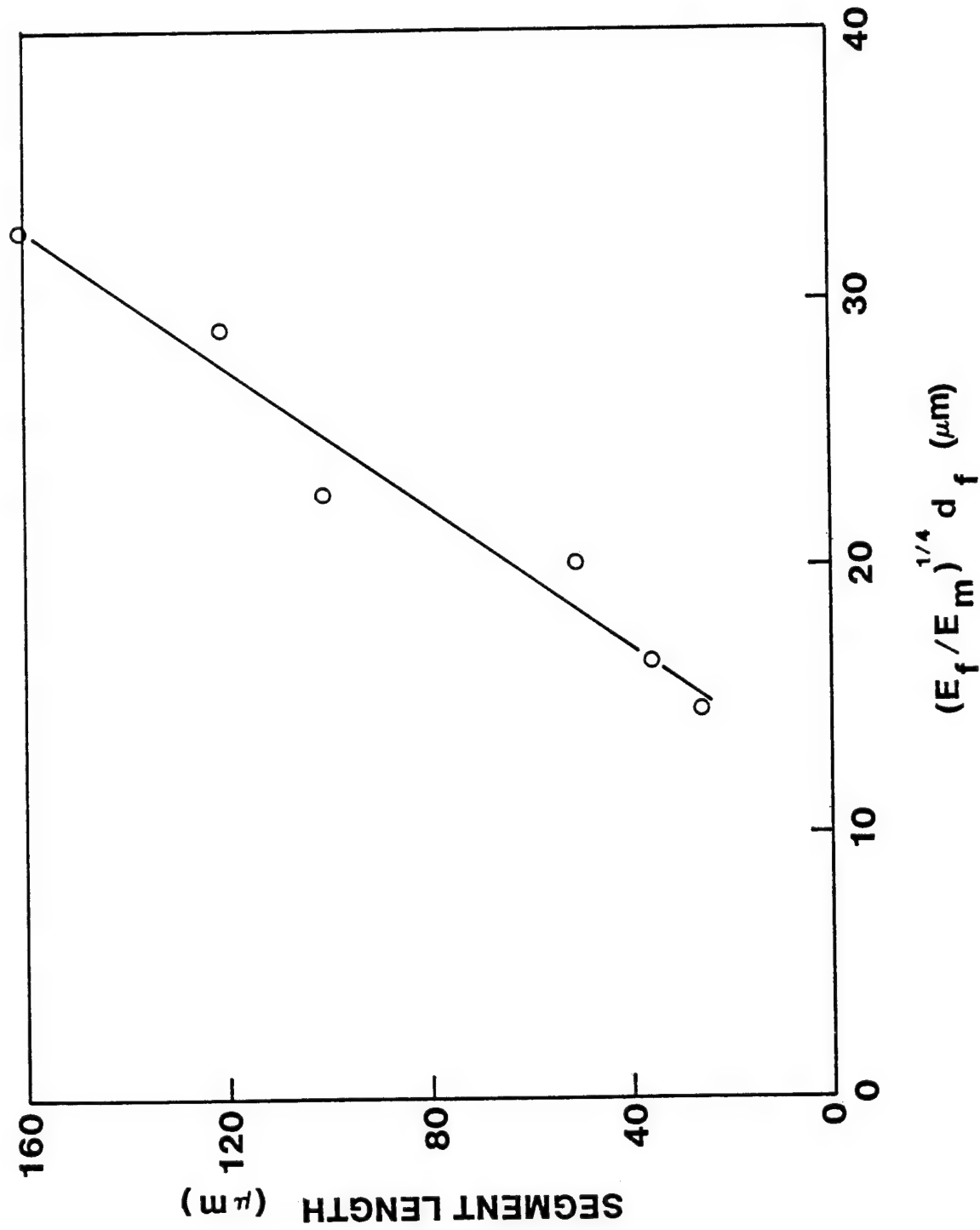


Figure 18. Average segment length increasing with quadratic root of fiber-to-matrix modulus ratio and with fiber diameter.

TABLE 4. Acoustic Emission Preset Parameters

Preamplifier Gain	60 dB
Amplifier Gain	30 dB
Threshold Voltage	0.3 Volts (fixed)
Event Duration clock	125 ns
Rise time clock	125 ns
Reject Criteria:	
-Ringdown count	$1 < n < 4095$
-Peak Amplitude	$5 < I < 64$ dB
-Event Duration	$1 < T < 480 \mu\text{s}$
-Rise Time	$1 < RT < 480 \mu\text{s}$
-Slope	$0 < S < 65520 \text{ dB}/\mu\text{s}$

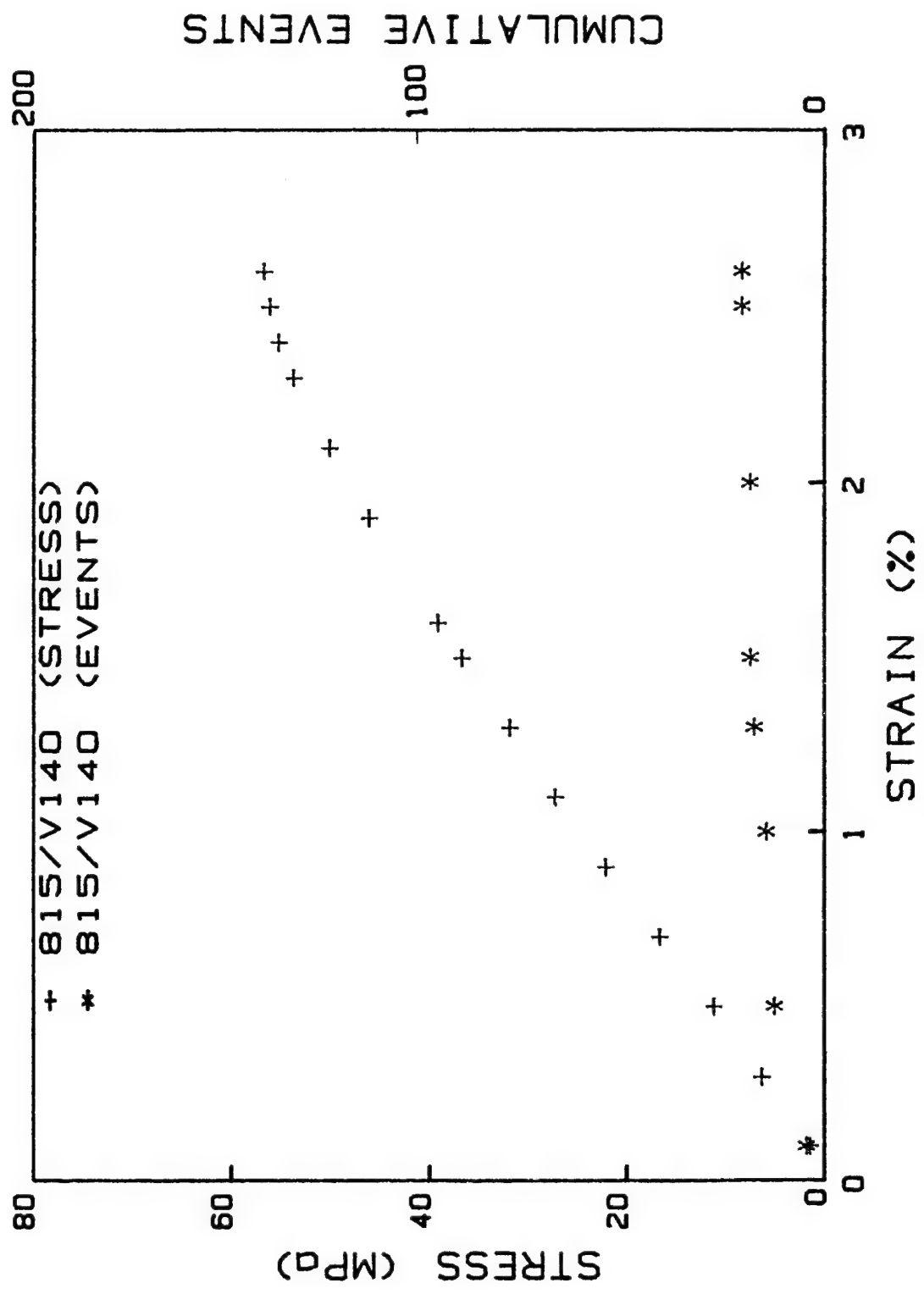


Figure 19. Stress and cumulative events vs. strain for Epon 815/V140.

1% strain, after which it becomes slightly nonlinear. At 2.6% strain the specimen started to yield. The total number of acoustic emission events recorded up to yielding is only 20, indicating that the resin is not very acoustically active in compression. Moreover, there were no events rejected by the AET system because of the preset parameters.

Acoustic emission events start quite early and increase rapidly with increasing strain in the presence of a glass bundle embedded in the resin, Figure 20. In fact, the total number of events for the neat resin alone is exceeded at a strain as low as 0.3-0.35%. A large burst of emissions is recorded at the time of visible bundle failure, which was also indicated by an abrupt drop in load in the load-strain plot.

Failed specimens were examined on an optical microscope to locate the probable sources of acoustic emissions. It was found that there was debonding and failure of the bundle at both loading ends in addition to the bundle failure in the gage section. A careful observation of another specimen during loading revealed that debonding was initiated at the loading ends and propagated along the bundle. However, before debonding could propagate well into the gage section, fibers at the ends had failed. The bundle failure in the gage section occurred much later.

Acoustic emissions emanating from debonding were shown by Rothwell using a single filament embedded in an epoxy block with curved neck [11]. However, with the end failure just described it was not clear whether or not some emissions were from debonding in the gage section. As a first step to answer this question, the quality of fiber-matrix bonding was examined on the cross section of a virgin specimen. The resulting SEM micrograph of Figure 21 (a) shows debonding, and hence indicates a poor interfacial

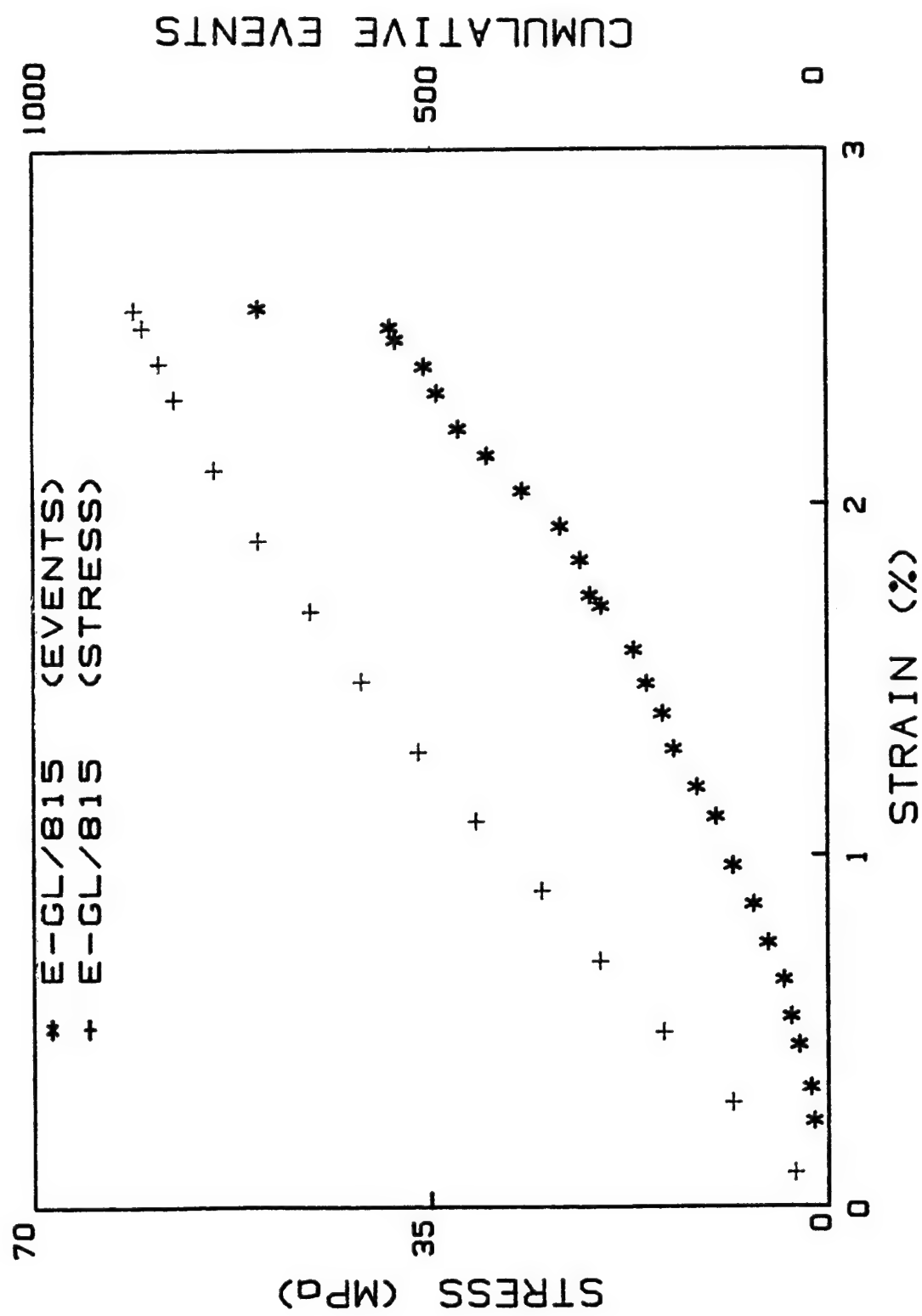
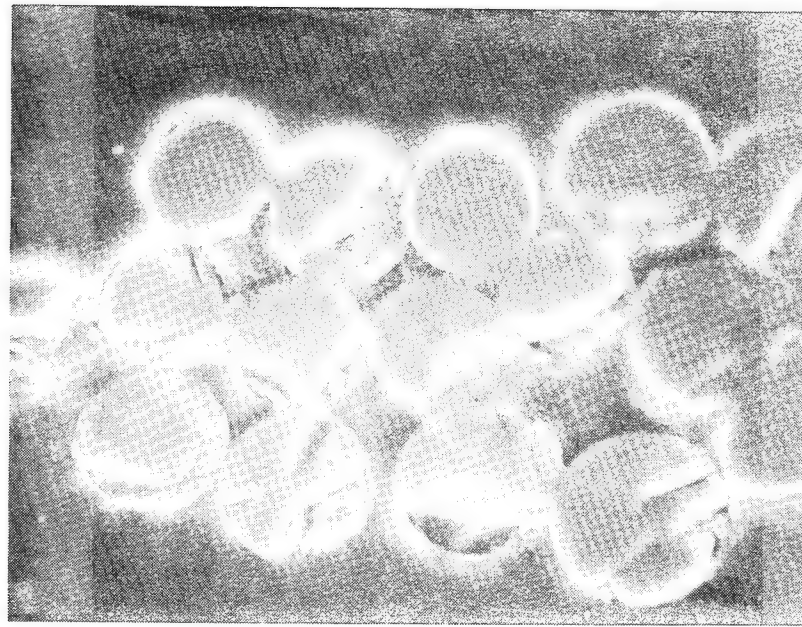
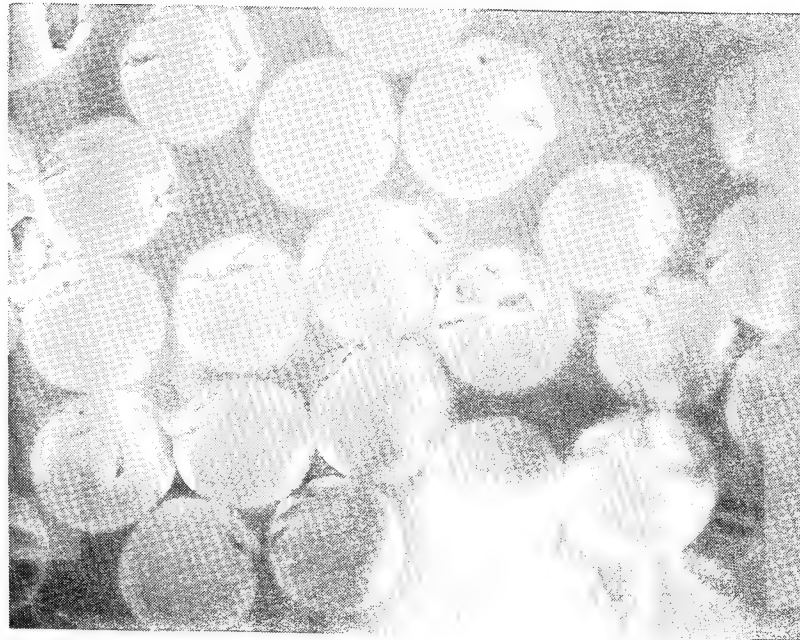


Figure 20. Stress and cumulative events vs. strain for E-G1/815.



(a)
POOR BONDING



(b)
GOOD BONDING

Figure 21. SEM micrographs of specimen cross-sections:
(a) poor bonding (1000X);
(b) good bonding (1000X).

strength in the specimen. To improve bonding, fiber bundles were dried at 300° F for 10 min, and then embedded in the resin. The resulting specimens had much better bonding, as indicated by the SEM micrograph of Figure 21(b). Improved bonding was expected to reduce the acoustic emission response. The comparison shown in Figure 22 shows the acoustic emission events for the improved bond specimen to start later (i.e. at a higher load) and have a higher occurrence rate at higher loads.

In order to prevent the end failure, a few specimens had their loading ends potted in the same resin. The resin was cured at room temperature for 48 hours. The potted region was 14 mm long by 9 mm thick whereas the gage section was 18 mm long by 3.5 mm thick. Figure 23 shows much fewer events for the specimens with potted ends. Improved bonding does reduce emissions somewhat. In both Figures 22 and 23, the burst of emissions indicates failure of the bundle and the bundle with good bonding had not failed when the test was stopped. Thus, regardless of the quality of bonding, most debonding is concluded to occur just before the bundle failure. Photographs of Figure 24 compare a virgin specimen with a failed specimen with extensive debonding.

Acoustic emissions in the FP alumina specimen start early and increase rapidly with increasing strain, Figure 25. Most of emissions are also believed to be from debonding and fiber failures at the ends because this specimen also showed end failure. Again, the biggest jump in AE occurs at the time of bundle failure in the gage section.

The T300 graphite specimen behaves similarly to the glass specimen, Figure 26. The cumulative events in the graphite specimen stay lower than in the FP specimen. Since the same type of end failure was observed in the

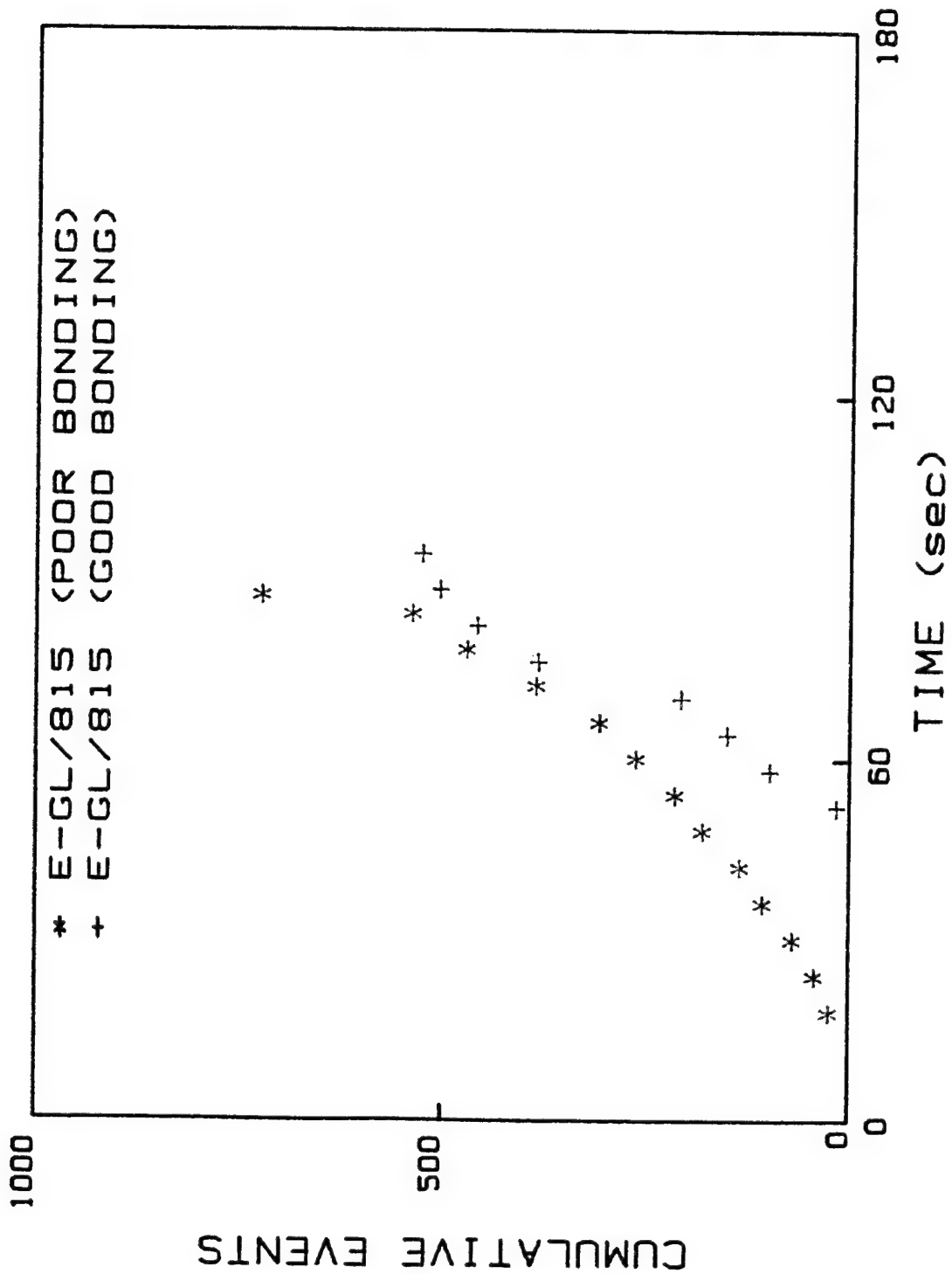


Figure 22. Cumulative events vs. time for E-GL/815 with good and poor bonding.

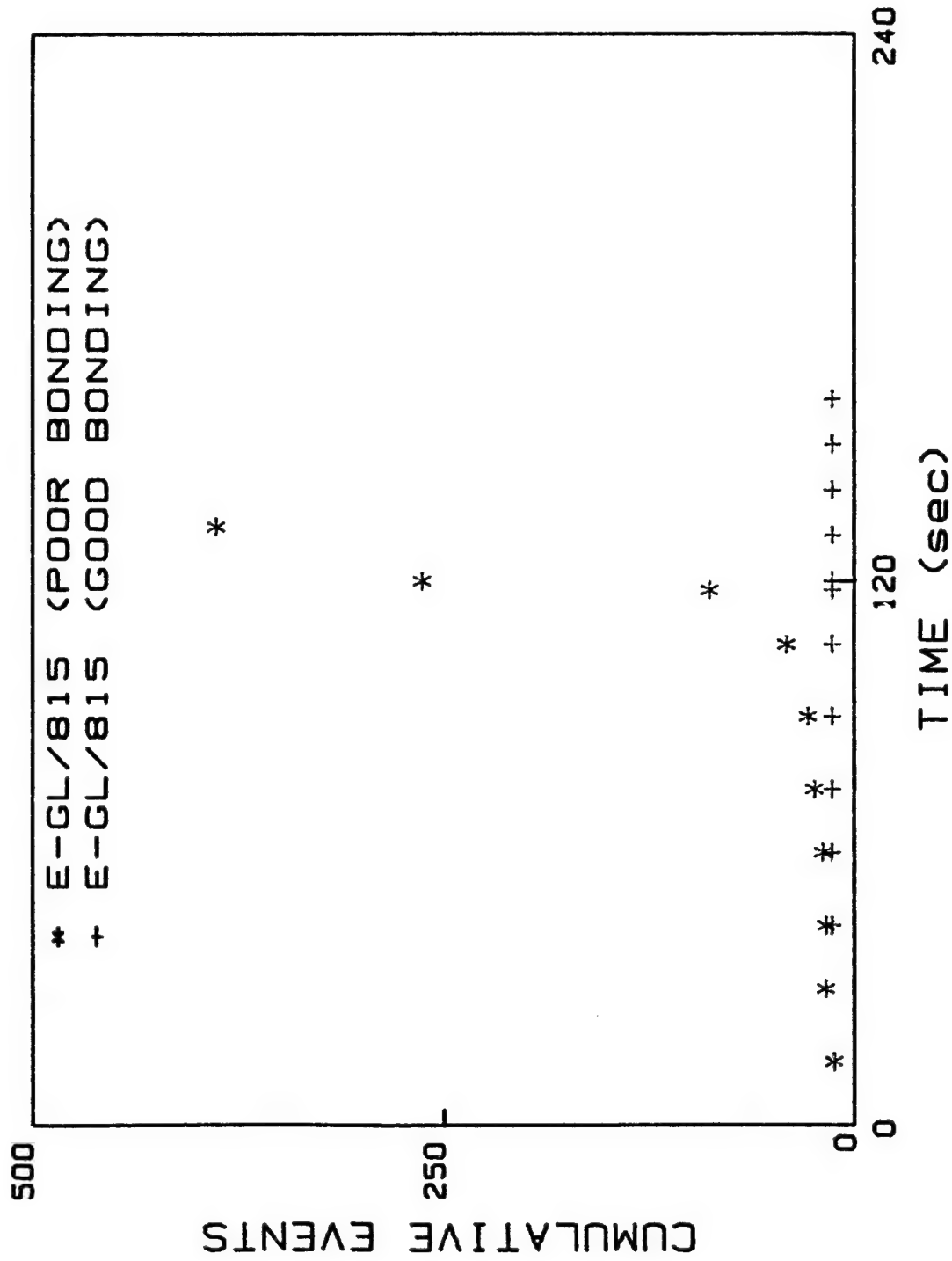
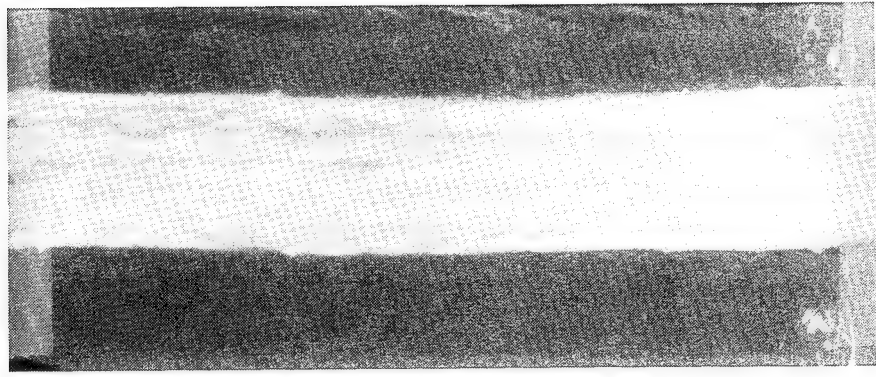


Figure 23. Cumulative events vs. time for potted E-G1/815 specimens with good and poor bonding.

FAILED



VIRGIN

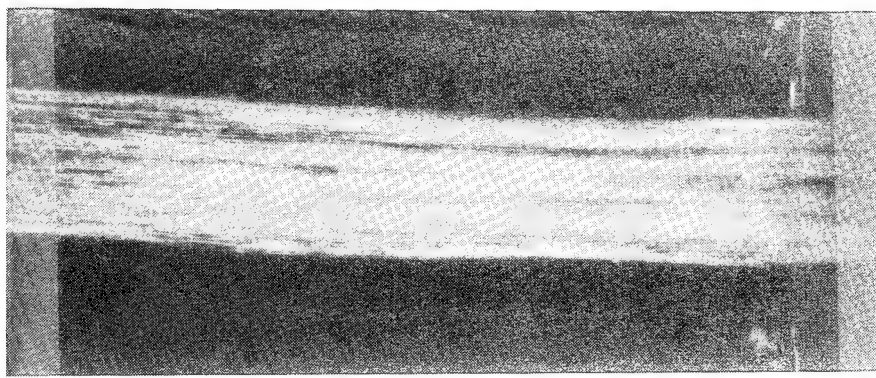


Figure 24. (a) A virgin specimen; (b) extensive debonding in failed specimen.

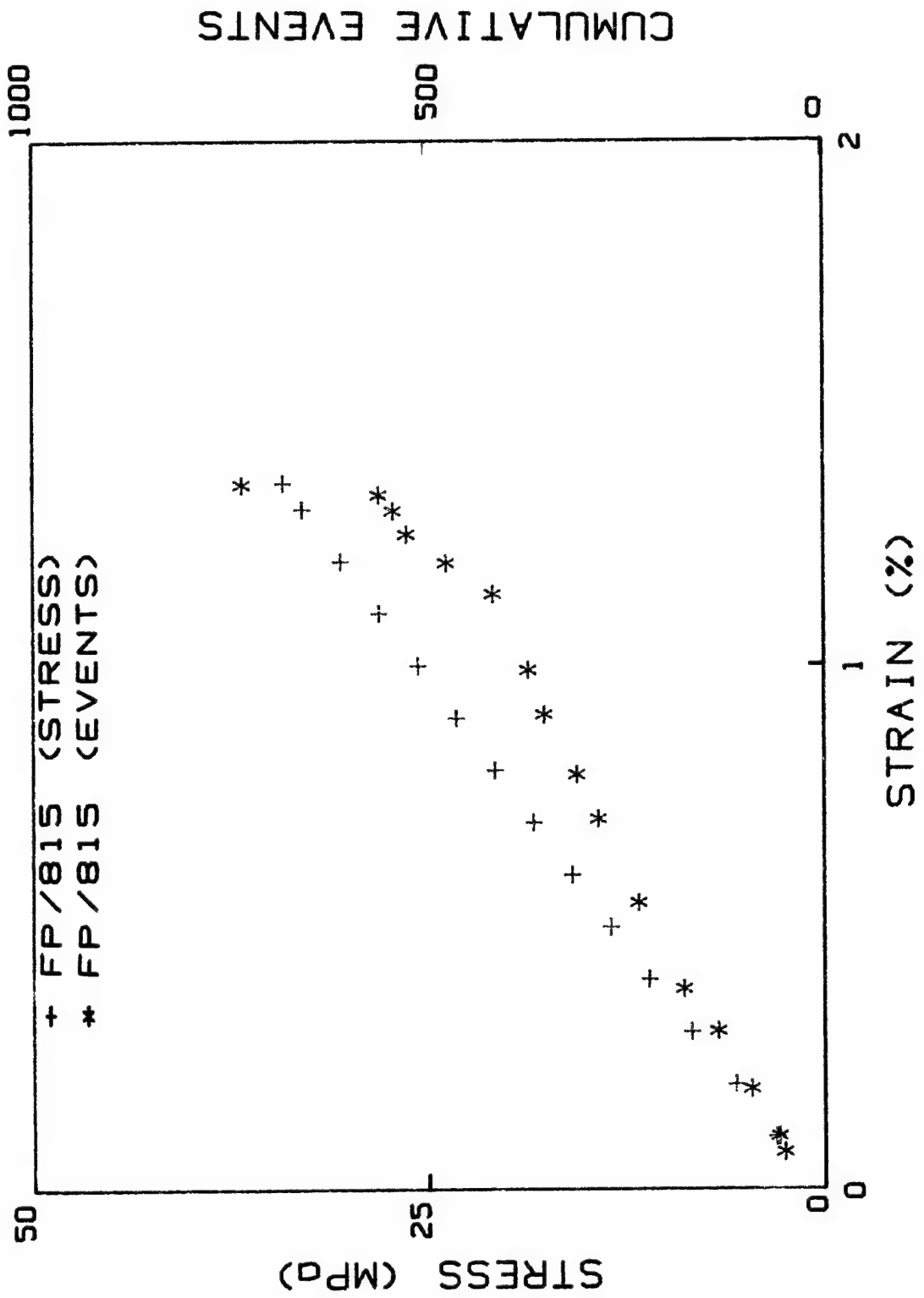


Figure 25. Stress and cumulative events vs. strain for FP/815.

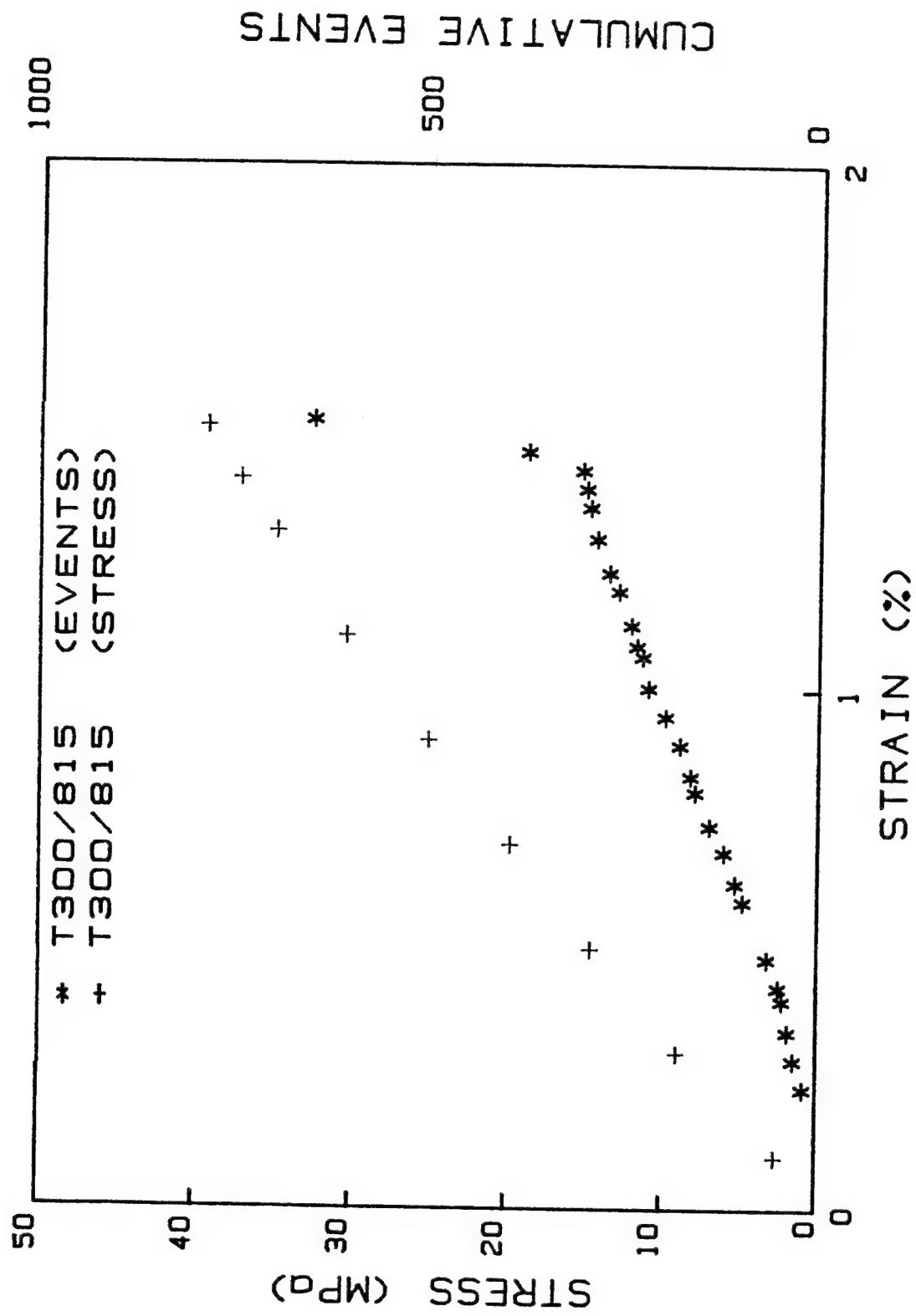


Figure 26. Stress and cumulative events vs. strain for T300/815.

graphite specimen also, it is expected to be responsible for most of the emissions.

Emissions in the Kevlar bundle specimen start early as in the other specimens, Figure 27. However, they increase much more rapidly with increasing strain than in any other specimen. Since Kevlar fibers themselves fail early in compression, as discussed previously, those emissions are from fiber failures and subsequent kinking in the bundle. Note that there is no sudden burst of emissions in contrast to the other specimens.

The acoustic emission behaviors of different fiber bundles discussed so far are compared with one another in Figure 28. At the same strain level, the Kevlar bundle is the most active acoustically while the E-glass bundle is the least. The T300 graphite bundle is only slightly more active than the E-glass except at failure. The alumina bundle is next to the Kevlar bundle in acoustic activity.

Emissions in the Kevlar bundle are from failure of fibers themselves. However, emissions in the remaining bundles are mostly from debonding and fiber failures at the ends. Since FP alumina fiber is the stiffest, the shear stress at the bundle-resin interface at the ends would be the highest in the FP bundle specimen. Therefore, for the same interfacial strength, the FP bundle would be more susceptible to interfacial failure at the ends than the other bundles. This argument based on fiber stiffness correctly predicts the ranking in acoustic activity shown in Figure 28.

Figure 29 shows variations of mean peak amplitude with time for the fibers studied. Except for the Kevlar bundle, emissions from debonding and fiber failure have higher peak amplitude than those in the neat resin. Since debonding occurs before fiber failure at the ends, the results for the

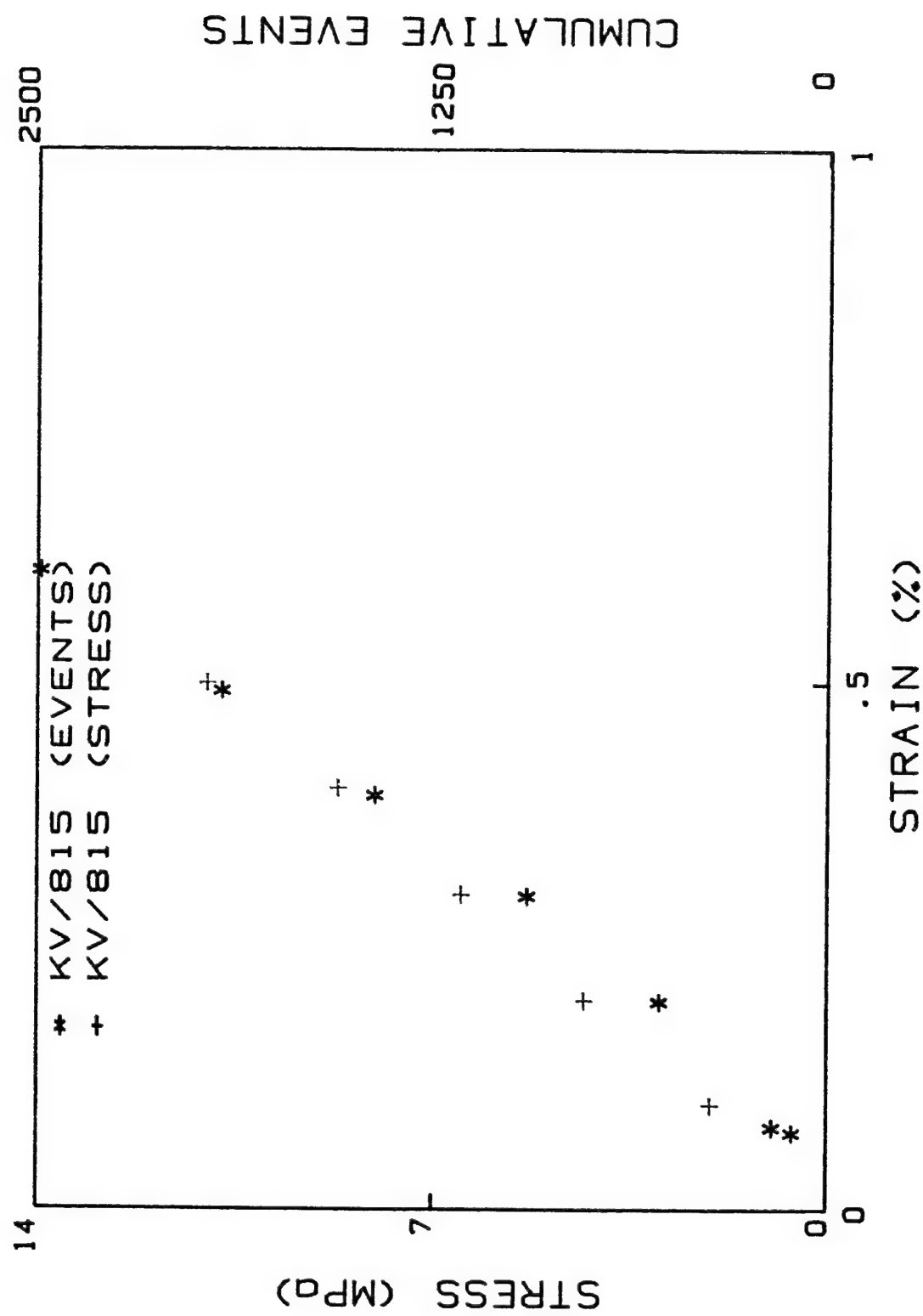


Figure 27. Stress and cumulative events vs. strain for KV/815.

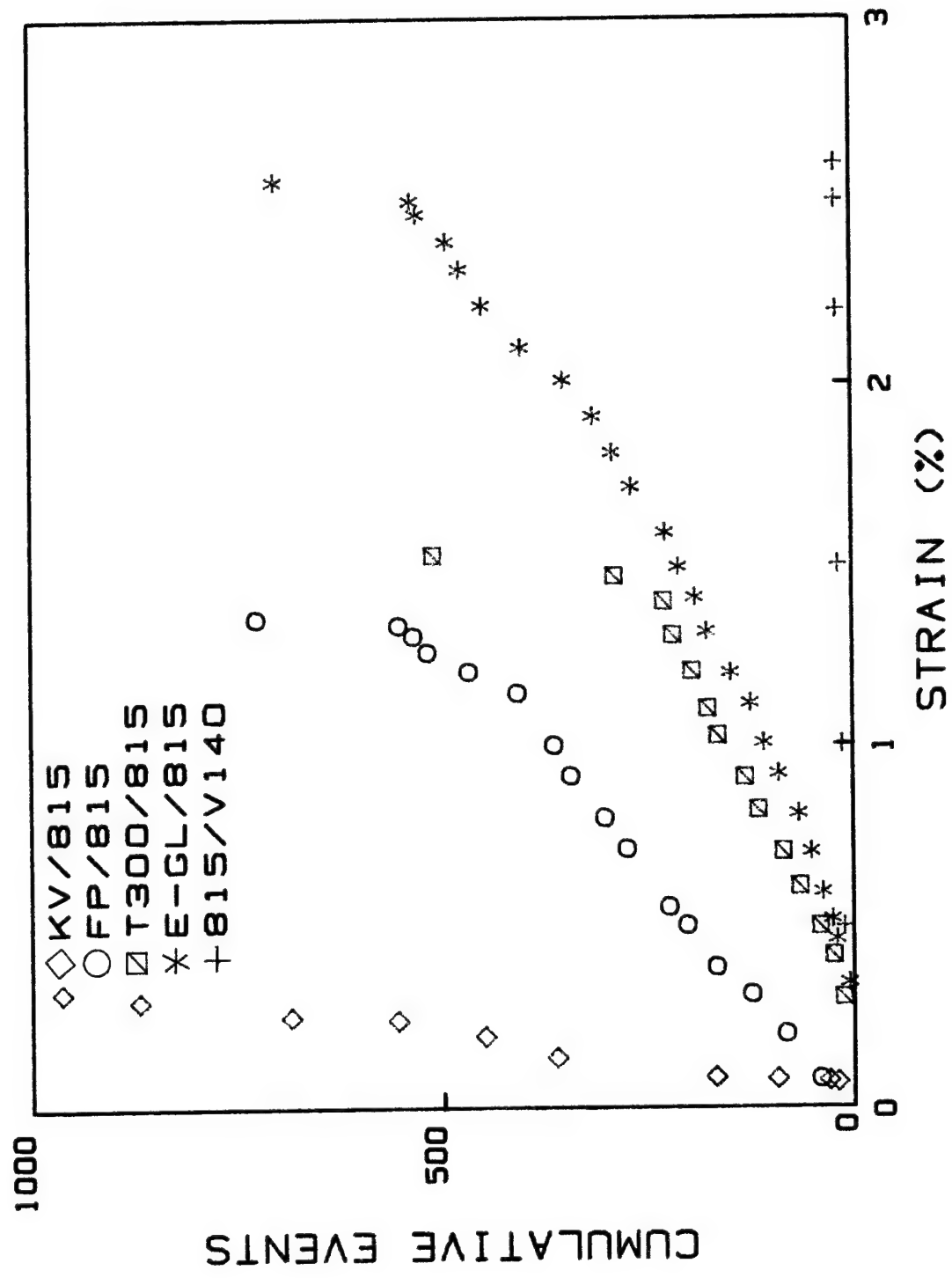


Figure 28. Comparison of acoustic emission activities for various embedded bundles.

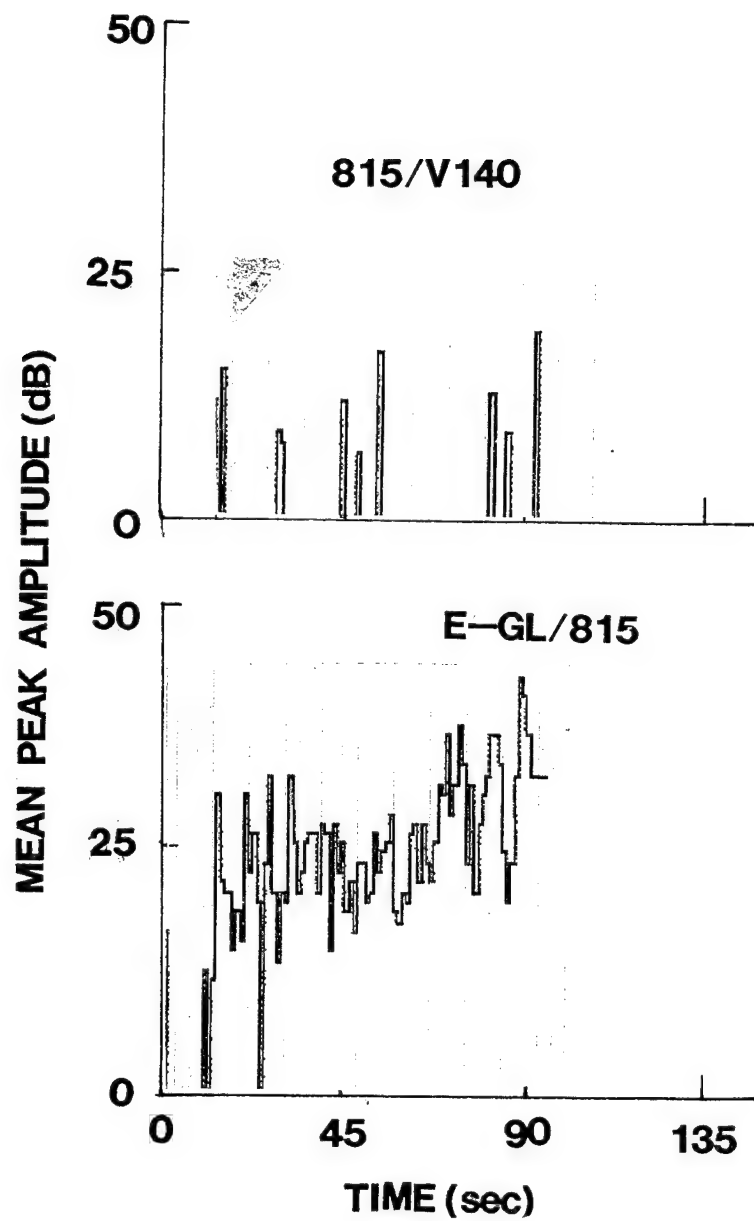


Figure 29 Mean peak amplitude vs. time for Epon 815 and for different fiber bundles embedded in Epon 815.

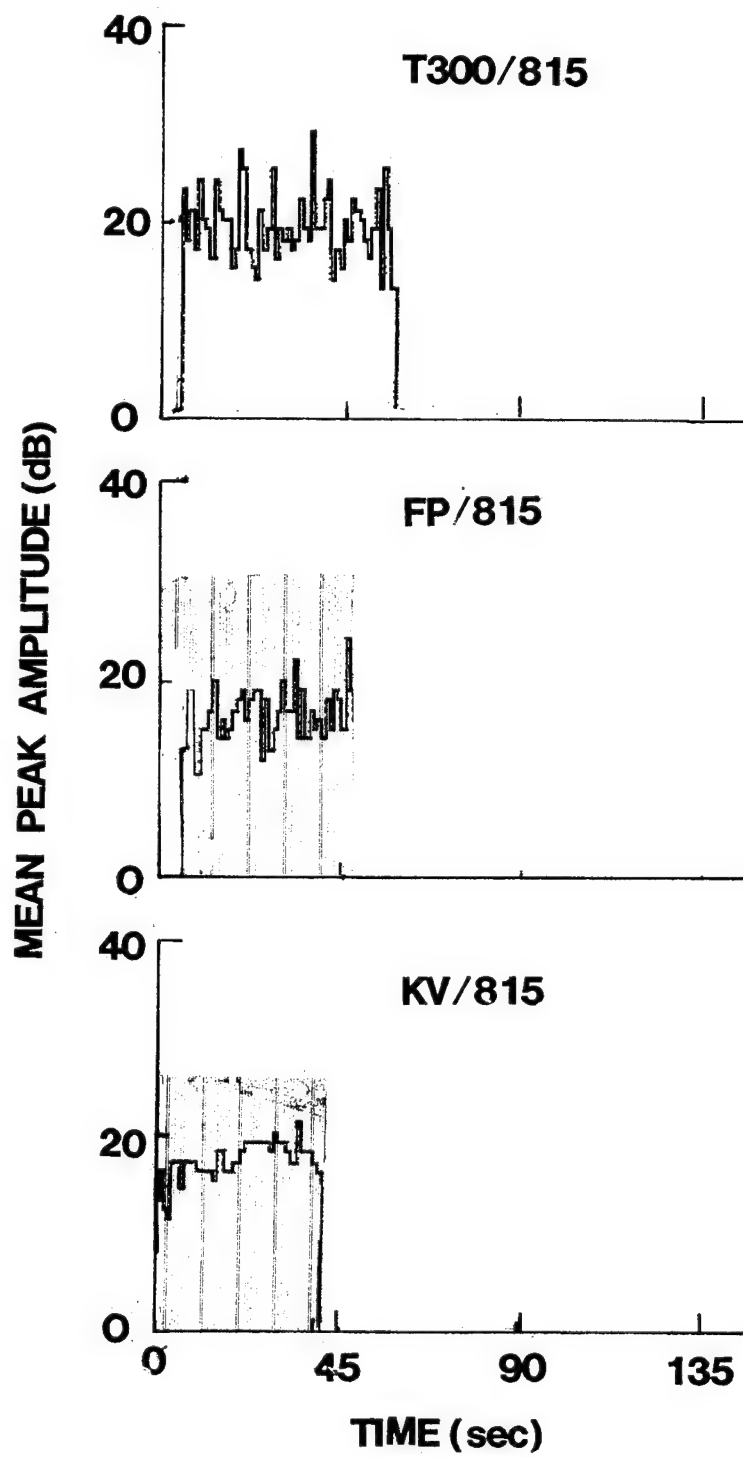


Figure 29.(continued)

glass and alumina bundles can be used to conclude that debonding produces emissions of lower peak amplitude than fiber failure. However, the same conclusion does not apply to the graphite bundle.

As for the ranking based on mean peak amplitude, the glass bundle is at the top while the Kevlar bundle is at the bottom. The graphite bundle shows slightly higher amplitudes than the alumina bundle. With the exception of the neat resin, the ranking based on mean peak amplitude is almost opposite to the ranking based on cumulative events.

2.6 Summary

The use of a fiber bundle embedded in a resin block can provide much needed information on compressive failure mechanisms in unidirectional composites because failure of the bundle is well contained and can be monitored during testing. The method can clearly distinguish between buckling-induced failure and intrinsic failure of fibers.

The present study indicates that the T300 and T700 graphite, FP alumina, and E-glass fibers all fail in microbuckling while the highly anisotropic P75 graphite and Kevlar 49 fibers fail by kinking of fibrils. Buckling of fibers could be uniformly distributed in an extremely soft resin, but it is quite localized in fairly stiff resins. Fiber fracture and debonding occur at the time of buckling.

Failure strains and segment lengths observed in bundle specimens follow the trends predicted for a single fiber embedded in an infinite matrix. With the exception of the P75 graphite and Kevlar 49, compressive failure strains of the fibers studied are higher than those of their composite counterparts. Therefore, compressive strengths of those fibers are not

fully utilized in the composites.

The acoustic emission technique can be used to detect failure of the embedded bundle. It can also detect such extraneous failures as bundle debonding and fiber fracture at the specimen ends. Improved bonding reduces emissions. Yet, regardless of the quality of bonding studied, debonding is not significant until immediately before the bundle failure. That is, debonding is not gradual; rather, it is sudden and catastrophic.

3. KINK BAND FORMATION

3.1 Incipient Failure

The dominant failure modes in composites are sensitive to constituent properties, the quality of fiber-matrix adhesion, defects, and the fiber volume fraction. Therefore, it is difficult to develop a unified model to account for all competing modes of failure. What is feasible, however, is to identify the incipient mode of failure and construct a model to incorporate only those parameters that are responsible for that particular mode of failure. Such a model can still serve as a guide for further improvements in compressive strength.

The results of the preceding section indicate that in composites made with glass, graphite and alumina fibers, the intrinsic compressive strengths of fibers are not fully utilized and hence failure of these fibers in composites is the result of microbuckling or kinking. Even for initially straight fibers the tensile radial stresses at the fiber-matrix interface can be as high as 1 to 3% the applied axial stress [20]. Thus, fiber-matrix debonding is possible even under longitudinal compression if the interface is not strong enough. The reduced support for the fibers due to interfacial failure facilitates microbuckling and will lead to final failure.

In real composites, the fibers usually are not straight. This is why the measured longitudinal compressive moduli are frequently lower than the tensile moduli [19]. Upon compression, the initial curvature certainly helps fibers buckle more easily against the resistance by the matrix through the interface. The matrix resistance depends not only on the matrix properties but also on the type of fiber buckling. That is, if the buckling of the fibers is in-phase, the matrix deformation will be mostly in shear,

while an out-of-phase buckling will induce predominantly normal deformation in the matrix.

In a composite with a fiber volume fraction V_f and a matrix volume fraction V_m , the average composite stress σ_c is related to the average fiber stress σ_f and the average matrix stress σ_m by

$$\sigma_c = V_f \sigma_f + V_m \sigma_m \quad (3)$$

If the fibers are inherently weak in compression, they fail before buckling and trigger the composite failure. The fiber stress is then equal to the fiber strength X_f , and the composite strength X_c will be given by [19, 30]

$$X_c = V_f X_f + V_m \sigma_m^* \quad (4)$$

where σ_m^* is the matrix stress at the time of fiber failure. As was seen in Chapter 2, highly anisotropic fibers such as high-modulus graphite and Kevlar are much weaker in compression than in tension. Consequently, composites made with these fibers fail as a result of the compressive failure of the fibers and the resulting composite strength follows the prediction given by Equation 4.

If fibers are not inherently weak in compression, their only other mode of failure is flexural failure as a result of buckling. If the matrix material is soft, the fibers will be able to push the matrix aside. It has been shown that even in Kevlar composites the mode of failure changes from fiber dominated to matrix dominated when the matrix yield strength drops below 10 MPa [19].

In out-of-phase buckling of initially curved fibers, the stress exerted

on the matrix is predominantly normal. Assuming sinusoidal deformation of the fibers, this stress is related to the average composite stress by [19],

$$\sigma_c = \frac{8R}{d_f} \left(V_f + \frac{V_m E_m}{E_f} \right) \sigma_{mT} \quad (5)$$

where σ_{mT} is the transverse normal stress exerted on the matrix; and R and d_f denote the fiber radius of curvature and the fiber diameter, respectively. The transverse stress σ_{mT} is tensile on the concave side of the fiber and compressive on the convex side. The tensile stresses can cause fiber-matrix debonding and thus facilitate further microbuckling of the fiber. If bonding is strong, however, the compressive stresses may cause yielding or compressive failure of the matrix. This would also facilitate further microbuckling of the fibers.

The in-phase buckling of fibers places the matrix predominantly in shear. Here, the composite stress needed to keep the fibers in the deformed position can be derived as [10]

$$\sigma_c = V_f \frac{\frac{G_{LT}}{\pi f_0}}{1 + \left(\frac{f_0}{\ell} \right) / \gamma_{LT}} \quad (6)$$

where f_0 and ℓ are the amplitude and half wavelength of the initial fiber curvature, respectively, and γ_{LT} and G_{LT} are the composite shear strain and shear modulus, respectively. The composite fails either when the shear stress exceeds the composite shear strength or when the fibers fail in bending.

The foregoing models are all concerned with the incipient failure of composites. Yet, the final failure always shows the formation of a kink

band. Therefore, details on kink band formation are reviewed in the following section.

3.2 Kink Band Formation

Kinking is a phenomenon that seems to be associated with material anisotropy. The materials that show kinking include single crystals of Cd [31], oriented rods of polyethelyne [32], oriented rods of Nylon [33], anisotropic rocks [34], paperboard [35], and wood [36]. In composite materials fiber kinking has become an important compressive mode of failure.

Although the exact details of kink band formation are not clear, it is believed to be triggered by one of the incipient failure mechanisms discussed in the preceding section. In most composites kinking is the result of fiber microbuckling. However, kinking can also be triggered by the compressive failure of fibers when the fibers are weak. Several investigators have attempted to predict the parameters associated with the kink band geometry, Figure 30(a). These parameters include kink orientation angle α , kink band angle β , and kink length δ .

Berg and Salama [37] argued that the kink band must be inclined in order to permit the buckled fibers to undergo both compressive and shear deformation. The reason is that microbuckling along planes which permit shear displacement as buckling proceeds requires smaller compressive stress than does buckling on a plane that does not permit shear displacement (i.e. planes perpendicular to the loading axis). Weaver and Williams [11] also suggested fiber microbuckling as the cause of kinking. They proposed that as the kink band broadens (i.e. δ increases), the kink band boundary rotates from its original transverse position maintaining a constant $\alpha = 2\beta$.

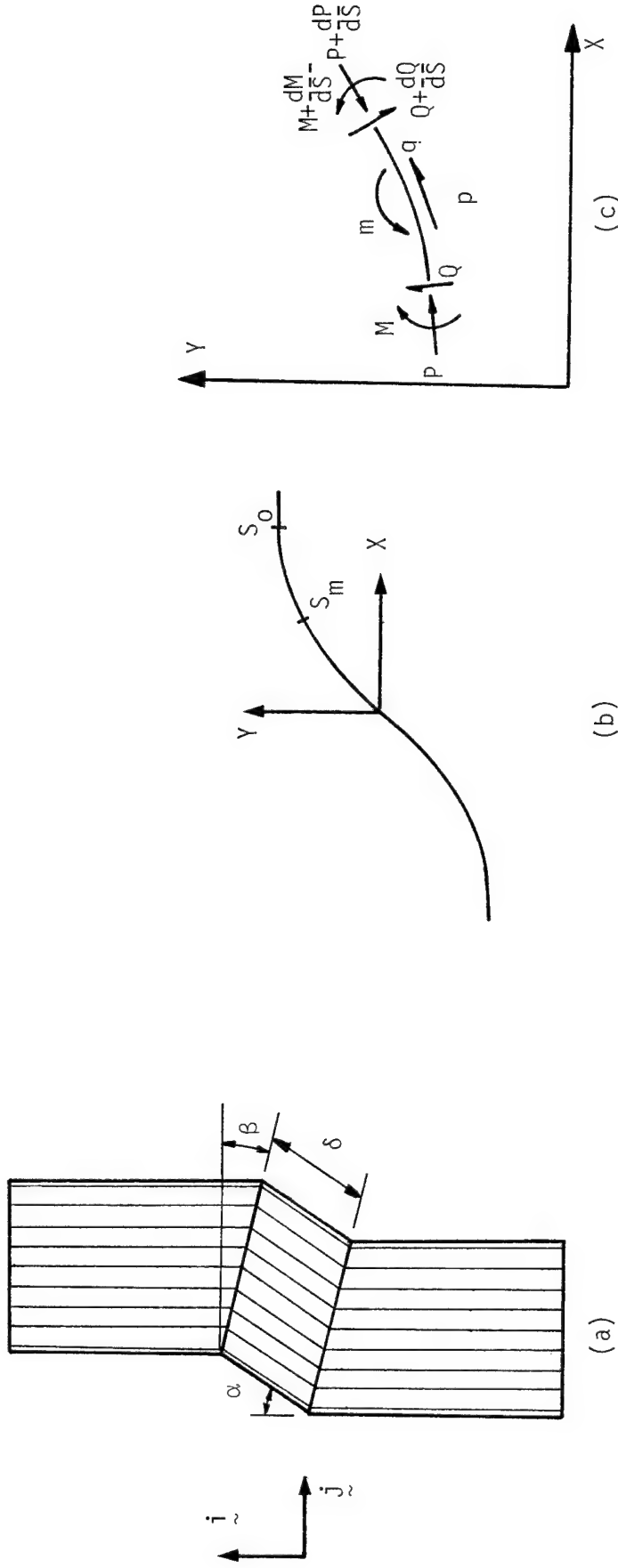


Figure 30. Kink band formation: (a) kink band geometry; (b) a kinked fiber before collapse; (c) free body diagram for an infinitesimal fiber element.

relationship.

By successively sectioning a partially failed glass/epoxy specimen, Chaplin [12] showed that the kink band does not change its orientation during propagation. Once started from a notch or a pre-existing defect, the kink band keeps the same orientation and width. This is compatible with the observations in graphite/epoxy composites in which sequential microbuckling of fibers in the early stage of failure set the kink band angle [10].

A typical kink band angle β is between 20–30 degrees although in some composites extensive longitudinal splitting prevents its accurate measurement [10]. The kink orientation α after failure depends on how early the test is stopped after kinking. Some experimental data suggest a $\alpha = 2\beta$ relationship which can be derived from the condition of zero volumetric strain within the kink band. Evans and Adler [14] used a similar approach and derived this $\alpha = 2\beta$ relationship by minimizing the strain energy within the kink band. They also found a value for the kink orientation angle between 48 to 67 degrees by minimizing the plastic work done on the matrix during fiber rotation. The above predictions are within the range of experimental values.

With the foregoing experimental evidences available to draw upon, we now proceed to develop a model to predict the kink band geometry. The kink band shown in Figure 30(a) is an idealized one just before collapse. In reality, no sharp curvature of fibers is allowed along the kink boundaries, although the kink band after final failure looks like the one in Figure 30(a). The deformation within the kink band can now be described by a deformation tensor E ,

$$\tilde{F} = \begin{bmatrix} F_{11} & F_{12} & 0 \\ F_{21} & F_{22} & 0 \\ 0 & 0 & 1 \end{bmatrix} \quad (7)$$

The deformation tensor \tilde{F} must satisfy the conditions that the kink band boundary does not deform and that the deformation of fiber segments is a simple rotation through angle α . Consequently, the components F_{ij} are related to the angles by

$$F_{11} = \cos\alpha$$

$$F_{12} = (\cos\alpha - 1) \tan\beta$$

$$F_{21} = \sin\alpha$$

$$F_{22} = 1 + \sin\alpha \tan\beta$$

Now, consider two unit vectors v and w before kinking such that

$$\tilde{v} = \tilde{i} \quad \text{and} \quad \tilde{w} = \tilde{j} \quad (9)$$

After kinking, those two vectors deform to

$$\tilde{v}_k = F_{11}\tilde{i} + F_{21}\tilde{j}, \quad \tilde{w}_k = F_{12}\tilde{i} + F_{22}\tilde{j} \quad (10)$$

Therefore, the change in area defined by v and w , ΔA , after kinking becomes

$$\Delta A = \frac{\cos(\alpha - \beta)}{\cos\beta} - 1 \quad (11)$$

Furthermore, the shear strain

$$\gamma_{LT} = \sin\alpha + (1 - \cos\alpha) \tan\beta \quad (12)$$

The condition that there be no volumetric change in kinking requires that [12,14]

$$\alpha = 2\beta \quad (13)$$

Although there are some experimental data indicating the validity of the relationship given by Equation (13), it should be noted that the kink orientation α depends on the amount of deformation allowed after kinking. If loading is permitted to increase even after kinking failure, α will certainly increase although β does not change any more. Therefore, α must be taken as the kink orientation just before final collapse. With this new definition for α , Equation (13) does not hold true, as will be shown later.

Micrographic evidences suggest that kink bands form in three steps: elastic kinking, plastic kinking, and then final collapse as a result of fiber failure at the kink boundaries. In the plastic kinking stage, the matrix within the kink band yields in shear.

For a kinked fiber shown in Figure 30(b), the local equilibrium equations are given by (See Figure 30 (c)).

$$q + dQ/ds + P (d\omega/ds) = 0 \quad (14)$$

$$p - dP/ds + Q (d\omega/ds) = 0 \quad (15)$$

$$dM/ds - Q + m = 0 \quad (16)$$

The symbols in Equations (14)-(16) are defined as follows:

ω = slope of the deflected fiber axis,

P = axial compressive force,

Q = transverse shear,

M = bending moment,

p = applied distributed axial force,

q = applied distributed transverse force,

m = applied distributed bending moment

s = distance along the fiber from the coordinate origin.

As a first order approximation, we assume that the axial force P

remains constant and disregard Equation (15). Furthermore, for the kinking deformation under consideration, it is plausible to set $q = 0$. Since the solution of Equation (14) is given by $Q = -P\omega$, Equation (16) becomes

$$\frac{dM}{ds} + P\omega + m = 0 \quad (17)$$

The internal bending moment in the fiber is obtained from

$$M = E_f I_f \frac{d\omega}{ds} \quad (18)$$

where I_f is the moment of inertia for the fiber cross section. Since the kink band is in a state of plastic yielding, the average shear stress is equal to the laminate yield stress τ_y . The corresponding distributed moment m is then [10]

$$m = -A_f \tau_y \quad (19)$$

where A_f is the fiber cross-sectional area.

Substitution of Equations (18) and (19) into Equation (17) finally yields an equation for ω ,

$$\frac{d^2\omega}{ds^2} + \frac{P}{E_f I_f} \omega = \frac{A_f \tau_y}{E_f I_f} \quad (20)$$

The appropriate boundary conditions for the kinked fiber shown in Figure 30 (b) are

$$\frac{d\omega}{ds} = 0 \text{ at } s = 0 ; \omega = \frac{d\omega}{ds} = 0 \text{ at } s \geq s_0 \quad (21)$$

The solution to Equation (20) is thus

$$\omega = \frac{A_f}{P} \tau_y (1 + \cos \sqrt{\frac{P}{E_f I_f}} s) \quad (22)$$

$$s_0 = \pi \sqrt{\frac{E_f I_f}{P}} \quad (23)$$

The fiber will break where the curvature is maximum. The maximum fiber curvature is obtained from Equation (22) as

$$\left(\frac{d\omega}{ds}\right)_{\max} = \frac{d\omega}{ds} \Big|_{s=s_m} = 4 \frac{\tau_y d_f}{\sqrt{\sigma_f E_f}} \quad (24)$$

where

$$s_m = \frac{s_0}{2} \quad (25)$$

and $P = A_f \sigma_f$ has been used. The resulting maximum strains in the fiber are given by

$$\varepsilon_b^{(+)} = \frac{d_f}{2} \left(\frac{d\omega}{ds}\right)_{\max} - \frac{\sigma_f}{E_f} = 2 \frac{\tau_y}{\sqrt{\sigma_f E_f}} - \frac{\sigma_f}{E_f} = \text{tensile} \quad (26)$$

$$\varepsilon_b^{(-)} = 2 \frac{\tau_y}{\sqrt{\sigma_f E_f}} + \frac{\sigma_f}{E_f} = \text{Compressive} \quad (27)$$

If fiber failure is initiated on the tension side, the applied fiber stress σ_f^* is obtained from

$$\varepsilon_f^{(+)} = 2 \frac{\tau_y}{\sqrt{\sigma_f^* E_f}} - \frac{\sigma_f^*}{E_f} \quad (28)$$

On the other hand, the fiber stress for the compression-initiated fiber failure is obtained from

$$\varepsilon_f^{(-)} = 2 \frac{\tau_y}{\sqrt{\sigma_f^* E_f}} + \frac{\sigma_f^*}{E_f} \quad (29)$$

In equations (28) and (29), $\varepsilon_f^{(+)}$ and $\varepsilon_f^{(-)}$ are the tensile and compressive failure strains, respectively, of the fiber.

The kink orientation is equal to the maximum slope at the time of fiber failure, and therefore is given by

$$\alpha = \frac{W_{\max}}{\sigma_f} \Big|_{\sigma_f} = \sigma_f^* = 2 \frac{\tau_y}{\sigma_f^*} \quad (30)$$

Also, the kink length δ is equal to

$$\delta = 2S_m \Big|_{\sigma_f} = \sigma_f^* = \frac{\pi}{4} d_f \sqrt{\frac{E_f}{\sigma_f^*}} \quad (31)$$

With α known, we now turn to the determination of β . Since the matrix was assumed to have yielded, the average shear stress in the kink band is τ_y . The shear strain depends on the kink band angle β as indicated by Equation (12). Therefore, instead of Equation (13), assume that the angle β is determined so that the shear strain γ_{LT} reaches the failure strain in shear γ_y at the time of final collapse. The result is then

$$\beta = \tan^{-1} \frac{\gamma_y - \sin \alpha}{1 - \cos \alpha} \quad (32)$$

The foregoing equations predict all the pertinent parameters for kink bands. The compressive strength X_c is determined from Equation (3) by substituting σ_f^* in place of σ_f . σ_f^* is in turn determined from Equation (28) or (29), depending on which yields a lower value. The kink orientation α and the kink length δ are given by Equations (30) and (31), respectively. Finally, the kink band angle β follows from Equation (32). The results obtained here are similar to those given by Budiansky [38].

3.3 Experimental Observations

Eleven different unidirectional composites were used to study the kink band formation. These eleven consisted of seven graphite/epoxy composites, two graphite/thermoplastic composites, one glass/epoxy composite, and one Kevlar /epoxy composite. All specimens were cut to fit an IITRI compression fixture and were tested on an Instron testing machine at a crosshead speed of 1 mm/min. Experimental details and compressive properties for the graphite/epoxy composites are reported in References [10,39]. The detailed data for the glass/epoxy and the Kevlar/epoxy composites can be found in References [40] and [41], respectively. Table 5 lists the average mechanical properties of different material systems. As was discussed earlier, kinking is believed to be due to microbuckling of the fibers in most composites. The following evidence supports this conclusion.

Figure 31 shows a T300/BP907 at the onset of failure at two different magnifications. Microbuckling of the fibers can be seen clearly. Each fiber has fractured at several points. Fiber fracture seems to have been initiated at points of maximum fiber curvature. Figure 31(a) shows that sequential microbuckling of fibers has taken place along a band making an angle of about 18° to the horizontal. This is within the reported range of $16\text{--}30^{\circ}$ that is common for graphite/epoxy composites. As expected, microbuckling was initiated at the edge and propagated inward; fibers ahead of the failure band are still straight and intact. Figure 32 shows another T300/BP907 specimen after final failure. The primary and conjugate kinks are orientated about 24° to horizontal. Fiber segments of regular periodicity are shown within the top kink band. Multiple fiber fractures were probably caused by propagation of the buckling wave [11]. Average

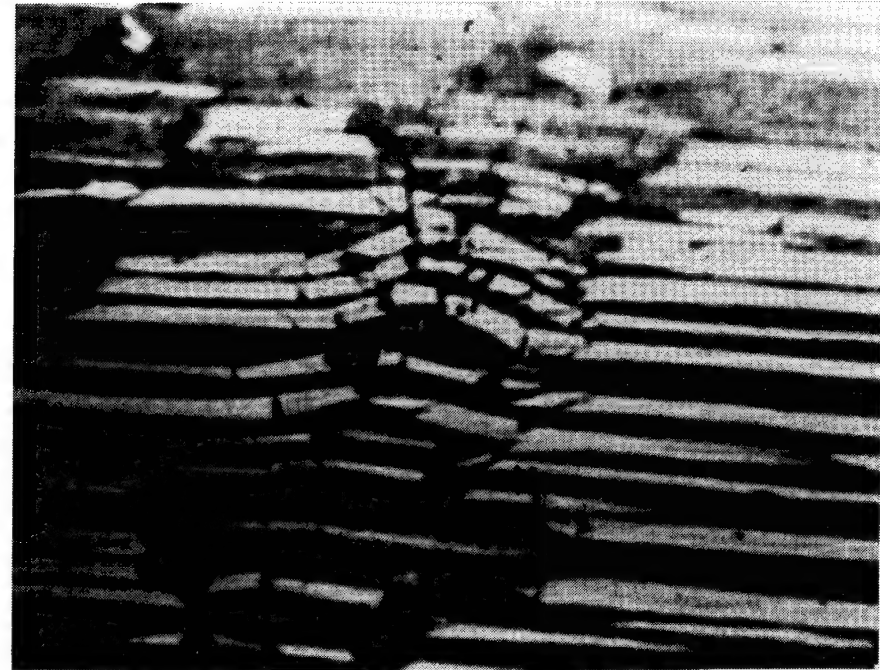
Table 5. Mechanical Properties of Different Unidirectional Composites.

Material	Modulus (GPa)	Strength (MPa)	Failure strain (%)
Graphite/epoxy			
T300/5208	128.1	1183	1.25
T300/BP907	118.7	762	0.54
T300/4901/MDA	147.9	1412	1.01
T300/4901/mPDA	152.4	1394	1.00
T700/BP907	126.4	915	1.20
T700/4901/MDA	143.5	1176	0.81
T700/4901/mPDA	134.8	1189	1.14
Graphite/ thermoplastic resin			
T300/PEEK	140.6	1211	1.03
T300/PPS	131.3	980	0.78
Kevlar/epoxy			
RT ¹	64.6	228	0.36
RTP ²	76.6	240	0.39
ETP ³	--	179	--
S2-g1/epoxy			
RT	56.4	705	--
ETP	55.6	669	--

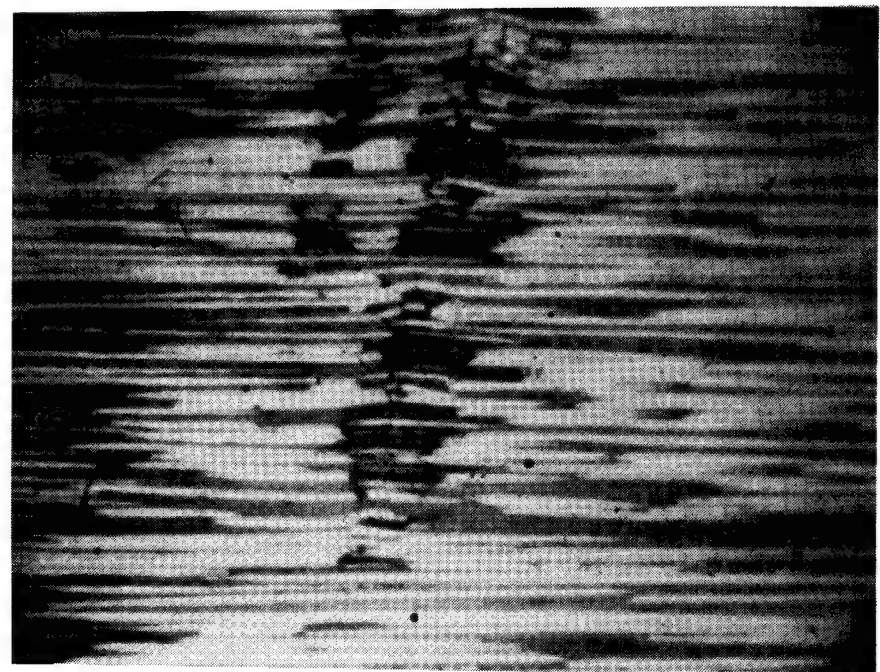
1 Room temperature

2 Room temperature, preconditioned

3 Elevated temperature, preconditioned



(a)



(b)

Figure 31. Failure initiation in a T300/BPP907 specimen (a) 200 X, (b) 500 X.

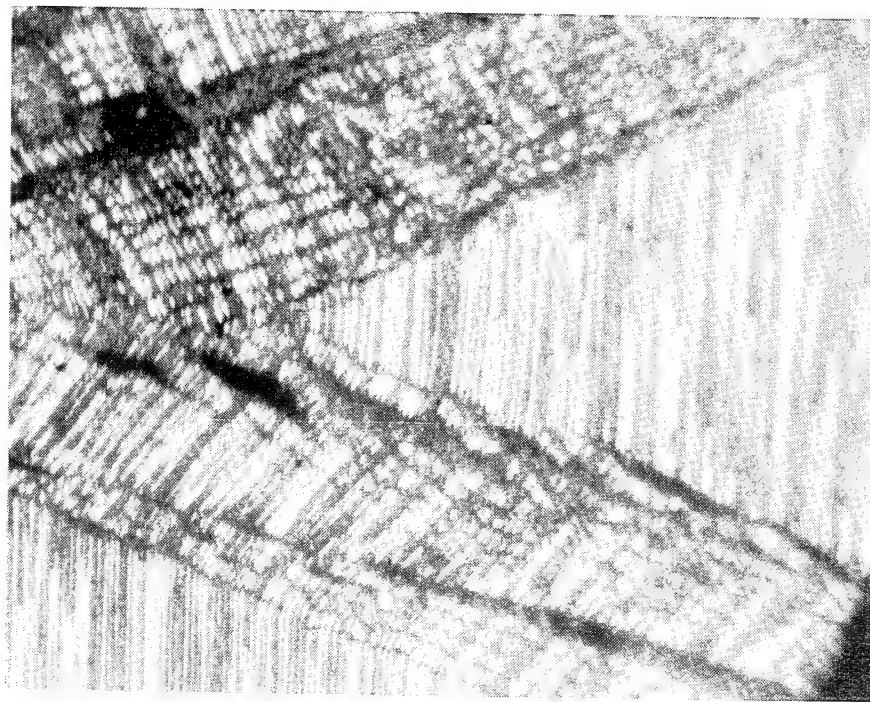
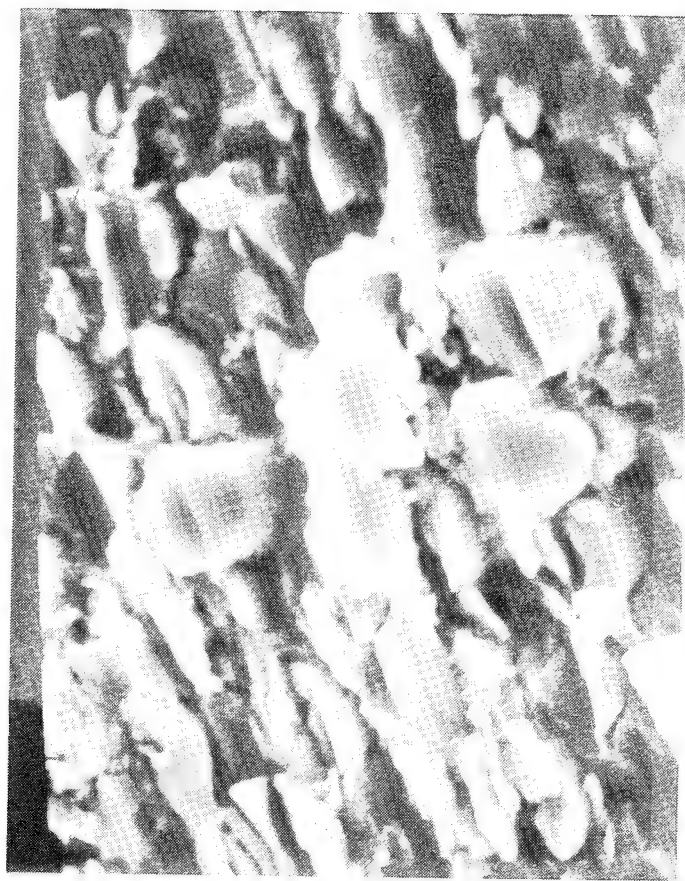


Figure 32. Primary and conjugate kink bands
in a T300/BP907 specimen (100 X).

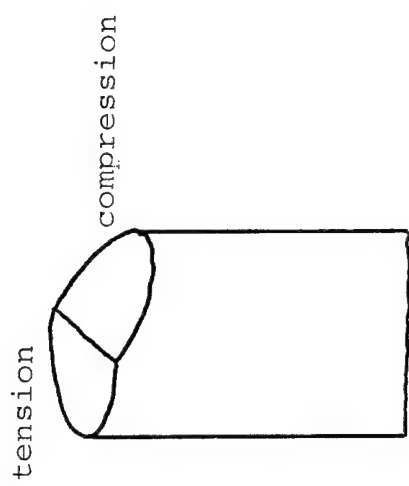
segment length of fractured fibers in Figure 31(b) is between 2-4 times the fiber diameter. This is close to the segment lengths observed within the kink zone in Figure 32.

A SEM micrograph of the fracture surface of a T300/5208 specimen is shown in Figure 33(a). This surface is parallel to the plane of the kink band. The fiber fracture surfaces show two distinct zones separated by a straight boundary. Since graphite fibers are brittle, their fracture surface in bending consists of two regions, Figure 33 (b). The inclined region is on the compression side and the horizontal region is on the tension side. The lines seen on the fiber fracture surfaces in Figure 33 (a) would then suggest a bending mode of failure like microbuckling for each fiber. The boudary lines on different fiber fracture surfaces are more or less parallel to one another indicating that the fibers buckled in phase with one another. A similar phenomenon can be seen in Figure 34 for a T300/4901/mPDA specimen, and in Figure 35 for a T300/PPS specimen. Tilted fiber segments on the left and center of Figure 34 show the direction of relative motion across the kink band. Fiber segments shown in this figure are about 3 times the fiber diameter.

Once microbuckling has occurred and propogated through the specimen width or thickness, the top portion over the microbuckling zone slips relative to the bottom portion. In the slipping process the buckled fibers rotate as the matrix deforms plastically and forms a kink band. If the slip is not contained by hydrostatic pressure or some kind of lateral support, the fiber segments within the kink band fall apart and the kink structure is destroyed. The remains of the structure can often be seen as tilted fibers on the fracture surface. These fibers are tilted in the direction compatible



(a)



(b)

Figure 33. (a) Fiber fracture surfaces in a T300/5208 specimen (1000 X),
(b) Bending Failure of a brittle fiber.

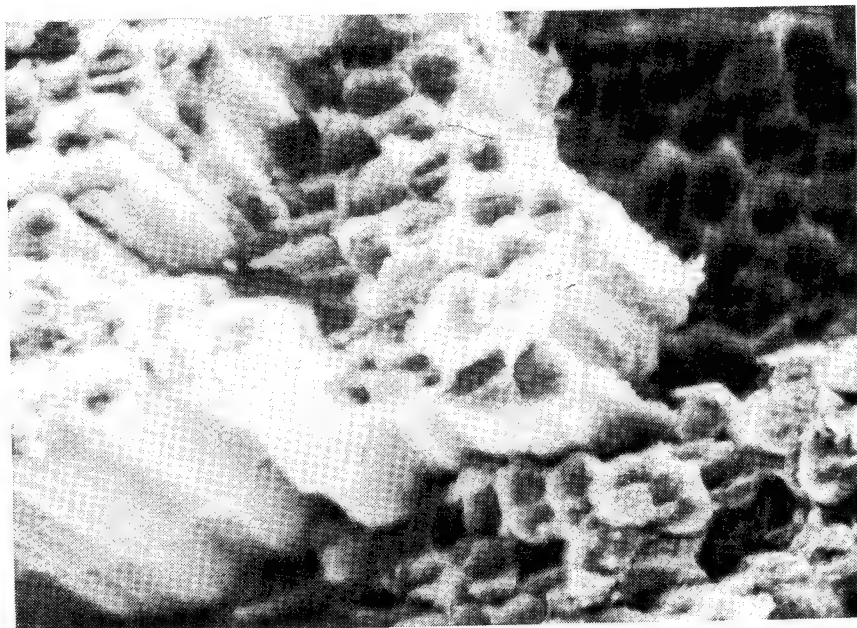


Figure 34. Fiber fracture surfaces in a T300/mPDA specimen (1000 X).

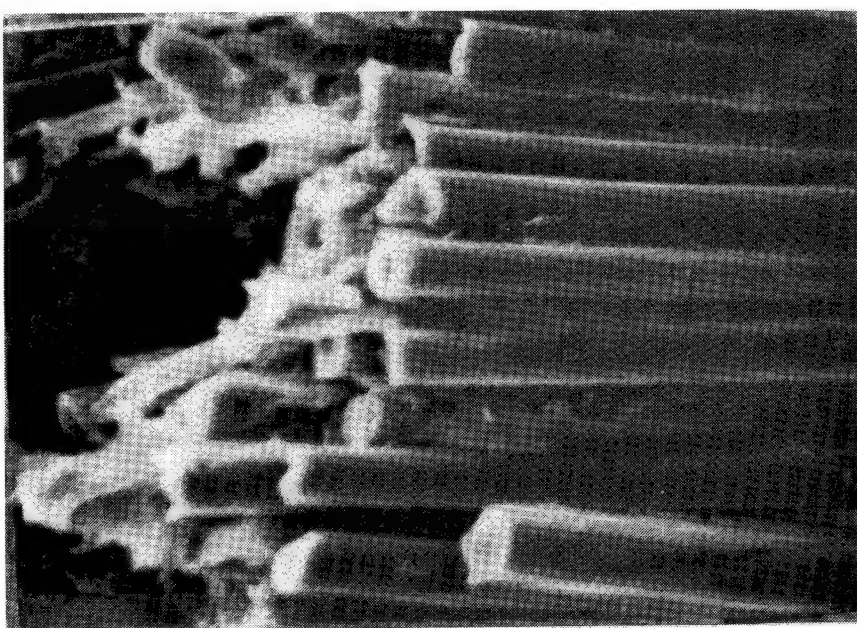


Figure 35. Fiber fracture surfaces in a T300/PPS specimen (900 X).

with the overall slip and plastic deformation of the matrix within the kink band.

Figures 36 through 44 show typical macroscopic features of failure in different graphite/epoxy specimens tested. In general, T300/5208 show the most longitudinal splitting, whereas the composites made with BP907, PPS, or PEEK resin show very little splitting after failure. The composites made with 4901/MDA or 4901/mPDA resin lie somewhere between the two extremes in their resistance to longitudinal splitting.

Figures 45 through 54 show SEM micrographs of fracture surfaces of different material systems under compression. Each figure is accompanied by a small sketch that shows the overall fracture surface and the direction from which the specimen was viewed. Comparing the fracture surfaces of T300 composites with those of T700 composites reveals a cleaner fiber-matrix separation in the latter composites. This would suggest a stronger interface in T300/epoxy composites than in T700/epoxy composites. This may explain why the T300/epoxy composites are stronger than the corresponding T700/epoxy composites. It should be kept in mind, however, that the smaller diameter of T700 graphite fiber may also lead to a lower compressive strength for the composite. Debonded fibers in T300/PPS display cleaner surfaces than those in T300/PEEK, indicating a stronger interface in the latter. Again, this may partially account for the higher compressive strength of T300/PEEK compared with T300/PPS.

Although all the composites considered failed by kinking, different morphologies could be identified for different material systems. In Kevlar/epoxy and glass/epoxy specimens the kink band was invariably formed through the thickness. In graphite composites, however, the kink band was

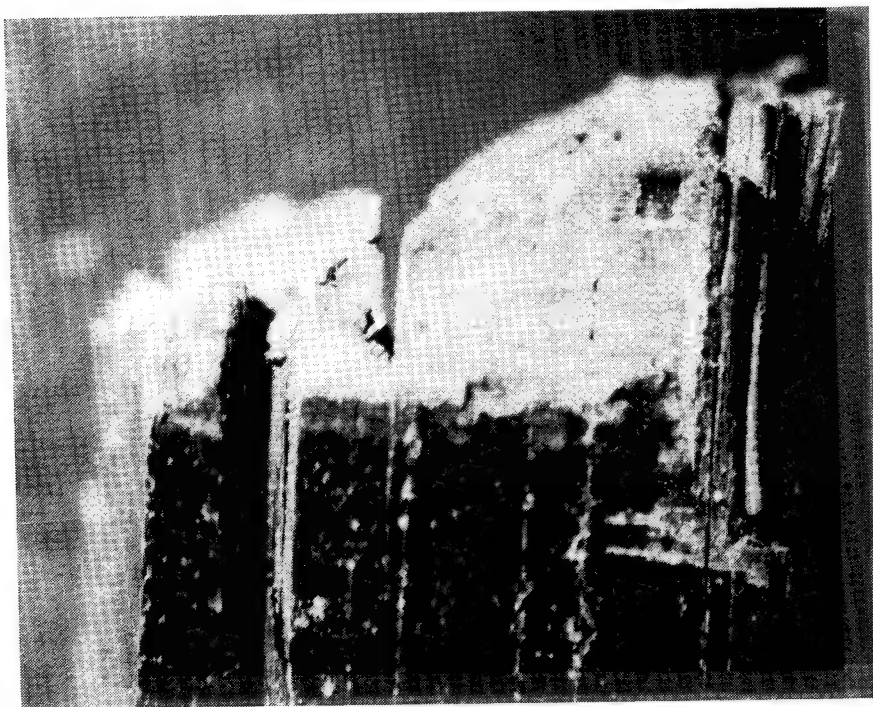


Figure 36. Failure through the width of a T300/5208 specimen (12 X).

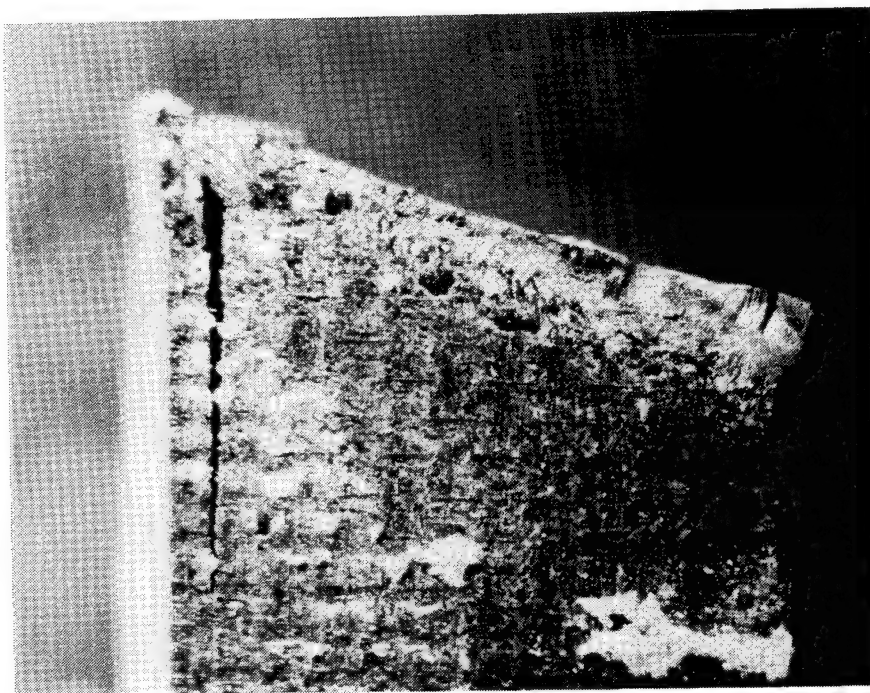


Figure 37. Failure through the width of a T300/BP907 specimen (12 X).

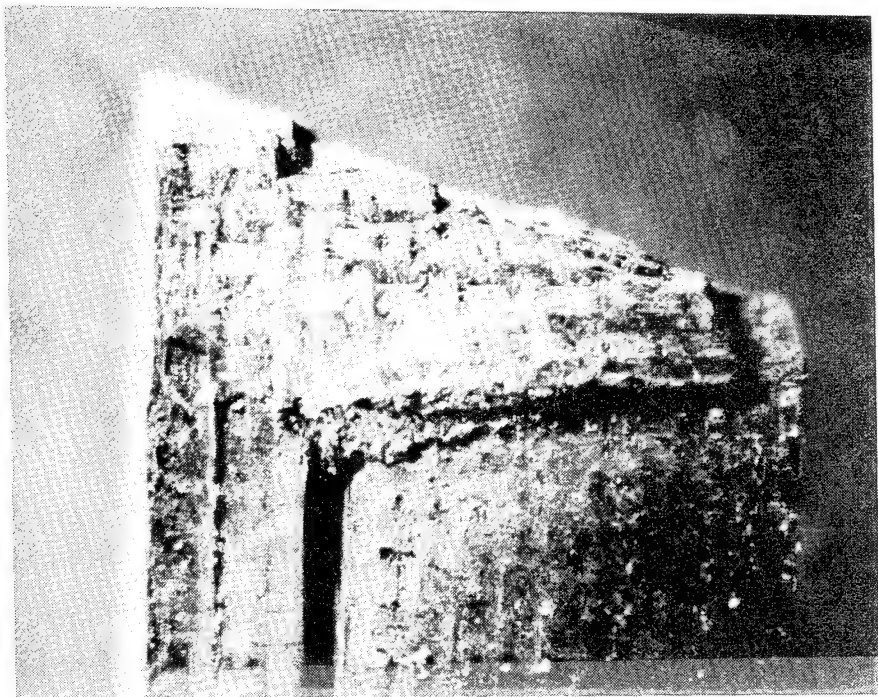


Figure 38. Failure through the width of a T300/4901/MDA specimen (12 X).

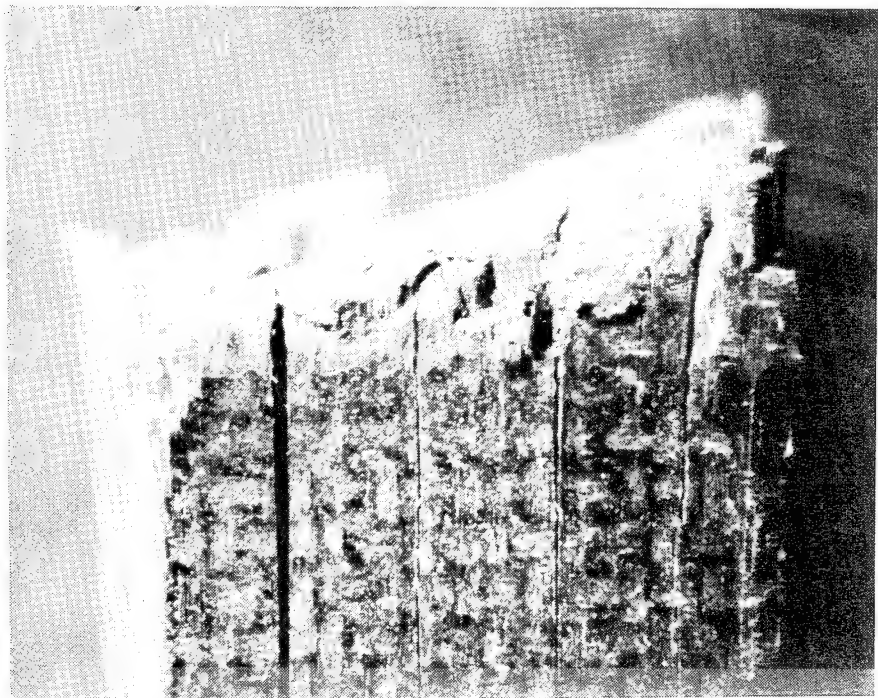


Figure 39. Failure through the width of a T300/4901/mPDA specimen (12 X).

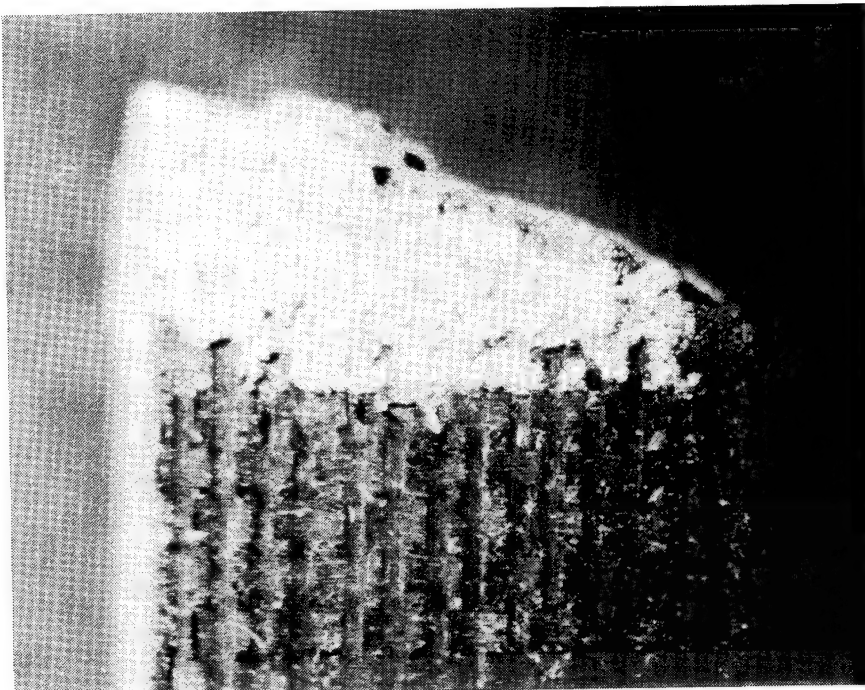


Figure 40. Failure through the width of a T700/BP907 specimen (12 X).

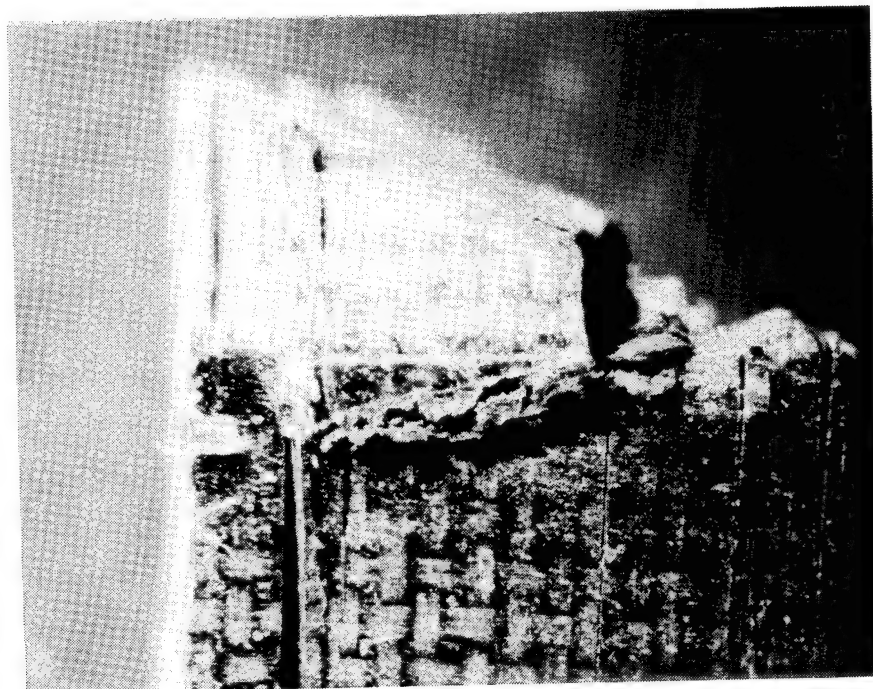


Figure 41. Failure through the width of a T700/4901/MDA specimen (12 X).

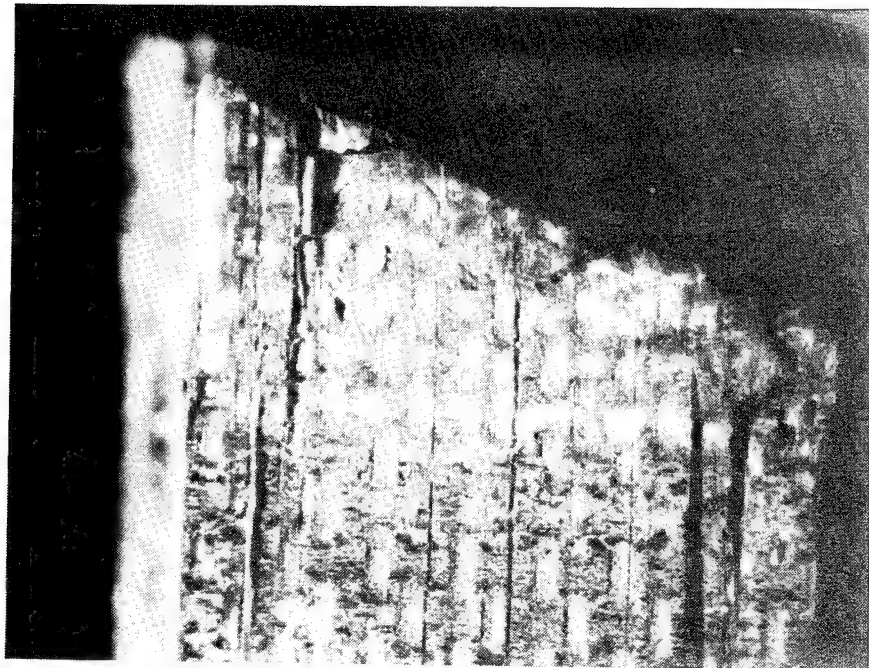


Figure 42. Failure through the width of a
T300/PPS specimen (12 X).

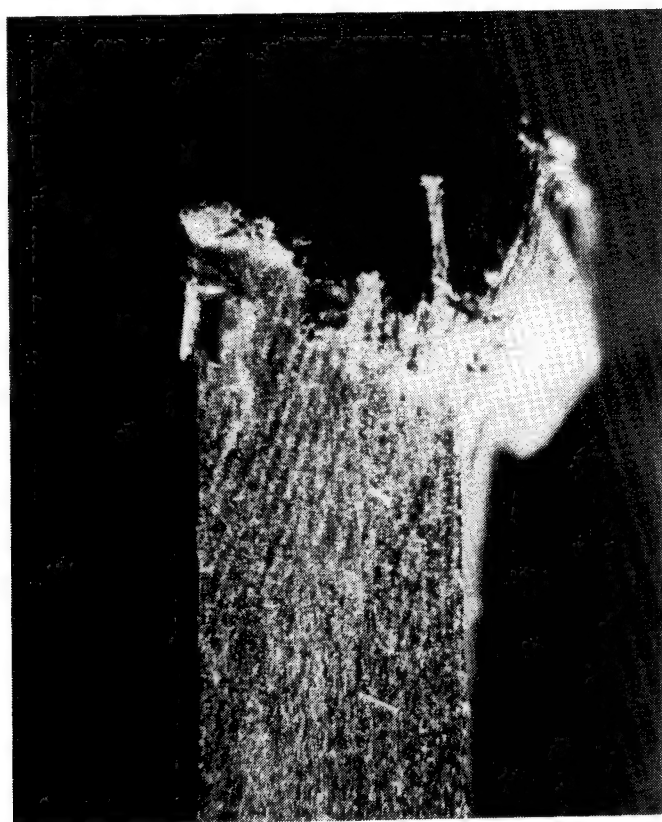


Figure 43. Failure through the thickness of a T300/PPS specimen (12 X).

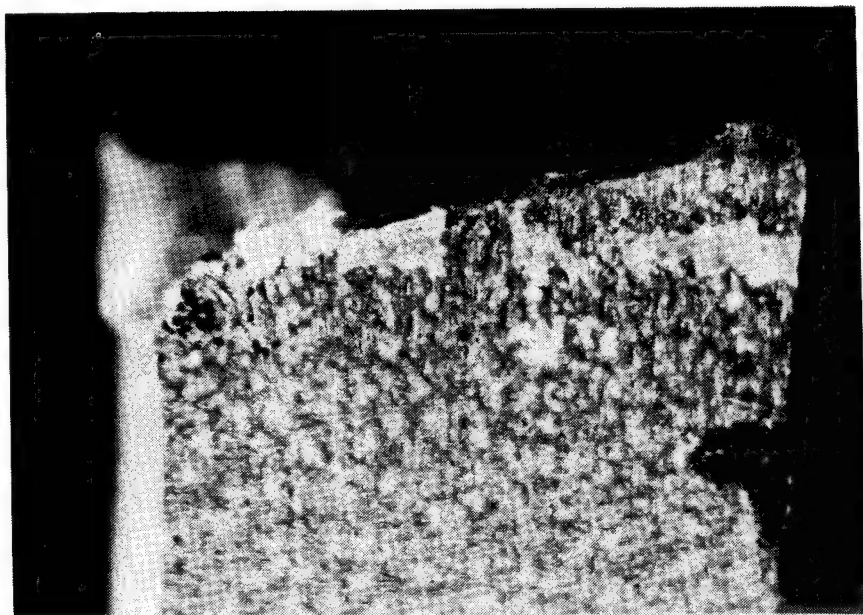


Figure 44. Failure through the width of a T300/PEEK specimen (12 X).

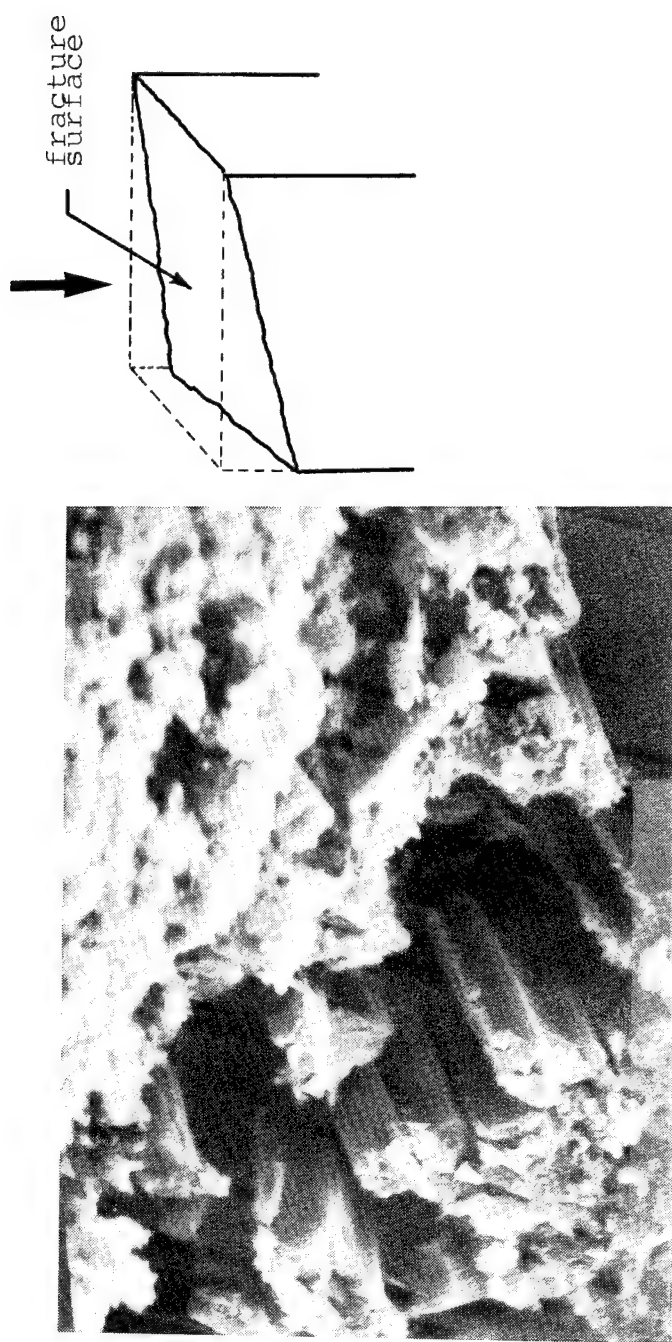


Figure 45. SEM micrograph of the fracture surface of a T300/5208 specimen (1250 X).

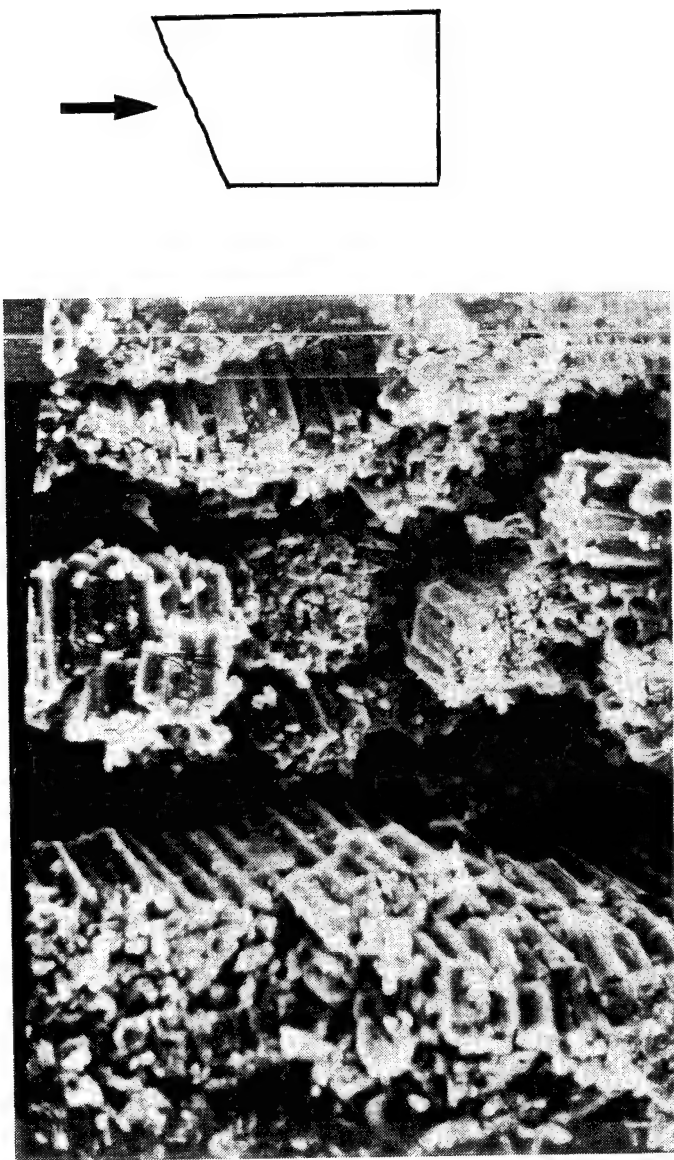


Figure 46. SEM micrograph of the fracture surface of a T300/
BP907 specimen (500 X).

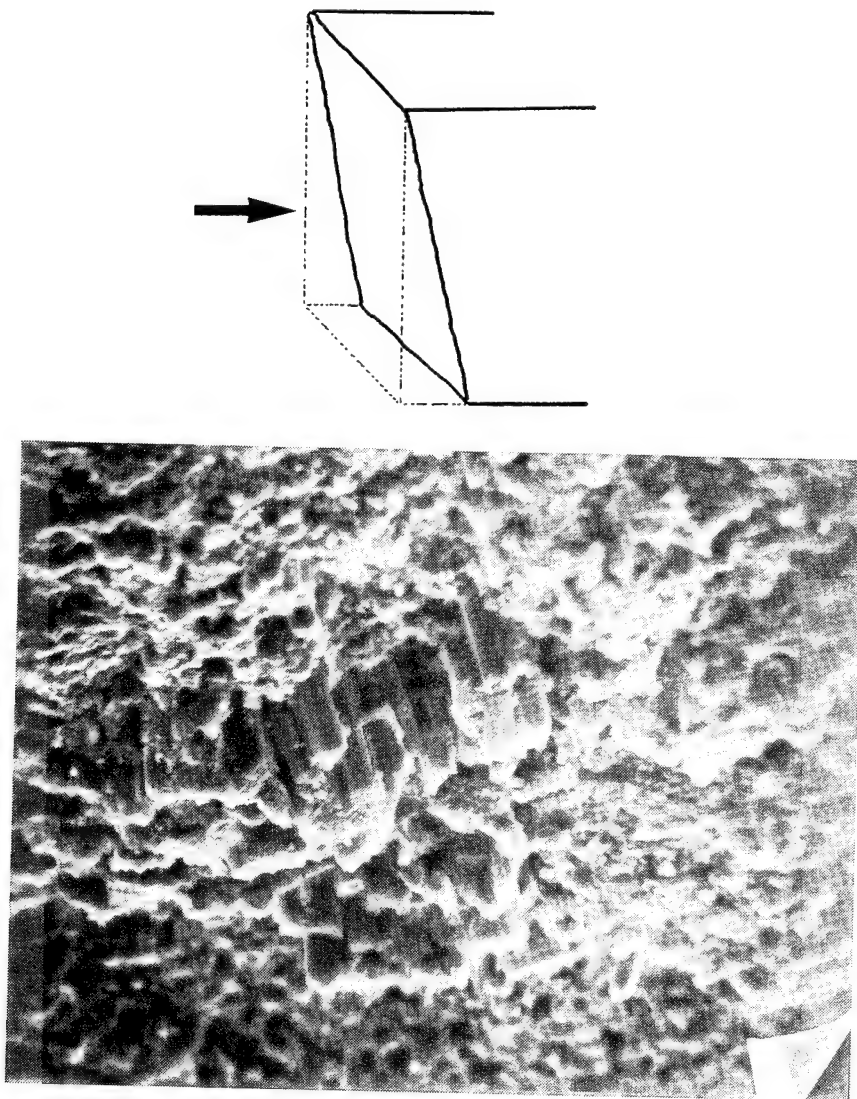


Figure 47. SEM micrograph of the fracture surface of a T300/4901/MDA specimen (500 X).

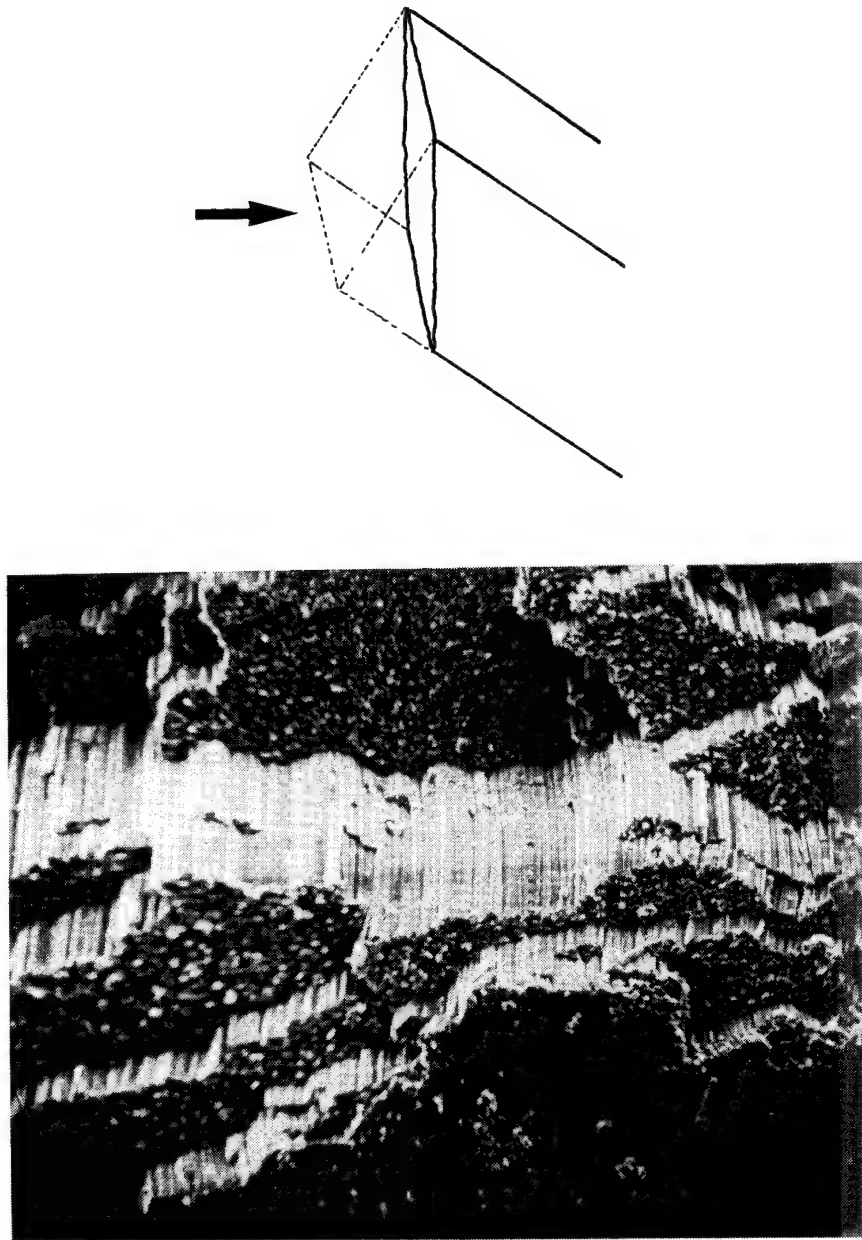
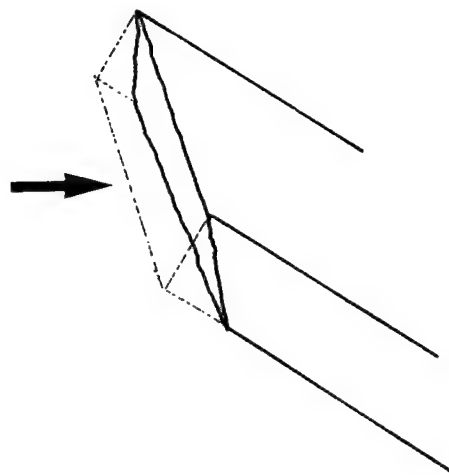
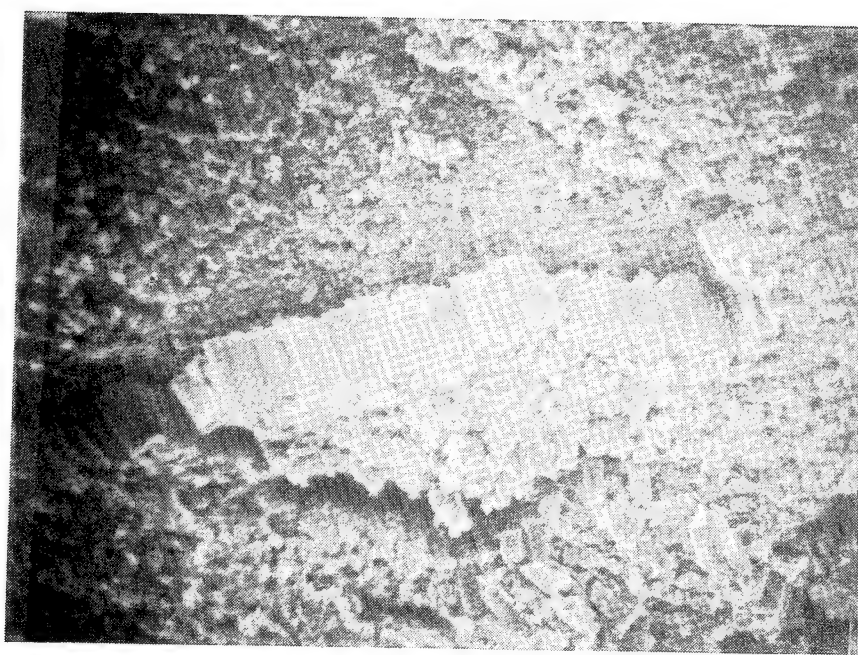


Figure 48. SEM micrograph of the fracture surface of a T300/4901/mPDA specimen (100 X).

Figure 49. SEM micrograph of the fracture surface of a T700/
BP907 specimen (400 X).



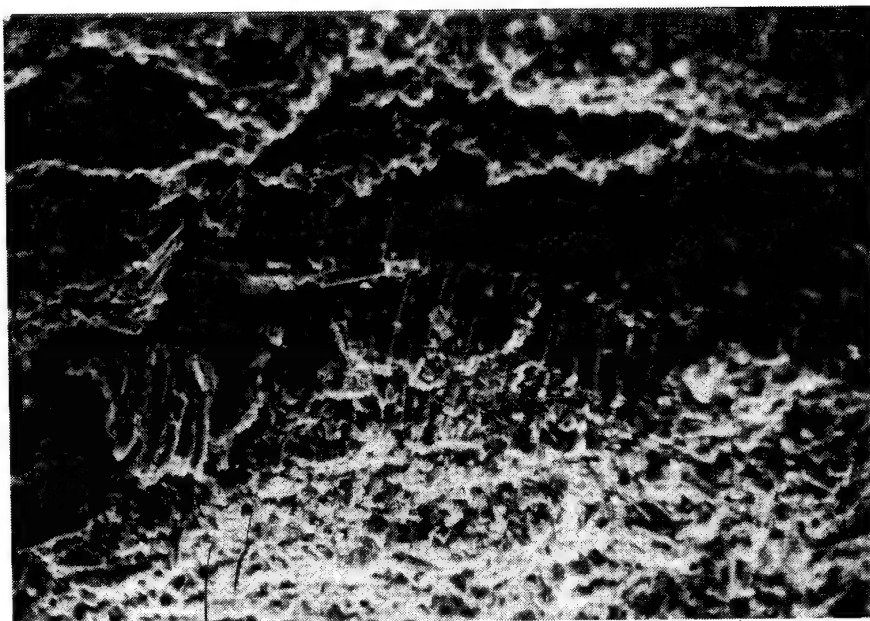
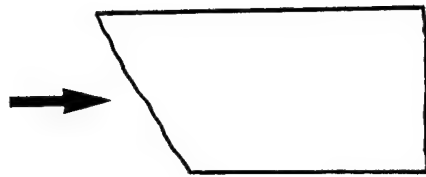


Figure 50. SEM micrograph of the fracture surface of a T700/4901/MDA specimen (250 X).

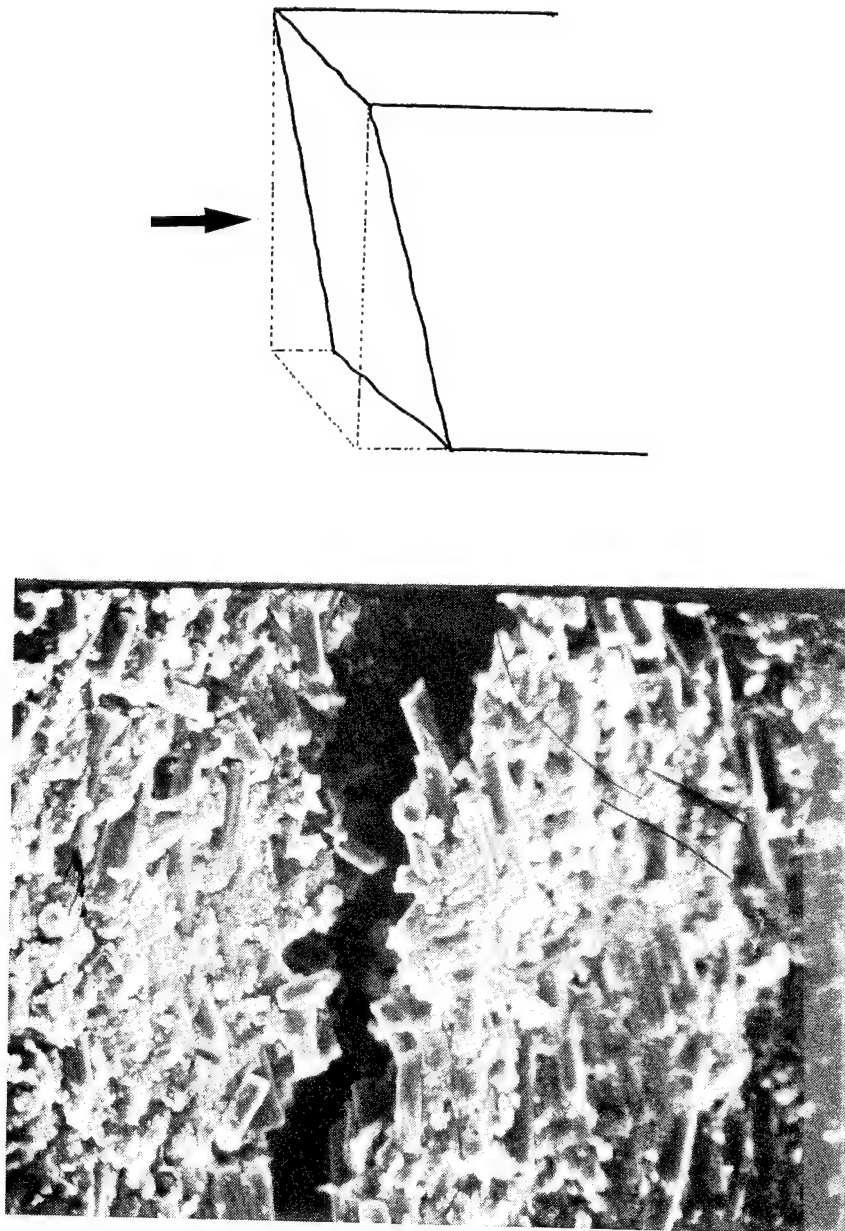


Figure 51. SEM micrograph of the fracture surface of a T700/4901/mPDA specimen (500 X).



Figure 52. SEM micrograph of the fracture surface of a T300/PPS specimen (125 X).

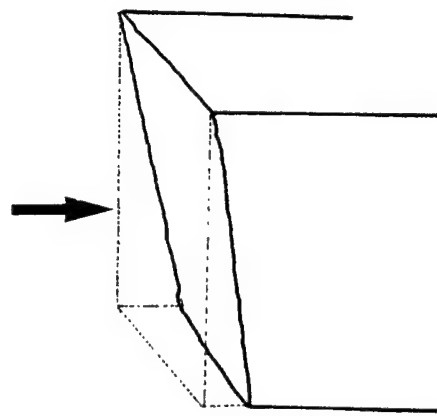


Figure 53. SEM micrograph of the fracture surface of a T300/PEEK specimen (1300 X).

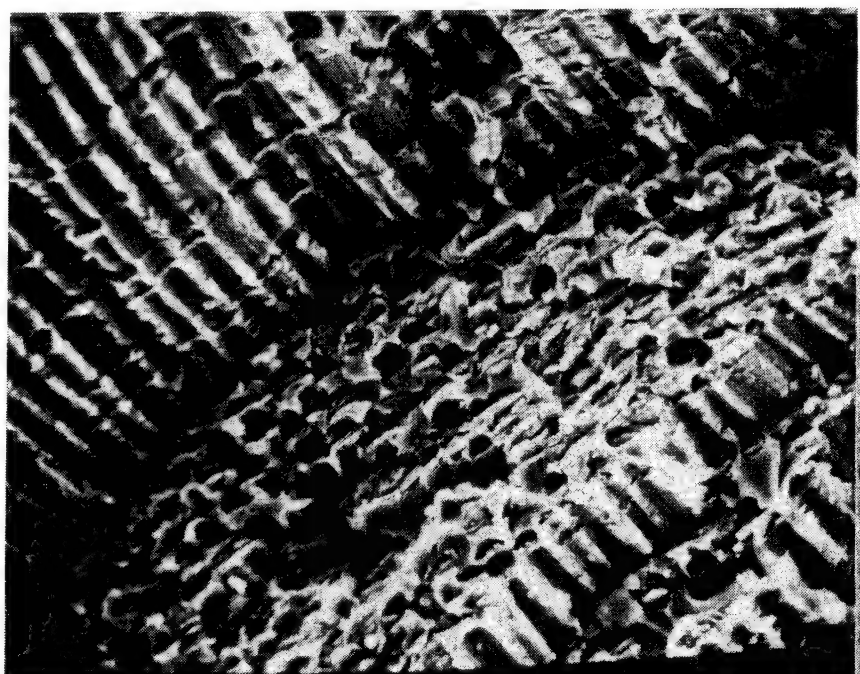
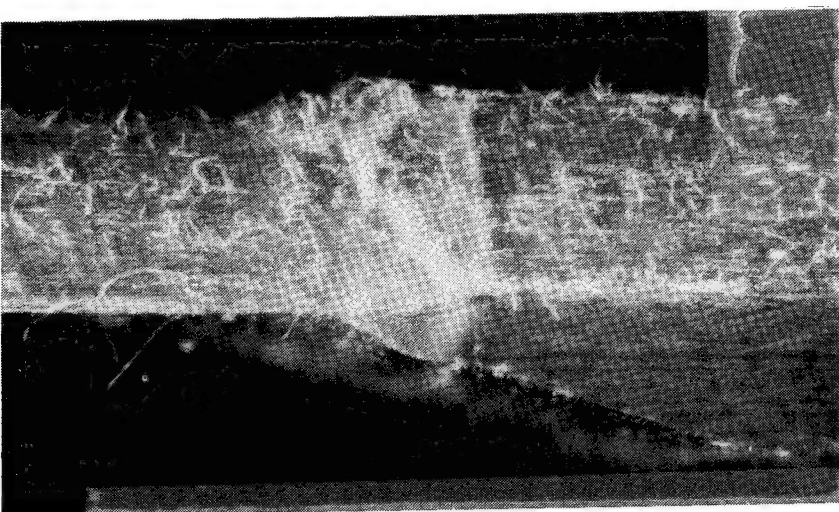


Figure 54. SEM micrograph of a T300/BP907 specimen showing fiber-matrix separation (500 X).

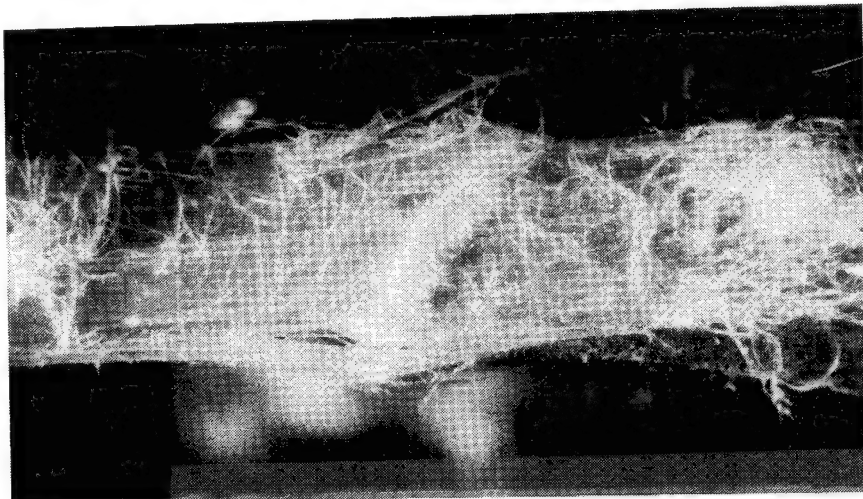
observed either through the thickness or through the width depending on the particular specimen. Kulkarni, et al [13] noticed that, if unidirectional Kevlar specimens were restrained transversely by glass fabrics, compressive strength increased and the kink band appeared through the thickness rather than through the width. The graphite/epoxy composites, however, did not associate higher strength with any of the above two modes.

The kink band in the graphite composites is characterized by well defined boundaries and multiply fractured fibers. The boundary is formed by fiber fractures. Some fracture surfaces show fiber-matrix debonding, Figure 54; imprints of the debonded fibers can be seen on the matrix. Multiple fracture of graphite fibers within the kink band may be due to their brittle nature and lower strain capability.

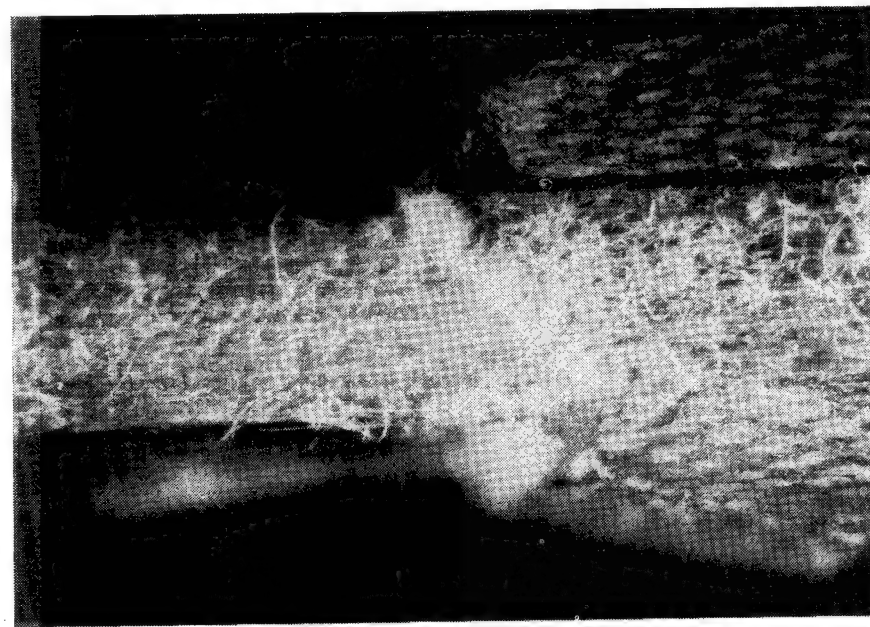
Figure 55 shows a Kevlar specimen tested at room temperature, the failure of a preconditioned Kevlar specimen tested at room temperature and another tested at 75°C. Preconditioning was done at 75°C in vacuum. There is no fiber fracture at the boundary although the fibers are sharply bent. Instead, fibers are kinked at the boundaries, Figures 56 (a) and (b). In spite of the softening of the resin at the elevated temperature, neither the failure mode nor the strength changes because the composite failure is the result of the compressive failure of fibers. There is no sign of damage on the fibers within or without the kink band, some distances away from the kink band boundaries, Figures 57 and 58, respectively. This is in contrast to the failure mode observed for Kevlar fibers themselves under compression [23]. A Kevlar fiber, when tested by itself, shows kinking uniformly distributed along its length. According to Detersa et al. [23], Kevlar fibers can unfold after kinking if they are stretched again. Also, it is



(c)

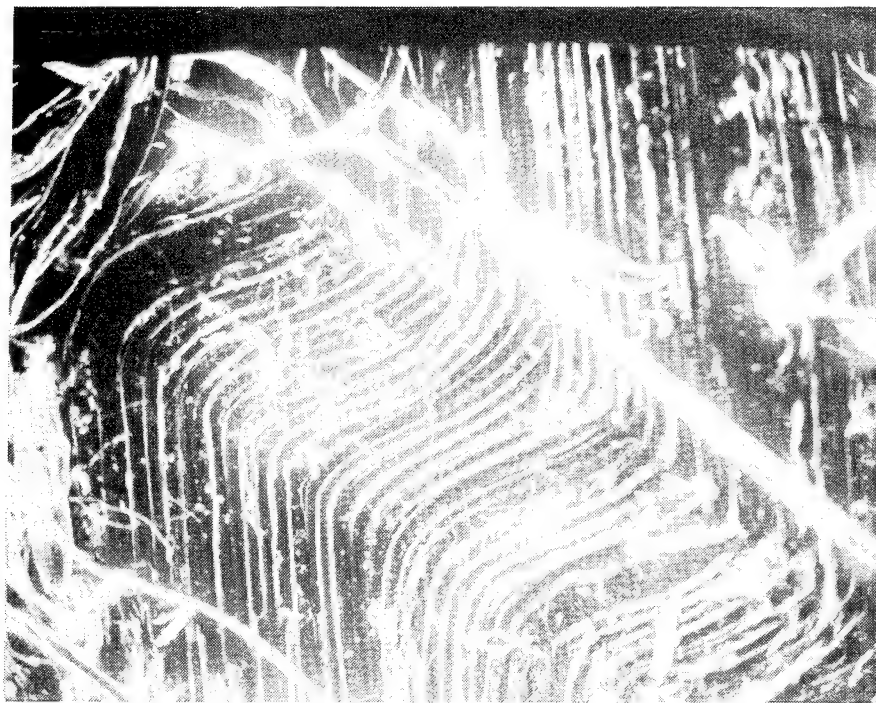


(b)

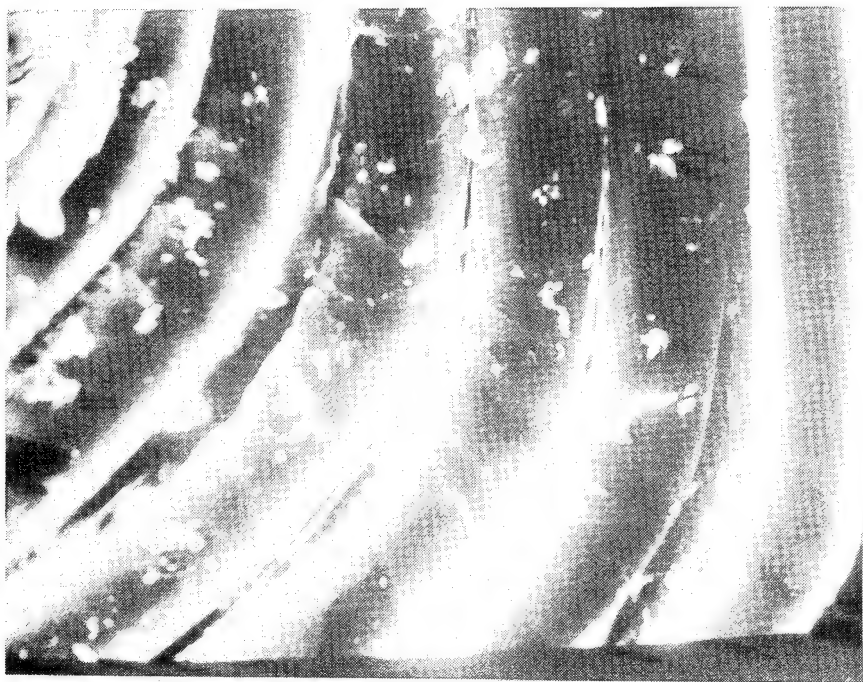


(a)

Figure 55. Kinking failure in Kevlar/epoxy specimens: (a) tested at room temperature (12 X); (b) preconditioned and tested at room temperature (12 X); (c) preconditioned and tested at 75°C (12 X).



(a)



(b)

Figure 56. Typical kinking failure in Kevlar specimens (a) overall view (150 X); (b) failure of fibers at the kink-band boundary (1300 X).

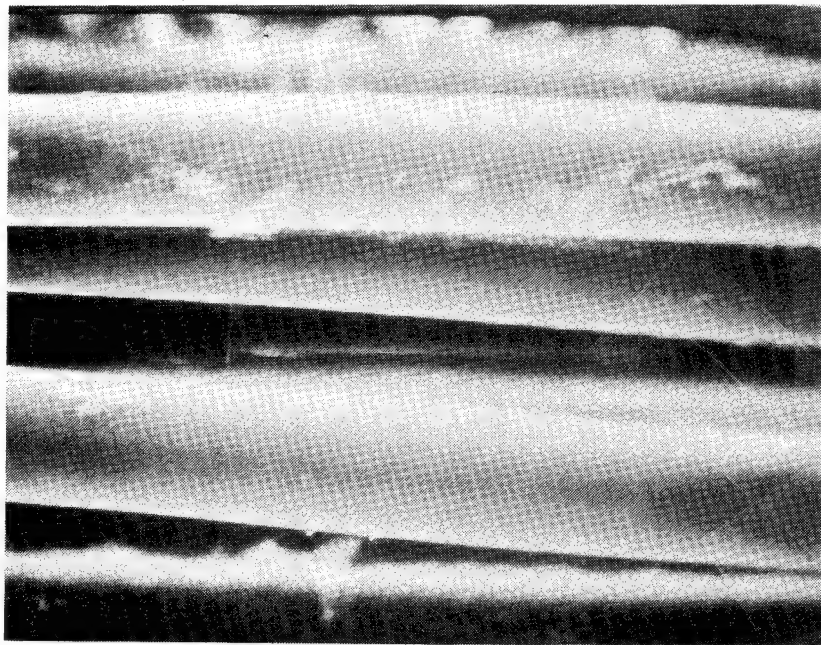


Figure 58. SEM micrograph of a Kevlar fiber located immediately outside the kink band (1500 X).

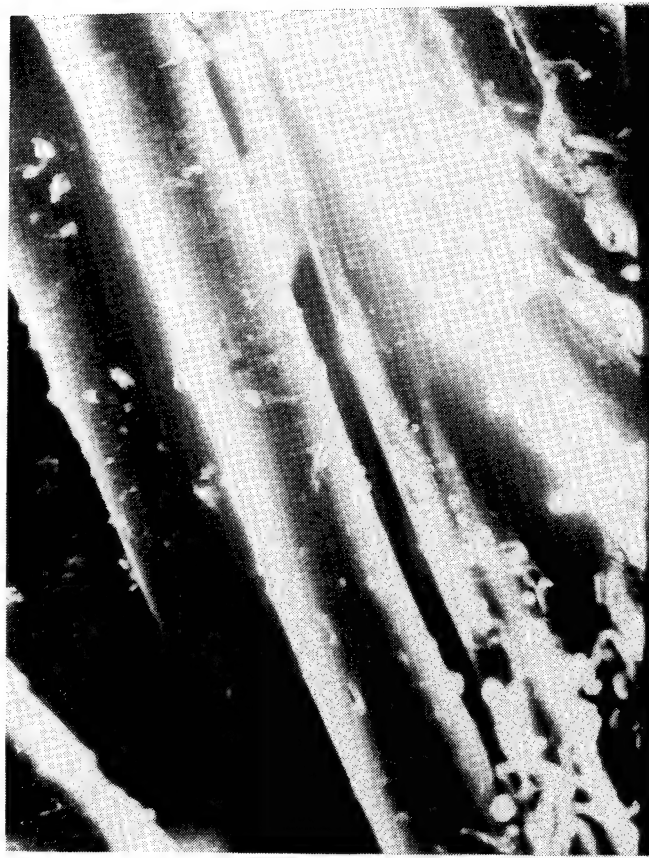


Figure 57. SEM micrograph of a Kevlar fiber within the kink band (1300 X).

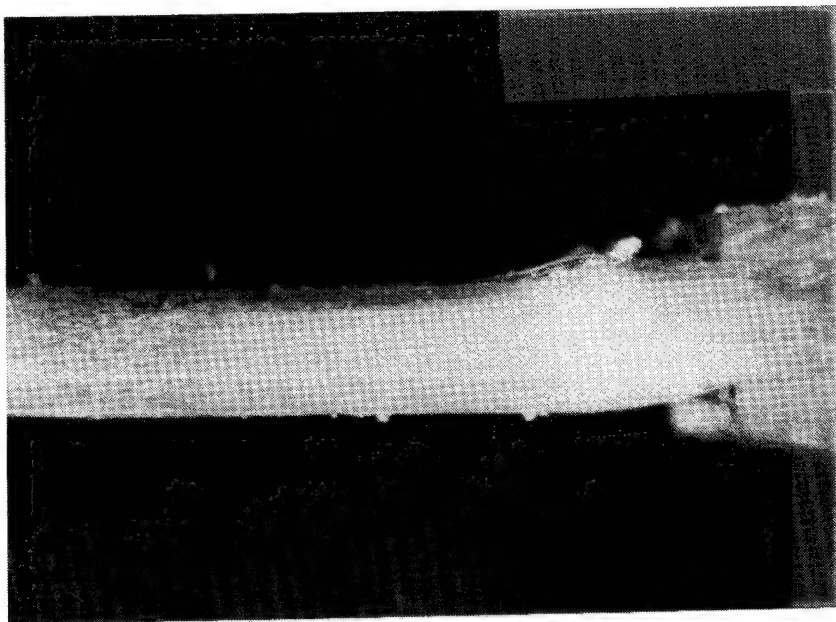
possible that the kinking in the composite occurs at the first sign of compressive failure in the fibers.

Figures 59 (a) and (b) show failures of glass/epoxy specimens tested at room and elevated temperatures, respectively. In the glass/epoxy specimen tested at room temperature, the kink band is very broad and the boundaries difficult to identify. There is no distinct kink band boundary; instead, the fibers were gradually bent in the vicinity of the failure band. There is no sign of damage to the fibers within the kink band. When tested at 100°C, however, there are some fiber fractures at the boundary, Figure 60. Furthermore, elevating the temperature and thereby softening the matrix results in a narrower kink band. Yet, there is no damage on the fibers within the kink band.

Other differences in kink morphology between different composites are in their kink band angles and kink lengths. On the average, graphite/epoxy composites have the smallest kink band angle (19°) and the smallest kink lengths (between 10-30 fiber diameters =0.07 to 0.2 mm). Kevlar/epoxy specimens tested at room temperature have the highest kink band angle (39°) and the second smallest kink length (0.45 mm). Kevlar/epoxy specimens tested at 100°C show almost the same kink band angle but a smaller average kink length (0.26 mm). Glass/epoxy specimens tested at 100°C show the second highest kink band angle (32°) and the highest kink length (1.2 mm). Since the kink band was not well defined in glass/epoxy specimens tested at room temperature, the kink band angle and the kink length could not be measured unambiguously.

The properties shown in Table 6 were used to calculate the strains at failure given by Equations 26 and 27. The applied stress at the time of

(b)



(a)

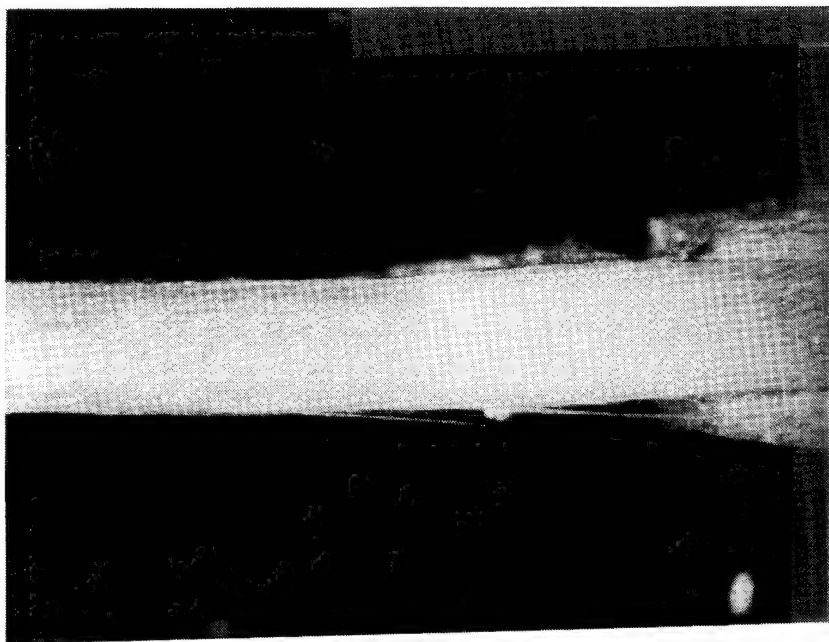


Figure 59. Compression failure in S2-glass/epoxy specimens: (a) tested at room temperature (8 \times) ; (b) tested at 100 $^{\circ}$ C (8 \times).



Figure 60. Fiber fractures at the kink band boundary of a S2-glass/epoxy specimen tested at 100 °C (150X).

Table 6. Prediction of Maximum Strains on the Fiber at the Time of Failure

Material	Avg. Compressive strength (MPa)	V_f	σ_f^* (MPa)	E_f (MPa)	τ_y (MPa)	$\varepsilon_b^{(+)}$ (%)	$\varepsilon_b^{(-)}$ (%)
Graphite/Epoxy	1300	0.60	2166	230000	68.0	-0.33	1.55
Glass/Epoxy (RT)	626	0.65	930	85000	70.4	0.49	2.67
Glass/Epoxy (100 °C)	669	0.65	1029	85000	38.9	-0.38	2.04
Kevlar/Epoxy (RT)	228	0.65	351	130000	27.1	0.53	1.07
Kevlar/Epoxy (RTP)	240	0.65	369	130000	23.2	0.39	0.95
Kevlar/Epoxy (ETP)	179	0.65	275	130000	23.9	0.59	1.01

failure σ_f^* was approximated from Equation 3 by

$$\sigma_f^* = \frac{x_c}{v_f}$$

As can be seen, the calculated strains on the tension side are either very small or negative. However, the strains on the compression side seem reasonable. It thus seems that fiber failure was initiated on the compression side at points of maximum fiber curvature. The compressive strains for the Kevlar fibers are higher than expected. Thus, these fibers appear to bend beyond the elastic limit when kink bands are formed.

Equations 30 and 31 were used with the properties listed in Table 6 to calculate the kink orientation angles and the kink lengths. Table 7 shows these calculated values along with the average experimental results for the kink band angle. The shear strains at failure were predicted by Equation 32. The calculated kink orientation angles are considerably smaller than those experimentally observed after failure. However, one should remember that the kink orientation angles in Table 7 were calculated at the onset of fiber failure. Once failure has occurred, the kink orientation angle can increase rapidly if the load is not immediately removed. The values reported in the literature were usually taken after final collapse of fibers. The predicted kink lengths for graphite and Kevlar composites agree fairly well with the experimental values discussed earlier. However, the prediction is too low for the S-glass fibers. The exact reason for such a discrepancy is not clear at present. One possible reason may be that the high failure strain of glass fibers allows growth of the kink band width even after failure.

As the predicted values of shear strain at failure show, the kink bands

Table 7. Predicted Values of Kink Orientation Angle, Kink Length, and Shear Strain at Failure

Material	α (degrees)	δ/d_f	β^* (degrees)	τ_y (%)
Graphite/ Epoxy	3.6	8.0	19.0	6.3
S2-Glass/ Epoxy	8.7	7.5	-	-
S2-Glass/ Epoxy (100 °C)	4.3	7.1	32.0	7.7
Kevlar/ Epoxy (RT)	8.8	24.5	39.0	16.3
Kevlar/ Epoxy (RTP)	7.2	23.9	38.0	13.2
Kevlar/ Epoxy (ETP)	9.9	27.7	35.0	18.3

* Experimental

undergo a significant amount of shear deformation. The local shear deformation at failure is the highest in Kevlar/epoxy followed by glass/epoxy and graphite/epoxy composites.

3.4 Short-Beam-Shear Testing of Preloaded Graphite/Epoxy Composites

When a unidirectional composite is subjected to an axial compressive force, transverse stresses are induced. These stresses result from the difference between Poisson's ratios of the fiber and matrix and also from additional bending of initially curved fibers. Whatever the source, these stresses may cause interfacial debonding especially when the quality of bonding is poor.

Greszczuck [20] showed that in model composites with steel reinforcements, the mode of failure and strength changed with the quality of bonding. In specimens with poor fiber-matrix adhesion failure was by premature buckling of the reinforcements. Those with strong interface failed by compression yielding of the reinforcements. Piggot [19] reported failure by longitudinal splitting in composites with hard matrix (microbuckling suppressed) and strong fibers. Application of hydrostatic pressure can suppress the longitudinal splitting and increase the strength by changing the mode of failure back to microbuckling [11, 15, 16].

In light of the foregoing discussion and the fiber-matrix debonding that was observed in some of the graphite/epoxy and graphite/thermoplastic composites (See Figures 45 through 54), one may raise the following question: Which one occurs first, fiber microbuckling or fiber-matrix debonding? In Chapter 2, an answer to this question was attempted by means of acoustic emission monitoring on embedded fiber bundles. It was concluded

that debonding does not occur gradually, but occurs suddenly at the time of bundle failure. Here, another attempt to answer the same question for unidirectional composites is discussed.

Since the presence of fiber-matrix debonding results in low interlaminar shear strength, the following experiment was conducted:

- a. the specimen was loaded to near its ultimate compressive strength (UCS),
- b. the load was removed,
- c. the specimen was then tested in short-beam-shear to measure the residual interlaminar shear strength,
- d. the residual shear strength was compared with the shear strength of virgin specimens.

Three unidirectional composites that had shown longitudinal splitting in a previous study [39] were chosen for this purpose: T300/5208, T300/4901/mPDA, and T700/4901/mPDA. IITRI specimens were prepared, loaded in compression and unloaded prior to final failure. The tabs were then removed and a short-beam-shear specimen was prepared out of the gage section. The specimen geometry and the testing procedure followed the ASTM standards D 2344-67. Although this method does not give an accurate measure of the interlaminar shear strength [42 and 43], it was judged to be adequate for our comparative analysis. One major drawback to this method of measuring interlaminar shear strength is that mixed-mode rather than pure shear failure modes may occur. A very likely mode of failure that is usually mixed with shear is microbuckling of fibers under the loading pin. However, this type of fiber microbuckling would also occur at a lower stress if fiber-matrix debonding is present.

The test matrix in Table 8 shows the specimen dimensions, the compressive loads applied, and the apparent horizontal shear strengths. The T300/5208 specimens were the first group to be tested. Their failure was by a mixed mode, Figure 61. Therefore, the span/depth ratio was slightly decreased for T700/4901/mPDA specimens. In T700/4901/mPDA specimens, however, the span/depth could not be reduced due to the smaller thickness of the panels and the limitation imposed by the testing fixture on the minimum span; the span was thus decreased to the smallest allowed by the testing fixture, Table 8. These were effective in changing the mode of failure to the one of predominantly shear, Figure 62.

In Reference [39] ten specimens of each composite were tested to measure their average ultimate compressive strengths (UCS). In the case of T300/5208 the average UCS was 1182 MPa with a variation from 887 to 1535 MPa. For T300/4901/mPDA the average UCS was 1394 MPa and the strength ranged from 1313 to 1546 MPa. And finally, for T700/4901/mPDA the average UCS was 1185 MPa and the strengths varied from 930 to 1370 MPa. It is thus seen that the highest percent of UCS shown in Table 8 for each composite is considerably higher than the lower bound of its compressive strength.

The results indicate that application of a compressive load does not affect the apparent horizontal shear strength or the failure modes involved in any of the composites tested. Even in T300/5208 and T700/4901/mPDA specimens which were loaded to over 90% UCS, no reduction of shear strength is observed. Therefore, it is concluded that if fiber-matrix debonding occurs, it would not happen gradually, but rather catastrophically, and near the final failure. Thus, debonding cannot be detected unless the composite is loaded very near its UCS. This conclusion

Table 8. Short-Beam-Shear Test Results.

Material: T300/5208
 Span/Depth = 3.85
 Length/Depth = 5.86
 Span = 13 mm ; depth = 3.30 mm

Specimen	Preloaded to	Apparent horizontal shear strength (MPa)
V1	0% UCS	116.5
V2	0% UCS	105.7
V3	0% UCS	95.5
SH1	89.6% UCS	112.7
SH2	91.7% UCS	114.0

Material: T300/mPDA
 Span/Depth = 3.90
 Length/Depth = 5.70
 Span = 11 mm ; depth = 2.87 mm

Specimen	Preloaded to	Apparent horizontal shear strength (MPa)
1	0% UCS	102.6
2	0% UCS	106.0
3	0% UCS	104.5
W108-31	80.0% UCS	103.1
W108-32	81.0% UCS	106.3

Material: T700/mPDA
 Span/Depth = 3.65
 Length/Depth = 5.00
 Span = 13 mm ; depth = 3.56 mm

Specimen	Preloaded to	Apparent horizontal shear strength (MPa)
1	0% UCS	114.6
2	0% UCS	118.1
3	0% UCS	117.4
W110-29	80.4% UCS	115.0
W110-31	85.2% UCS	115.3
W110-32	88.4% UCS	117.3
W110-33	94.6% UCS	113.0

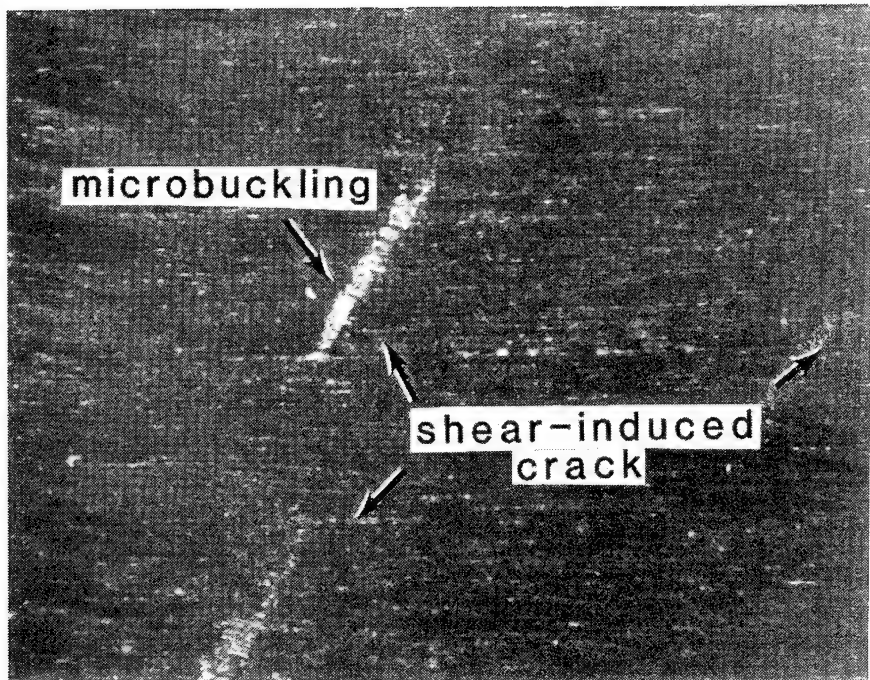
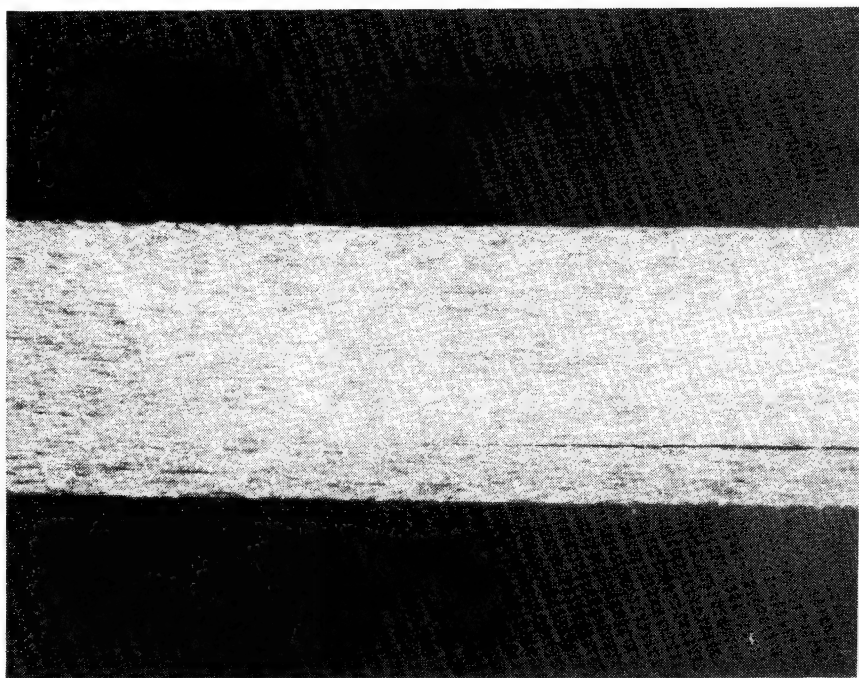
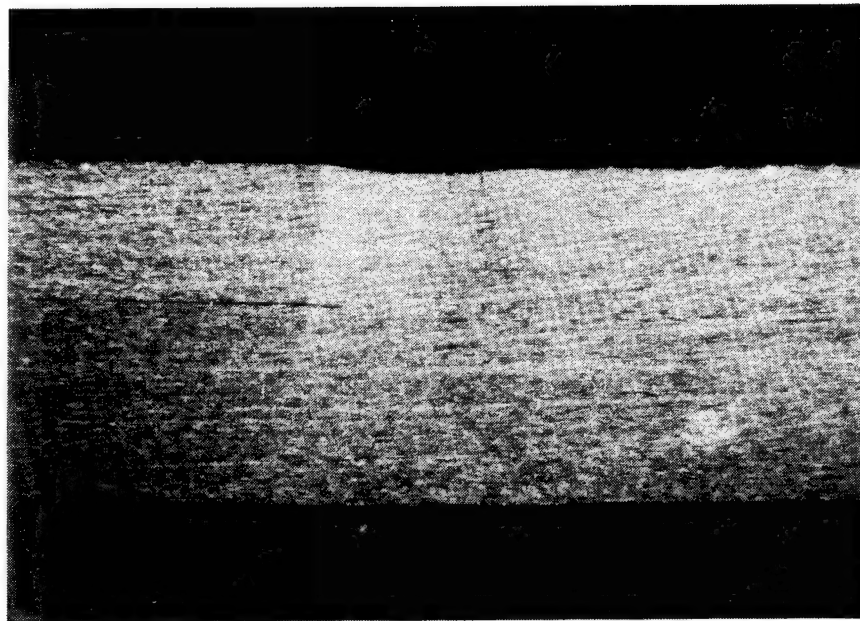


Figure 6]. Failure by a mixed mode of shear and microbuckling in a T300/5208 short-beam-shear specimen (50X).



(a)



(b)

Figure 62. Shear dominated failure: (a) in a virgin T300/mPDA specimen (12X);
(b) in a virgin T700/mPDA specimen (12X).

agrees with the result of the acoustic emission study described in Section 2.

3.5 Summary

Kinking was the mode of failure in all the unidirectional composites studied. Fiber microbuckling caused the kinking failure in graphite/epoxy, graphite/thermoplastic resin, and glass/epoxy composites. In Kevlar/epoxy, however, fiber failure triggered the kinking. This means that whatever the incipient mode of failure, slip occurs on a plane oblique to the loading because of the presence of a resolved shear stress on this plane. The angle of slip (i.e. the kink band angle) is usually smaller than 45°.

In composites with graphite fibers, the kink band is narrow and well defined. The kink band boundary is defined by fracture of fibers, and multiple fracture of fibers is common within the band. The fibers on the fracture surfaces are tilted in a direction compatible with the overall slip. The T300 fibers seem to bond to the epoxy resins better than the T700 fibers. Also, the fiber-matrix bonding in the T300/PEEK composite looks better than that in the T300/PPS composite.

In glass/epoxy specimens tested at room temperature, the kink band is broad and no definite kink band boundaries can be identified due to the very gradual change of curvature in fibers leading into the failure zone. Softening of the matrix at an elevated temperature results in a well-defined kink band. That is, fibers are sharply bent at the boundaries, and some are fractured.

In Kevlar/epoxy composites, the failure of fibers at the kink band boundaries is by kinking of microfibrils. There is no sign of damage on the fibers within or without the kink band.

Preloading some representative graphite/epoxy specimens to near their

respective compressive strengths did not affect their residual short-beam-shear strengths. Therefore, fiber-matrix debonding does not occur gradually but suddenly and concurrently with the final failure. This conclusion is in agreement with the observed acoustic emission behavior of embedded bundles.

Kink band geometry was characterized through an analytical model that was developed under the assumption of plastic yielding in the matrix within the kink band.

4. CONCLUSIONS

1. Kevlar and P75 graphite fibers are inherently weak in compression. Their compressive failure is the result of kinking of microfibrils. E-glass, T300 graphite, T700 graphite, and FP alumina fibers fail by microbuckling when embedded in a resin.
2. Buckling of fibers was uniformly distributed in a very soft resin, but quite localized in stiff resins.
3. Debonding and fiber fracture occurred immediately after microbuckling of fibers in fiber bundle specimens.
4. Failure strains and segment lengths observed for bundle specimens follow the trends predicted for a single fiber embedded in infinite matrix.
5. With the exception of P75 graphite and Kevlar, compressive failure strains of the fibers studied are higher than those of their composites. Thus, the ultimate compressive strengths of fibers are not fully utilized in composites and failure is governed by other factors, primarily the properties of the matrix.
6. Acoustic emissions can be used to detect compressive failure of Kevlar fibers.
7. Acoustic emission study of embedded glass bundles indicate that no detectable debonding occurs until immediately before fiber buckling.
8. In unidirectional composites, kinking failure can be caused by either microbuckling or intrinsic compressive failure of fibers. Kinking failure is caused by fiber microbuckling in graphite and glass composites while it is by microfibrillar kinking of fibers in Kevlar/epoxy composites.
9. In graphite composites, kink bands are narrow with a kink band angle between 10 to 30°. Multiple fiber fracture within the kink band produces

kink lengths between 2 to 4 times the fiber diameter.

10. In glass/epoxy composites tested at room temperature, the failure bands were broad and there was no fiber fracture. Elevating the testing temperature, however, resulted in a narrower kink band with some fiber fractures.

11. In Kevlar/epoxy composites the only sign of fiber damage was at the kink-band boundaries. This may be due to the relaxation or even slight stretching of the fibers within the kink band after failure. Another possible reason is that failure occurs as soon as some fibers fail.

12. The T300 graphite fiber shows better bonding than the T700 graphite fiber in graphite/epoxy composites. The PEEK resins show better bonding than the PPS resin when combined with T300 fibers.

13. Residual shear strengths of precompressed specimens indicate no gradual interfacial failure occurring in compression.

14. Assuming plastic yielding of matrix within the kink band, a theoretical model was developed to predict the kink geometry. According to this model, the kink orientation angle at the onset of fiber failure is only a fraction of the kink orientation angle observed after the final failure. Most of the rotation of the fibers occurs after their collapse. Failure of the fibers initiates on the compression side at the kink band boundary. The predicted values of kink band lengths were reasonable for graphite and Kevlar composites, but too small for S-glass composites.

REFERENCES

1. J. G. Williams and M. D. Rhodes, "Effect of Resins on Impact Damage Tolerance of Graphite/Epoxy Laminates," Composite Materials: Testing and Design (ASTM STP 787), 1982, pp. 450-480.
2. J. G. Williams, "Effect of Impact Damage and Open Holes on the Compression Strength of Tough Resin/High Strain Fiber Laminates," NASA TM-85756, February 1984.
3. B. W. Rosen, "Mechanics of Composite Strengthening," Fiber Composite Materials, ASM, 1964, pp. 58-75.
4. H. Schuerch, "Prediction of Compressive Strength in Uniaxial Boron Fiber-Metal Matrix Composite Materials," AIAA Journal, Vol. 4, 1966, pp. 102-106.
5. W. Y. Chung and R. B. Testa, "The Elastic Stability of Fibers in a Composite Plate," Journal of Composite Materials, Vol. 3, 1969, pp. 58-79.
6. L. B. Greszczuk, "Microbuckling of Unidirectional Composites," AFML-TR-71-231, January 1972.
7. L. B. Greszczuk, "Failure Mechanisms of Composites Subjected to Compressive Loading," AFML-TR-72-107, August 1972.
8. J. G. Davis, "Compression Strength of Fiber Reinforced Composite Materials," Composite Reliability, ASTM STP 580, 1975, pp. 364-377.
9. A. S. D. Wang, "A Non-Linear Microbuckling Model Predicting the Compressive Strength of Unidirectional Composites," ASTM paper 78-WA/Aero-1, 1978.
10. H. T. Hahn and J. G. Williams, "Compression Failure Mechanisms in Unidirectional Composites," NASA TM 85834, 1984.
11. C. W. Weaver and J. G. Williams, "Deformation of a Carbon/Epoxy Composite Under Hydrostatic Pressure," Journal of Materials Science, Vol. 10, 1975, pp. 1323-1333.
12. C. R. Chaplin, "Compressive Fracture in Unidirectional Glass-Reinforced Plastics," Journal of Composite Materials, Vol. 12, 1977, pp. 347-352.
13. S. V. Kulkarni, J. S. Rice, and B. W. Rosen, "An Investigation of the Compressive Strength of Kevlar 49/Epoxy Composites," Composites, Vol. 6, 1975, pp. 217-225.
14. A.G. Evans and N.F. Adler, "Kinking as a Mode of Structural Degradation in Carbon Fiber Composites," Acta Metallurgica, Vol. 26, 1978, pp. 725-738.

15. T. V. Parry and G. S. Wronski, "Kinking and Compressive Failure in Uniaxially Aligned Carbon Fiber Composites Tested Under Superposed Hydrostatic Pressure," Journal of Materials Science, Vol. 17, 1982, pp. 893-900.
16. A. S. Wronski and T. V. Parry, "Compressive Failure and Kinking in Uniaxially Aligned Glass/Resin Composites Under Superposed Hydrostatic Pressure," Journal of Materials Science, Vol. 17, 1982, pp. 3656-3662.
17. N.L. Hancox, "The Compression Strength of Unidirectional Carbon Fiber Reinforced Plastics, Journal of Materials Science, Vol. 10, 1975, pp. 234-242.
18. M. R. Piggot and P. Wilde, "Compressive Strength of Aligned Steel Reinforced Epoxy Resin," Journal of Materials Science, Vol. 15, 1980, pp. 2811-2815.
19. M. R. Piggot, "A Theoretical Framework for the Compressive Properties of Aligned Fiber Composites," Journal of Materials Science, Vol. 16, 1981, pp. 2837-2845.
20. L. B. Greszczuk, "On Failure Modes of Unidirectional Composites Under Compressive Loading," MDAC Paper G8721, Presented at the 2nd USA-USSR Symposium on Fracture of Composite Materials, Bethlehem, Pa., 9-12 March 1981.
21. M.M.Sohi, H.T.Hahn, and J.G. Williams, "The Effect of Matrix Toughness and Modulus on Compressive Failure Modes of Quasi-Isotropic Graphite/Epoxy Composites," Presented at ASTM Symposium on Toughened Composites, Houston, 13-15 March 1985, NASA TM-87604.
22. H. M. Hawthorn and E. Teghtsoonian, "Axial Compression Fracture in Carbon Fibers," Journal of Material Science, Vol. 10, 1975, pp. 41-51.
23. S. J. Deteresa, S. R. Allen, R. J. Farris, and R. S. Porter, "Compressive and Torsional Behavior of Kevalr 49 Fibers," Journal of Materials Science, Vol. 19, 1984, pp. 57-72.
24. L. Lorenzo and H. T. Hahn, "Acoustic Emission Study of Fracture of Fibers Embedded in Epoxy Matrix," Proc. The First Int. Symp. on Acoustic Emission from Reinforced Composites, SPI, 1983, Session 2.
25. M. G. Dobb, O. J. Johnson, and B. P. Saville, Polymer, Vol. 22, pp. 960-965.
26. M. A. Sadowsky, S. L. Pu, and M. A. Hussain, "Buckling of Microfibers," Journal of Applied Mechanics, Vol. 34, 1967, 1011-1016.
27. L. R. Herrman, N. E. Mason, and T. K. Chan, "Response of Reinforcing Wires to Compressive States of Stress," Journal of Composite Materials, 1, 1967, 212-226.

28. Y. Lanir and Y.C.B. Fung, "Fiber Composite Columns under Compression," Journal of Composite Materials, Vol. 6, 1972, pp. 387-401.
29. R. Rothwell and M. Arrington, Nature Physical Science, Vol. 233, October 25, 1971, pp. 163-169.
30. E.M. DeFerran and B. Harris, "Compression Strength of Polyester resin Reinforced with Steel Wires," Journal of Composite Materials, Vol. 4, January 1970, pp. 62-72.
31. E. Orowan, "A Type of Plastic Deformation New in Metals," Nature, Vol. 149, 1942, pp. 643-646.
32. T. Seto and Y. Tajima, "Observation of Kink Bands in Oriented Polyethyline," Japanese Journal of Applied Physics, Vol. 5, 1966, pp. 534-546.
33. D. A. Zaukelies, "Observation of Slip in Nylon 66 and 610 and Its Interpretation in Terms of a New Model," Journal of Applied Physics, Vol. 33, 1962, pp. 2797-2803.
34. F.A. Donath, "Some Information Squeezed Out of Rock," American Scientist, Vol. 58, 1970, pp. 54-73.
35. L. Carlsson, C. Fellers and A. DeRuvo, "The Mechanism of Failure in Bending of Paperboard," Journal of Materials Science, Vol 15, 1980, pp. 2636-2642.
36. J.B. Wilson, R.P. McEvoy, Jr. and R.W. Perkins, "On Compression Failure in Wood Materials: A Mathematical and Experimental Simulation," Proc. the First International Conference on Wood Fracture, Forintek Canada Corp., 1979, pp. 290-301.
37. C. A. Berg and M. Salama, "Fatigue of Graphite Fiber-Reinforced Epoxy in Compression," Fiber Science Technology, Vol. 6, 1973, p. 79-118.
38. B. Budiansky, "Micromechanics," Computers and Structures, Vol. 16, 1983, pp. 3-120.
39. M. Sohi, "Compressive Behavior of Graphite/Epoxy Composites," Master's Thesis, Washington University, Dec. 1984.
40. H.T. Hahn, D.G. Hwang, W.K. Chin, and S.Y. Lo., "Mechanical Properties of a Glass-Wound S2-Glass/Epoxy Composite for Flywheel Applications," Lawrence Livermore Laboratory Report, 1982, UCRL-15365.
41. H. T. Hahn and W. K. Chin, "Mechanical Properties of a Filament-Wound Aramid Fiber/Epoxy Composite for Flywheel Applications," Lawrence Livermore Laboratory Report, 1982, UCRL-15461.

42. S. A. Sattar, and D. H. Kellogg, "The Effect of Geometry on The Mode of Failure of Composites in Short-Beam Shear Test," Composite Materials: Testing and Design (ASTM STP 460), 1969, pp. 62-71.
43. C. A. Berg, J. Tirosh, and M. Israeli, "Analysis of Short Beam Bending of Fiber Reinforced Composites," Composite Materials: Testing and Design (ASTM STP 497), 1972, pp. 206-218.

1. Report No. NASA CR-3988	2. Government Accession No.	3. Recipient's Catalog No.	
4. Title and Subtitle Compression Failure Mechanisms of Composite Structures		5. Report Date June 1986	
7. Author(s) H. Thomas Hahn, Mohsen Sohi & Suresh Moon		6. Performing Organization Code	
9. Performing Organization Name and Address Center for Composites Research Washington University St. Louis, MO 63130		8. Performing Organization Report No. WU/CCR-85/5	
12. Sponsoring Agency Name and Address National Aeronautics and Space Administration Washington, DC 20546		10. Work Unit No.	
15. Supplementary Notes Langley Technical Monitor: Jerry G. Williams Final Report		11. Contract or Grant No. NAG1-295	
16. Abstract An experimental and analytical study was conducted to delineate the compression failure mechanisms of composite structures. Results on unidirectional and quasi-isotropic graphite/epoxy laminates were published previously. The present report summarizes further results on kink band formation in unidirectional composites. In order to assess the compressive strengths and failure modes of fibers themselves, a fiber bundle was embedded in epoxy casting and tested in compression. A total of six different fibers were used together with two resins of different stiffnesses. The failure of highly anisotropic fibers such as Kevlar 49 and P-75 graphite was due to kinking of fibrils. However, the remaining fibers--T300 and T700 graphite, E-glass, and alumina--failed by localized microbuckling. Compressive strengths of the latter group of fibers were not fully utilized in their respective composites. In addition, acoustic emission monitoring revealed that fiber-matrix debonding did not occur gradually but suddenly at final failure.		13. Type of Report and Period Covered Final 8/1/82-7/31/85	
17. Key Words (Suggested by Author(s)) Unidirectional composites Compressive behavior Graphite/epoxy Kink band Acoustic emission		18. Distribution Statement Unclassified - Unlimited	
Microbuckling		Subject Category 24	
19. Security Classif. (of this report) Unclassified	20. Security Classif. (of this page) Unclassified	21. No. of Pages 118	22. Price A06

For sale by the National Technical Information Service Springfield, Virginia 22161

NASA-Langley, 1986